

# RtEstim: Effective reproduction number estimation with trend filtering

Jiapeng Liu<sup>1\*</sup>, Zhenglun Cai<sup>2</sup>, Paul Gustafson<sup>1</sup>, Daniel J. McDonald<sup>1</sup>

**1** Department of Statistics, The University of British Columbia, Vancouver, British Columbia, Canada

**2** Centre for Health Evaluation and Outcome Sciences, The University of British Columbia, Vancouver, British Columbia, Canada

\* [jiapeng.liu@stat.ubc.ca](mailto:jiapeng.liu@stat.ubc.ca)

## Abstract

To understand the transmissibility and spread of infectious diseases, epidemiologists turn to estimates of the effective reproduction number. While many estimation approaches exist, their utility may be limited. Challenges of surveillance data collection, model assumptions that are unverifiable with data alone, and computationally inefficient frameworks are critical limitations for many existing approaches. We propose a discrete spline-based approach **RtEstim** that solves a convex optimization problem—Poisson trend filtering—using the proximal Newton method. It produces a locally adaptive estimator for effective reproduction number estimation with heterogeneous smoothness. **RtEstim** remains accurate even under some process misspecifications and is computationally efficient, even for large-scale data. The implementation is easily accessible in a lightweight R package [rtestim](#).

## Author summary

Effective reproduction number estimation presents many challenges due to data collection, modelling assumptions, and computational burden. Such limitations hinder the accurate estimation of the effective reproduction number. Our motivation is to

develop a model that produces accurate estimates, is robust to model misspecification, and is straightforward to use and computationally efficient, even for large counts and long time periods. We propose a convex optimization model with an  $\ell_1$  trend filtering penalty. It couples accurate estimation of the effective reproduction number with desired smoothness. We solve the optimization using the proximal Newton method, which converges rapidly and is numerically stable. Our software, conveniently available in the R package `RtEstim`, can produce estimates in seconds for incidence sequences with hundreds of observations. These estimates are produced for a sequence of tuning parameters and can be selected using a built-in cross validation procedure.

## 1 Introduction

The effective reproduction number (or, effective reproductive number) at time  $t$  is defined to be the expected number of secondary infections produced by a primary infection throughout the course of the entire infection if conditions remain the same at the specific time. The instantaneous reproduction number is a type of effective reproduction number focusing on how past infection contribute to the transmission at a specific timepoint; while, the case reproduction number, which is another type of effective reproduction number, focuses on the transmission of the same cohort of individuals with the same date of infection or symptom onset [1]. Effective reproduction number is a key quantity for understanding infectious disease dynamics including the potential size of an outbreak and the required stringency of control measures [2, 3]. Tracking the time series of this quantity is useful for understanding whether or not future infections are likely to increase or decrease from the current state [4]. Let  $\mathcal{R}(t)$  denote the effective reproduction number at time  $t$ . Practically, as long as  $\mathcal{R}(t) < 1$ , infections will decline gradually, eventually resulting in a disease-free equilibrium, whereas when  $\mathcal{R}(t) > 1$ , infections will continue to increase, resulting in endemic equilibrium. While  $\mathcal{R}(t)$  is fundamentally a continuous time quantity, it can be related to data only at discrete points in time  $t = 1, \dots, n$ . This sequence of effective reproduction numbers over time is not observable, but, nonetheless, is easily interpretable and retrospectively describes the course of an epidemic. Therefore, a number of procedures exist to estimate  $\mathcal{R}_t$  from different types of observed incidence

data such as cases, deaths, or hospitalizations, while relying on various domain-specific  
assumptions, e.g., [5–8]. Importantly, accurate estimation of effective reproduction  
numbers relies heavily on the quality of the available data, and, due to the limitations of  
data collection, such as underreporting and lack of standardization, estimation  
methodologies rely on various assumptions to compensate. Because model assumptions  
may not be easily verifiable from data alone, it is also critical for any estimation  
procedure to be robust to model misspecification.

Many existing approaches for effective reproduction number estimation are Bayesian:  
they estimate the posterior distribution of  $\mathcal{R}_t$  conditional on the observations. One of  
the first such approaches is the software **EpiEstim** [9], described in [10]. This method is  
prospective, in that it uses only observations available up to time  $t$  in order to estimate  
 $\mathcal{R}_t$  for each  $i = 1, \dots, t$ . An advantage of **EpiEstim** is its straightforward statistical  
model: new incidence data follows the Poisson distribution conditional on past incidence  
combined with the conjugate gamma prior distribution for  $\mathcal{R}_t$  with fixed  
hyperparameters. Additionally, the serial interval distribution, the distribution of the  
period between onsets of primary and secondary infections in a population, is fixed and  
known. For this reason, **EpiEstim** requires little domain expertise for use, and it is  
computationally fast. Thompson et al. modified this method to distinguish imported  
cases from local transmission and simultaneously estimate the serial interval  
distribution [11]. Nash et al. further extended **EpiEstim** by using “reconstructed” daily  
incidence data to handle irregularly spaced observations [12]. Recently, Abbott et al.  
proposed a Bayesian latent variable framework, **EpiNow2** [13], which leverages incident  
cases, deaths or other available streams simultaneously along with allowing additional  
delay distributions (incubation period and onset to reporting delays) in modelling [14].  
Lison et al. proposed an extension that handles missing data by imputation followed by  
a truncation adjustment [15]. These modifications are intended to increase accuracy at  
the most recent (but most uncertain) timepoints, to aid policymakers. Parag et al. also  
proposed a Bayesian approach, **EpiFilter**, based on the (discretized) Kalman filter and  
smoother [16]. **EpiFilter** also estimates the posterior of  $\mathcal{R}_t$  given a Gamma prior and  
Poisson distributed incident cases. Compared to **EpiEstim**, however, **EpiFilter**  
estimates  $\mathcal{R}_t$  retrospectively using all available incidence data both before and after time  
 $t$ , with the goal of being more robust in low-incidence periods. Gressani et al. proposed

a Bayesian P-splines approach, **EpiLPS**, that assumes negative binomial distributed observations [17]. Trevisin et al. also proposed a Bayesian model estimated with particle filtering to incorporate spatial structures [18]. Bayesian approaches estimate the posterior distribution of the effective reproduction numbers and possess the advantage that credible intervals may be easily computed. They incorporate the prior knowledge on parameters to modelling, while some techniques are also used to eliminate the power of prior parameters on the posterior estimates to make the estimates more plausible, e.g., Thompson et al. assumes a relatively large prior mean of  $\mathcal{R}_t$  (appreciably larger than 1), and if the estimate is less than 1, researchers will know it is a direct result from data, instead of the choice of prior parameters [11]. Some Bayesian approaches, however, are computationally expensive, since they require more intensive computational routines, especially when observed data sequences are long or hierarchical structures are complex, e.g., [14]. While, some Bayesian methods with more efficient structures, especially the ones with only conjugate priors, can be computationally efficient, e.g., [10]. Below, we compare the accuracy of our method to the aforementioned Bayesian models, **EpiEstim**, **EpiLPS**, **EpiFilter**, and **EpiNow2**, which provides accessible softwares or scripts.

There are also frequentist approaches for  $\mathcal{R}_t$  estimation. Abry et al. proposed regularizing the smoothness of  $\mathcal{R}_t$  through penalized regression with second-order temporal regularization, additional spatial penalties, and with Poisson loss [19]. Pascal et al. extended this procedure by introducing another penalty on outliers [20].

Pircalabelu et al. proposed a spline-based model relying on the assumption of exponential-family distributed incidence [21]. Ho et al. estimates  $\mathcal{R}_t$  while monitoring the time-varying level of overdispersion [22]. There are other spline-based approaches such as [23, 24], autoregressive models with random effects [25] that are robust to low incidence, and generalized autoregressive moving average (GARMA) models [26] that are robust to measurement errors in incidence data.

We propose an effective (instantaneous, specifically) reproduction number estimator, called **RtEstim** that requires only incidence data. Our model makes the conditional Poisson assumption, similar to much of the prior work described above, but is empirically more robust to misspecification. This estimator is defined by a convex optimization problem with Poisson loss and  $\ell_1$  penalty on the temporal evolution of  $\log(\mathcal{R}_t)$  to impose smoothness over time. As a result, **RtEstim** generates discrete splines,

and the estimated curves (in logarithmic space) appear to be piecewise polynomials of  
an order selected by the user. Importantly, the estimates are locally adaptive, meaning  
that different time ranges may possess heterogeneous smoothness. Because we penalize  
the logarithm of  $\mathcal{R}_t$ , we naturally accommodate the positivity requirement, in contrast  
to related methods [19, 20], can handle large or small incidence measurements, and are  
automatically (reasonably) robust to outliers without additional constraints.

A small illustration using three years of Covid-19 case data in Canada is shown in  
[Fig 1](#) [27], where we consider a time-varying serial interval distribution. Specifically, we  
get the viral evolution and spread data from the `duotang` project provided by [28] and  
compute the probabilities of having each variant at each timepoint using the  
multinomial logistic regression. The variant with the highest probability is deemed as  
the *dominant* variant at a specific timepoint. There are four dominant variants  
throughout the epidemic, Ancestral lineage, Alpha, Delta, and Omicron over time with  
mean 5.1, 3.5, 3.5, 3.0 and standard deviation 4.0, 4.5, 2.9, 2.1 respectively, estimated by  
Xu et al. [29].

While our approach is straightforward and requires little domain knowledge for  
implementation, we also implement a number of refinements. We use a proximal  
Newton method to solve the convex optimization problem along with warm starts to  
produce estimates efficiently, typically in a matter of seconds, even for long sequences of  
data. In a number of simulation experiments, we show empirically that our approach is  
more *accurate* than existing methods at estimating the true effective reproduction  
numbers and *robust* under multiple settings of the misspecification of incidence  
distribution, serial interval distribution, and the order of graphical curvature.

The manuscript proceeds as follows. We first introduce the methodology of `RtEstim`  
including the renewal equation and the development of Poisson trend filtering estimator.  
We explain how this method could be interpreted from the Bayesian perspective,  
connecting it to previous work in this context. We provide illustrative experiments  
comparing our estimator to other Bayesian alternatives. We then apply our `RtEstim` on  
the Covid-19 pandemic in Canada and the 1918 influenza pandemic in the United States.  
Finally, we conclude with a discussion of the advantages and limitations of our approach  
and describe practical considerations for effective reproduction number estimation.

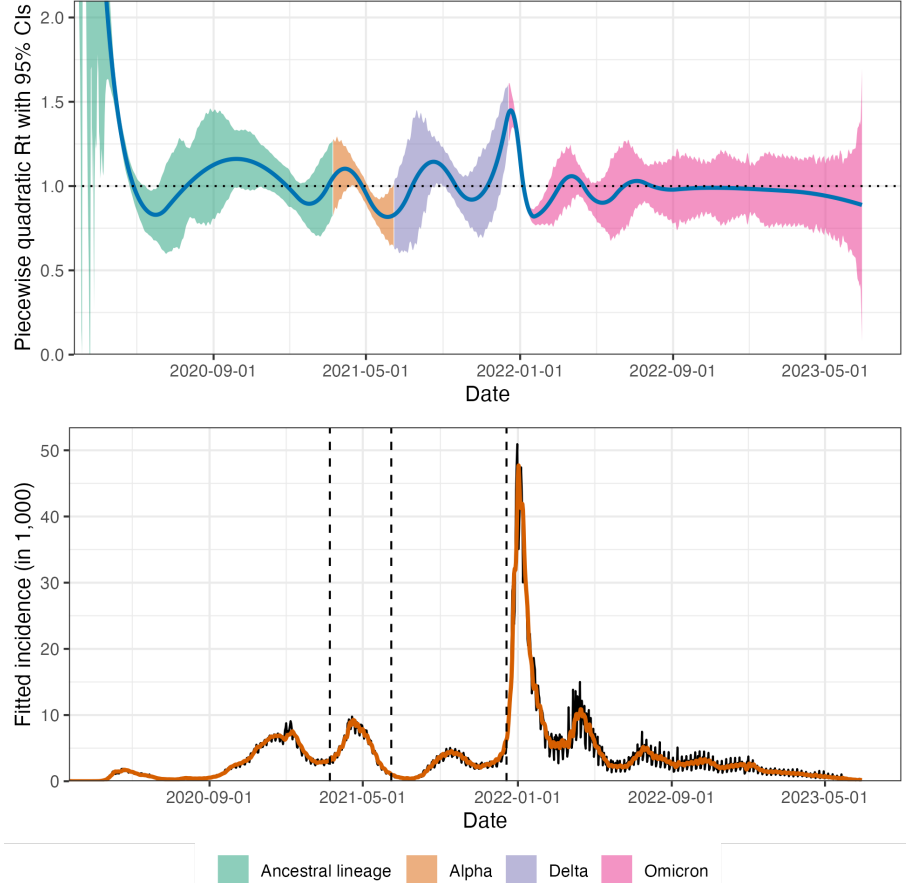


**Fig 1.** A demonstration of effective reproduction number estimation by RtEstim and the corresponding predicted incident cases for the Covid-19 epidemic in Canada during the period from January 23, 2020 to June 28, 2023. In the top panel, the blue curve is the estimated piecewise quadratic  $\mathcal{R}_t$  and the colorful ribbon is the corresponding 95% confidence band. The ribbon is dyed by four colors representing the variants whose serial interval distributions are used to estimate  $\mathcal{R}_t$ . The y-axis is truncated for a better illustration; the estimated  $\mathcal{R}_t$  decreases from 10.77 to below 2 in the first 55 timepoints. In the bottom panel, the black curve is the observed Covid-19 daily confirmed cases, and the orange curve on top of it is the predicted incident cases corresponding to the estimated  $\mathcal{R}_t$ . The three vertical dashed lines represent the beginning of a new dominant variant.

## 2 Methods

### 2.1 Renewal model for incidence data

The effective reproduction number  $\mathcal{R}(t)$  is defined to be the expected number of secondary infections at time  $t$  produced by a primary infection sometime in the past. To make this precise, denote the number of new infections at time  $t$  as  $y(t)$ . Then the total primary infectiousness can be written as  $\eta(t) := \int_0^\infty p(t, i)y(t - i)di$ , where  $p(t, i)$  is the

probability that a new secondary infection at time  $t$  is the result of a primary infection  
123  
 that occurred  $i$  time units in the past. The effective reproduction number is then given  
124  
 as the value that equates  
125

$$\mathbb{E}[y(t) | y(j), j < t] = \mathcal{R}(t)\eta(t) = \mathcal{R}(t) \int_0^\infty p(t,i)y(t-i)di, \quad (1)$$

otherwise known as the renewal equation. The period between primary and secondary  
126  
 infections is exactly the generation time of the disease, but given real data, observed at  
127  
 discrete times (say, daily), this delay distribution must be discretized into contiguous  
128  
 time intervals, say,  $(0, 1], (1, 2], \dots$ . It results in the sequence  $\{p_i^t\}_{i=0}^\infty$  corresponding to  
129  
 observations  $y_t$  for each  $t$  and yields the discretized version of Eq (1),  
130

$$\mathbb{E}[y_t | y_1, \dots, y_{t-1}] = \mathcal{R}_t \eta_t = \mathcal{R}_t \sum_{i=1}^{\infty} p_i^t y_{t-i}. \quad (2)$$

Many approaches to estimating  $\mathcal{R}_t$  rely on Eq (2) as motivation for their procedures,  
131  
 among them, **EpiEstim** [10] and **EpiFilter** [16].  
132

In most cases, it is safe to assume that infectiousness disappears beyond  $\tau$   
133  
 timepoints ( $p(t, i) = 0$  for  $i > \tau$ ), resulting in the truncated integral of the generation  
134  
 interval distribution  $\int_0^\tau p(t,i)di = 1$  for each  $t$ . Generation time, however, is usually  
135  
 unobservable and tricky to estimate, so common practice is to approximate it by the  
136  
 serial interval: the period between the symptom onsets of primary and secondary  
137  
 infections. If the infectiousness profile after symptom onset is independent of the  
138  
 incubation period (the period from the time of infection to the time of symptom onset),  
139  
 then this approximation is justifiable: the serial interval distribution and the generation  
140  
 interval distribution share the same mean. However, other properties may not be  
141  
 similarly shared, and, in general, the generation interval distribution is a convolution of  
142  
 the serial interval distribution with the distribution of the difference between  
143  
 independent draws from the delay distribution from infection to symptom onset. See,  
144  
 for example, [1] for a fuller discussion of the dangers of this approximation. Nonetheless,  
145  
 treating these as interchangeable is common [10, 30] and doing otherwise is beyond the  
146  
 scope of this work. Additionally, we take the generation interval (and, therefore, the  
147  
 serial interval) either as constant over time  $t$ , i.e., the probability  $p(i)$  depends only on  
148

the gap between primary and secondary infections and not on the time  $t$  when the  
secondary infection occurs, or as time-varying, i.e., the probability  $p(t, i)$  also depends  
on the time of (the symptom onset of) the secondary infection. For our methods, we  
assume that the serial interval can be accurately estimated from auxiliary data (say by  
contact tracing, or previous epidemics) and we take it as fixed, as is common in existing  
studies, e.g., [10, 19, 20].

The renewal equation in Eq (2) relates observable data streams (incident cases)  
occurring at different timepoints to the effective reproduction number given the serial  
interval. The fact that it depends only on the observed incident counts makes it  
reasonable to estimate  $\mathcal{R}_t$ . However, data collection idiosyncrasies can obscure this  
relationship. Diagnostic testing targets symptomatic individuals, omitting  
asymptomatic primary infections which can lead to future secondary infections. Testing  
practices, availability, and uptake can vary across space and time [31, 32]. Finally,  
incident cases as reported to public health are subject to delays due to laboratory  
confirmation, test turnaround times, and eventual submission to public health [33]. For  
these reasons, reported cases are lagging indicators of the course of the pandemic.  
Furthermore, they do not represent the actual number of new infections that occur on a  
given day, as indicated by exposure to the pathogen. The assumptions described above  
(homogeneous mixing, similar susceptibility and social behaviours, etc.) are therefore  
consequential. That said, Eq (2) also provides some comfort about deviations from these  
assumptions. We discuss three types of deviation here. First, if  $y_t$  is scaled by a constant  
(in time) describing the reporting ratio, then it will cancel from both sides when we take  
the ratio of secondary and primary infection when calculating the effective reproduction  
number. Second, even if such a scaling varies in time, as long as it varies slowly relative  
to the set of  $p_i$  that are larger than 0, Eq (2) will be a reasonably accurate  
approximation, so that  $\mathcal{R}_t$  can still be estimated well from reported incidence data.  
Finally, even a sudden change in reporting ratio occurs at time  $t_1$ , it would only result  
in large errors in  $\mathcal{R}_t$  in the neighbourhood of  $t_1$  (where the size of this neighbourhood is  
determined indirectly by the effective support of  $\{p_i^t\}$ ). This robustness to certain types  
of data reporting issues partially justifies using Eq (2) to calculate  $\mathcal{R}_t$ .

## 2.2 Poisson trend filtering estimator

179

We use the daily confirmed incident cases  $y_t$  on day  $t$  to estimate the observed infectious cases under the model that  $y_t$ , given previous incident cases  $y_{t-1}, \dots, y_1$  and a constant serial interval distribution, follows a Poisson distribution with mean  $\Lambda_t$ . That is,

$$y_t \mid y_1, \dots, y_{t-1} \sim \text{Poisson}(\Lambda_t), \text{ where } \Lambda_t = \mathcal{R}_t \sum_{i=1}^{t-1} p_i y_{t-i} = \mathcal{R}_t \eta_t. \quad (3)$$

Given a history of  $n$  confirmed incident counts  $\mathbf{y} = (y_1, \dots, y_n)^\top$ , our goal is to estimate  $\mathcal{R}_t$  for each  $t = 1, \dots, n$ . A natural approach is to maximize the likelihood, producing the maximum likelihood estimator (MLE):

$$\begin{aligned} \hat{\mathcal{R}} &= \underset{\mathcal{R} \in \mathbb{R}_+^n}{\operatorname{argmax}} \mathbb{P}(\mathcal{R} \mid \mathbf{y}, \mathbf{p}) = \underset{\mathcal{R} \in \mathbb{R}_+^n}{\operatorname{argmax}} \prod_{t=1, \dots, n} \frac{(\mathcal{R}_t \eta_t)^{y_t} \exp\{-\mathcal{R}_t \eta_t\}}{y_t!} \\ &= \underset{\mathcal{R} \in \mathbb{R}_+^n}{\operatorname{argmin}} \sum_{t=1}^n \mathcal{R}_t \eta_t - y_t \log(\mathcal{R}_t \eta_t). \end{aligned} \quad (4)$$

This optimization problem, however, is easily seen to yield a one-to-one correspondence between the observation and the estimated effective reproduction number, i.e.,  $\hat{\mathcal{R}}_t = y_t / \eta_t$ , so that the estimated sequence  $\hat{\mathcal{R}}$  will have no significant smoothness.

The MLE is an unbiased estimator of the true parameter  $\mathcal{R}_t$ , but unfortunately has high variance: changes in  $y_t$  result in proportional changes in  $\hat{\mathcal{R}}_t$ . To avoid this behaviour, and to match the intuition that  $\mathcal{R}_t \approx \mathcal{R}_{t-1}$ , we advocate enforcing smoothness of the effective reproduction numbers. This constraint will decrease the estimation variance, and hopefully lead to more accurate estimation of  $\mathcal{R}$ , as long as the smoothness assumption is reasonable. Smoothness assumptions are common (see e.g., [1, 16]), but the type of smoothness assumption is critical. Cori et al. imposes smoothness indirectly by estimating  $\mathcal{R}_t$  with moving windows of past observations [10]. The Kalman filter procedure of [16] would enforce in  $\ell_2$ -smoothness  $(\int_0^n (\hat{\mathcal{R}}''(t))^2 dt < C$  for some constant  $C$ ), although the computational implementation results in  $\hat{\mathcal{R}}$  taking values over a discrete grid. Pascal et al. produces piecewise linear  $\hat{\mathcal{R}}_t$ , which turns out to be closely related to a special case of our methodology [20]. Smoother estimated curves will provide high-level information about the entire epidemic, obscuring small local changes in  $\mathcal{R}(t)$ , but may also remove the ability to detect large sudden changes,

such as those resulting from lockdowns or other major containment policies. 203

To enforce smoothness of  $\hat{\mathcal{R}}_t$ , we add a trend filtering penalty to Eq (5) [34–37]. 204

Because  $\mathcal{R}_t > 0$ , we explicitly penalize the divided differences (discrete derivatives) of 205  
neighbouring values of  $\log(\mathcal{R}_t)$ . Let  $\theta := \log(\mathcal{R}) \in \mathbb{R}^n$ , so that  $\Lambda_t = \eta_t \exp(\theta_t)$ , and 206  
 $\log(\eta_t \mathcal{R}_t) = \log(\eta_t) + \theta_t$ . For evenly spaced incident case, we write our estimator as the 207  
solution to the optimization problem 208

$$\hat{\mathcal{R}} = \exp(\hat{\theta}) \quad \text{where} \quad \hat{\theta} = \underset{\theta \in \mathbb{R}^n}{\operatorname{argmin}} \eta^\top \exp(\theta) - \mathbf{y}^\top \theta + \lambda \|D^{(k+1)}\theta\|_1, \quad (5)$$

where  $\exp(\cdot)$  applies elementwise and  $\|\mathbf{a}\|_1 := \sum_{i=1}^n |a_i|$  is the  $\ell_1$  norm. Here, 209  
 $D^{(k+1)} \in \mathbb{Z}^{(n-k-1) \times n}$  is the  $(k+1)^{\text{th}}$  order divided difference matrix for any 210  
 $k \in \{0, \dots, n-1\}$ .  $D^{(1)} \in \{-1, 0, 1\}^{(n-1) \times n}$  is the divided difference matrix for  $k=0$ . 211  
It is a sparse matrix with diagonal band of the form: 212

$$D^{(1)} = \begin{pmatrix} -1 & 1 & & & \\ & -1 & 1 & & \\ & & \ddots & \ddots & \\ & & & -1 & 1 \end{pmatrix}. \quad (6)$$

$D^{(k+1)}$  for  $k \geq 1$  is defined recursively as  $D^{(k+1)} := D^{(1)} D^{(k)}$ , where 213  
 $D^{(1)} \in \{-1, 0, 1\}^{(n-k-1) \times (n-k)}$  takes the form defined in Eq (6). More description on 214  
the recursive definition of divided difference matrix for trend filtering can be found 215  
in [35, 36]. 216

The tuning parameter (hyperparameter)  $\lambda$  balances data fidelity with desired 217  
smoothness. When  $\lambda = 0$ , the problem in Eq (5) reduces to the MLE in Eq (4). Larger 218  
tuning parameters privilege the regularization term and yield smoother estimates. 219  
Finally, there exists  $\lambda_{\max}$  such that any  $\lambda \geq \lambda_{\max}$  will result in  $D^{(k+1)}\hat{\theta} = 0$  and  $\hat{\theta}$  will 220  
be the Kullback-Leibler projection of  $\mathbf{y}$  onto the null space of  $D^{(k+1)}$  (see 221  
subsection 2.3). 222

The solution to Eq (5) will result in piecewise polynomials, specifically called discrete 223  
splines. For example, 0<sup>th</sup>-degree discrete splines are piecewise constant, 1<sup>st</sup>-degree 224  
curves are piecewise linear, and 2<sup>nd</sup>-degree curves are piecewise quadratic. For  $k \geq 1$ , 225  
 $k^{\text{th}}$ -degree discrete splines are continuous and have continuous discrete differences up to 226

degree  $k - 1$  at the knots (i.e., changing points between segments). This penalty results  
227  
in more flexibility compared to the homogeneous smoothness that is created by the  
228  
squared  $\ell_2$  norm. Using different orders of the divided differences results in estimated  
229  
effective reproduction numbers with different smoothness properties.  
230

For unevenly spaced data, the spacing between neighbouring parameters varies with  
231  
the time between observations, and thus, the divided differences must be adjusted by  
232  
the times that the observations occur. Given observation times  $\mathbf{x} = (x_1, \dots, x_n)^\top$ , for  
233  
 $k \geq 1$ , define a  $k^{\text{th}}$ -order diagonal matrix  
234

$$X^{(k)} = \text{diag} \left( \frac{k}{x_{k+1} - x_1}, \frac{k}{x_{k+2} - x_2}, \dots, \frac{k}{x_n - x_{n-k}} \right). \quad (7)$$

Letting  $D^{(\mathbf{x}, 1)} := D^{(1)}$ , then for  $k \geq 1$ , the  $(k + 1)^{\text{th}}$ -order divided difference matrix for  
235  
unevenly spaced data can be created recursively by  $D^{(\mathbf{x}, k+1)} := D^{(1)} X^{(k)} D^{(\mathbf{x}, k)}$ . No  
236  
adjustment is required for  $k = 0$ .  
237

Due to the penalty structure, this estimator is locally adaptive, meaning that it can  
238  
potentially capture local changes such as the initiation of control measures. Abry et al.  
239  
and Pascal et al. considered only the 2<sup>nd</sup>-order divided difference of  $\mathcal{R}_t$  rather than its  
240  
logarithm [19, 20]. In comparison to their work, our estimator (i) allows for arbitrary  
241  
degrees of temporal smoothness and (ii) avoids the potential numerical issues of  
242  
penalizing/estimating positive real values. Furthermore, as we will describe below, our  
243  
procedure is computationally efficient for estimation over an entire sequence of penalty  
244  
strengths  $\lambda$  and provides methods for choosing how smooth the final estimate should be.  
245

### 2.3 Solving over a sequence of tuning parameters

246

We can solve the Poisson trend filtering estimator over an arbitrary sequence of  $\lambda$  that  
247  
produces different levels of smoothness in the estimated curves. We consider a  
248  
candidate set of  $M$   $\lambda$ -values,  $\boldsymbol{\lambda} = \{\lambda_m\}_{m=1}^M$ , that is strictly decreasing.  
249

Let  $D := D^{(k+1)}$  for simplicity in the remainder of this section. As  $\lambda \rightarrow \infty$ , the  
250  
penalty term  $\lambda \|D\theta\|_1$  dominates the Poisson objective, so that minimizing the objective  
251  
is asymptotically equivalent to minimizing the penalty term, which results in  $\|D\theta\|_1 = 0$ .  
252  
In this case, the divided differences of  $\theta$  with order  $k + 1$  is always 0, and thus,  $\theta$  must  
253  
lie in the null space of  $D$ , that is,  $\theta \in \mathcal{N}(D)$ . The same happens for any  $\lambda$  beyond this  
254

threshold, so define  $\lambda_{\max}$  to be the smallest  $\lambda$  that produces  $\theta \in \mathcal{N}(D)$ . It turns out  
255  
 that this value can be written explicitly as  $\lambda_{\max} = \|(D^\dagger)^\top(\eta - y)\|_\infty$ , where  $D^\dagger$  is the  
256  
 (left) generalized inverse of  $D$  satisfying  $D^\dagger D = I$  and  $\|a\|_\infty := \max_{i=1}^n \{|a_i|\}$  is the  
257  
 infinity norm. Therefore, we use  $\lambda_1 = \lambda_{\max}$  and then choose the minimum  $\lambda_M$  to be  
258  
 $r\lambda_{\max}$  for some  $r \in (0, 1)$  (typically  $r = 10^{-5}$ ). Given any  $M \geq 3$ , we generate a  
259  
 sequence of  $\lambda$  values to be equally spaced on the log-scale between  $\lambda_1$  and  $\lambda_M$ .  
260

To compute the sequence efficiently, the model is estimated sequentially by visiting  
261  
 each component of  $\boldsymbol{\lambda}$  in order. The estimates produced for a larger  $\lambda$  are used as the  
262  
 initial values (warm starts) for the next smaller  $\lambda$ . By solving through the entire  
263  
 sequence of tuning parameters, we have a better chance to achieve a better trade-off  
264  
 between bias and variance, and accordingly, improved accuracy relative to procedures  
265  
 examining one fixed value of  $\lambda$ .  
266

## 2.4 Choosing a final $\lambda$

267

We estimate model accuracy over the candidate set through  $K$ -fold cross validation  
268  
 (CV) to choose the best tuning parameter. Specifically, we divide  $\mathbf{y}$  (except the first and  
269  
 last observations) roughly evenly and randomly into  $K$  folds, estimate  $\mathcal{R}_t$  for all  $\boldsymbol{\lambda}$   
270  
 leaving one fold out, and then predict the held-out observations. Model accuracy can be  
271  
 measured by multiple metrics such as mean squared error  $\text{MSE}(\hat{y}, y) = n^{-1}\|\hat{y} - y\|_2^2$  or  
272  
 mean absolute error  $\text{MAE}(\hat{y}, y) = n^{-1}\|\hat{y} - y\|_1$ , but we prefer to use the (average)  
273  
 deviance, to mimic the likelihood in Eq (4):  
274

$D(y, \hat{y}) = n^{-1} \sum_{i=1}^n 2(y_i \log(y_i) - y_i \log(\hat{y}_i) - y_i + \hat{y}_i)$ , with the convention that  
275  
 $0 \log(0) = 0$ . Note that for any  $K$  and any  $M$ , we will end up estimating the model  
276  
 $(K + 1)M$  times rather than once.  
277

## 2.5 Approximate confidence bands

278

We also provide empirical confidence bands of the estimators with approximate  
279  
 coverage. Consider the related estimator  $\tilde{\mathcal{R}}_t$  defined as  
280

$$\tilde{\mathcal{R}} = \exp(\tilde{\theta}) \quad \text{where} \quad \tilde{\theta} = \underset{\theta \in \mathbb{R}^n}{\operatorname{argmin}} \eta^\top \exp(\theta) - \mathbf{y}^\top \theta + \lambda \|D\theta\|_2^2. \quad (8)$$

Let  $\tilde{\mathbf{y}} = \eta \circ \tilde{\mathcal{R}}$ , and then it can be shown (for example, Theorem 2 in [38]) that an estimator for  $\text{Var}(\tilde{\mathbf{y}})$  is given by  $(\text{diag}(\tilde{\mathbf{y}}^{-2}) + \lambda D^\top D)^\dagger$ . Finally, an application of the delta method shows that  $\text{Var}(\tilde{\mathbf{y}}_t)/\eta_t^2$  is an estimator for  $\text{Var}(\tilde{\mathcal{R}}_t)$  for each  $t = 1, \dots, n$ . We therefore use  $(\text{diag}(\hat{\mathbf{y}}^{-2}) + \lambda D^\top D)_t^\dagger/\eta_t^2$  as an estimator for  $\text{Var}(\hat{\mathcal{R}}_t)$ . An approximate  $(1 - \alpha)\%$  confidence interval then can be written as  $\hat{\mathcal{R}}_t \pm s_t \times T_{\alpha/2, n-\text{df}}$ , where  $s_t$  is the square-root of  $\text{Var}(\hat{\mathcal{R}}_t)$  for each  $t = 1, \dots, n$  and df is the number of changepoints in  $\hat{\theta}$  plus  $k + 1$  [35]. An approximate confidence interval of  $\hat{\mathbf{y}}$  can be computed similarly.

## 2.6 Bayesian perspective

Unlike many other methods for  $\mathcal{R}_t$  estimation, our approach is frequentist rather than Bayesian. Nonetheless, it has a corresponding Bayesian interpretation: as a state-space model with Poisson observational noise, autoregressive transition equation of degree  $k \geq 0$ , e.g.,  $\theta_{t+1} = 2\theta_t - \theta_{t-1} + \varepsilon_{t+1}$  for  $k = 1$ , and Laplace transition noise  $\varepsilon_{t+1} \sim \text{Laplace}(0, 1/\lambda)$ . Compared to **EpiFilter** [16], we share the same observational assumptions, but our approach has a different transition noise. **EpiFilter** estimates the posterior distribution of  $\mathcal{R}_t$ , and thus it can provide credible interval estimates as well. Our approach produces the maximum *a posteriori* estimate via an efficient convex optimization, obviating the need for MCMC sampling. But the associated confidence bands are created differently.

## 3 Results

Implementation of our approach is provided in the R package **rtestim**. All computational experiments are conducted on the Cedar cluster provided by Compute Canada with R 4.3.1. The R packages used for simulation and real-data application are **EpiEstim** 2.2-4 [39], **EpiLPS** 1.2.0 [40], and **rtestim** 0.0.4. The R scripts for **EpiFilter** are used [41].

### 3.1 Synthetic experiments

306

#### 3.1.1 Problem design

307

We simulate four scenarios of the time-varying effective reproduction number, intended to mimic different epidemics. The first two scenarios are rapidly controlled by intervention, where the  $\mathcal{R}(t)$  consists of one discontinuity and two segments. Scenario 1 has constant  $\mathcal{R}(t)$  before and after an intervention, while Scenario 2 grows exponentially, then decays. The other two scenarios are more complicated, where more waves are involved. Scenario 3 has four linear segments with three discontinuities, which reflect the effect of an intervention, resurgence to rapid transmission, and finally suppression of the epidemic. Scenario 4 involves sinusoidal waves throughout the epidemic. The first three scenarios and the last scenario are motivated by [16] and [17] respectively. We name the four scenarios as (1) *piecewise constant*, (2) *piecewise exponential*, (3) *piecewise linear*, and (4) *periodic* lines or curves respectively.

318

In all cases, the times of observation are regular, and epidemics are of length  $n = 300$ . Specifically, in Scenario 1,  $\mathcal{R}_t = 2, 0.8$  before and after  $t = 120$ . In Scenario 2,  $\mathcal{R}_t$  increases and decreases exponentially with rates 0.01, 0.005 pre and post  $t = 100$ . In Scenario 3,  $\mathcal{R}_t$  is piecewise linear with four discontinuous segments following

$$\begin{aligned} \mathcal{R}(t) = & \left( 2.5 - \frac{0.5}{74} (t - 1) \right) \mathbf{1}_{[1,76)}(t) + \left( 0.8 - \frac{0.2}{74} (t - 76) \right) \mathbf{1}_{[76,151)}(t) \\ & + \left( 1.7 + \frac{0.3}{74} (t - 151) \right) \mathbf{1}_{[151,226)}(t) + \left( 0.9 - \frac{0.4}{74} (t - 226) \right) \mathbf{1}_{[226,300]}(t), \end{aligned} \quad (9)$$

where  $\mathbf{1}_A(t) = 1$ , if  $t \in A$ , and  $\mathbf{1}_A(t) = 0$  otherwise. In Scenario 4,  $\mathcal{R}_t$  is realization of the continuous, periodic curve generated by the function

$$\mathcal{R}(t) = 0.2 \left( (\sin(\pi t/12) + 1) + (2 \sin(5\pi t/12) + 2) + (3 \sin(5\pi t/6) + 3) \right), \quad (10)$$

evaluated at equally spaced points  $t \in [0, 10]$ . These  $\mathcal{R}_t$  scenarios are illustrated in Fig 2. We compute the expected incidence  $\Lambda_t$  using the renewal equation, and generate the incident infections from the Poisson distribution  $y_t \sim \text{Pois}(\Lambda_t)$ . To verify the performance of our model under the violation of the distributional assumption, we also generate incident cases using the negative binomial distribution with dispersion size

$\rho = 5$ , i.e.,  $y_t \sim \text{NB}(\mu_t = \Lambda_t, \rho = 5)$ . The probability mass function can be written as 330

$$p(y_t|\Lambda_t, \rho) = \frac{\Gamma(y_t + \rho)}{\Gamma(\rho)y_t!} \left(\frac{\rho}{\rho + \Lambda_t}\right)^\rho \left(\frac{\Lambda_t}{\rho + \Lambda_t}\right)^{y_t}, \quad (11)$$

where  $y_t = 0, 1, 2, \dots, t = 1, \dots, n$  and the variance is  $\sigma_t^2 = \Lambda_t + \frac{\Lambda_t^2}{\rho}$ , which follows the 331  
definition in [17]. The variance equals the mean appended by another term of the 332  
squared mean over a relatively small dispersion size, so the squared mean can dominate 333  
the term and result in sufficient overdispersion level in the generated samples. We 334  
visualize the dispersion level (using the ratio of standard deviation over mean) of 335  
synthetic epidemics in Figure A.2.1 in the supplementary document to have a better 336  
idea on the overdispersion level of the negative binomial distributions (with size 5) 337  
compared the Poisson distributions with the same mean. 338

We use serial interval (SI) distributions of measles (with mean 14.9 and standard 339  
deviation 3.9) at Hagelloch, Germany in 1861 [42] and SARS (with mean 8.4 and 340  
standard deviation 3.8) at Hong Kong in 2003 [43], inspired by [10], to generate 341  
synthetic epidemics. We initialize all epidemics with  $y_1 = 2$  cases and generate for 342  
 $t = 2, \dots, 300$ . The synthetic measles epidemics have smaller incident cases in general, 343  
and the SARS epidemics have larger incidence. The intuition behind this is a smaller 344  
mean of serial interval with a similar standard deviation leads to an averaged shorter 345  
period of the onsets of symptoms between the primary and secondary infected 346  
individuals, which results in a greater growth of incidence within the same period of 347  
time. We also consider shorter flu epidemics with 50 timepoints with piecewise linear 348  
 $\mathcal{R}_t$  (Scenario 3) considering both incidence distributional assumptions. The motivation 349  
is to compare our method and other alternatives with EpiNow2 which takes much 350  
longer time to converge for long epidemics (almost 2 hours to converge for a measles 351  
epidemic with 300 timepoints) than other methods. Besides using the correct SI 352  
distributions to estimate  $\mathcal{R}_t$ , we also consider the scenarios where SI is mildly or 353  
majorly misspecified. More details on experimental settings and results for shorter 354  
epidemics and misspecification of SI distributions are given in Sections A.2.1 and A.3 in 355  
the supplementary document respectively. 356

For each problem setting (including a SI distribution, an  $\mathcal{R}_t$  scenario, and an 357  
incidence distribution), we generate 50 random samples, resulting in 800 total synthetic 358

epidemics. An example of measles and SARS epidemics for each effective reproduction number scenario with an incidence distribution is displayed in Fig 2.

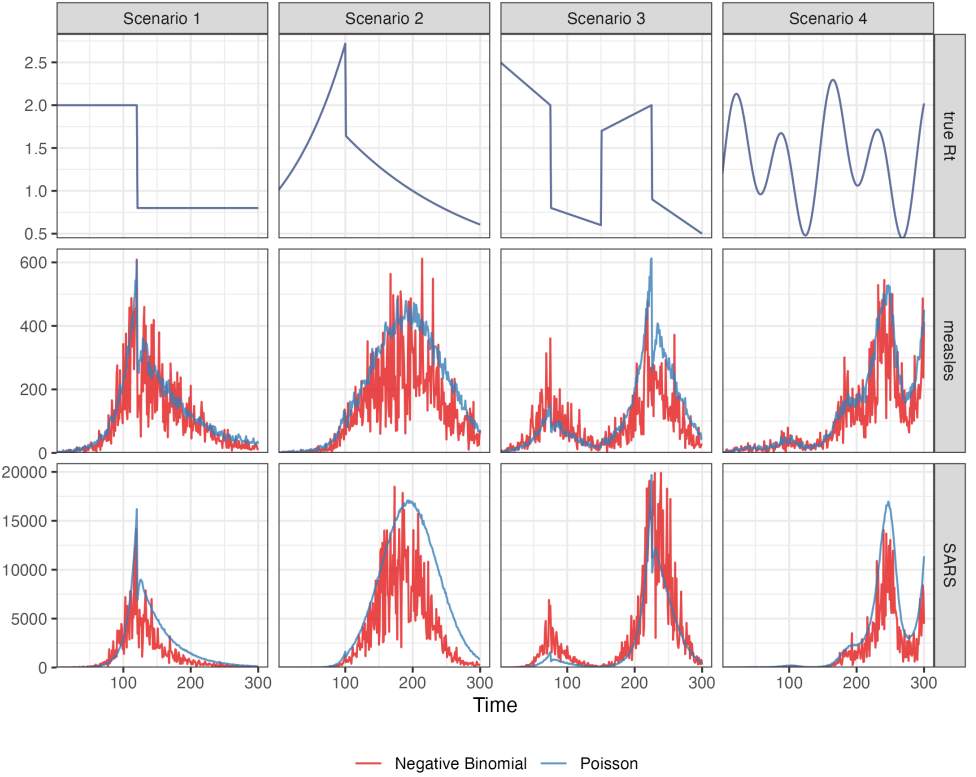


**Fig 2.** The effective reproduction numbers for four  $\mathcal{R}_t$  scenarios (in the top row). The synthetic measles (in the middle row) and SARS (in the bottom row) incident cases drawn from Poisson (in blue curves) or negative binomial (in red curves) distribution across 4  $\mathcal{R}_t$  scenarios (in four columns respectively).

### 3.1.2 Algorithm design

We compare **RtEstim** to **EpiEstim**, **EpiLPS**, and **EpiFilter**. **EpiEstim** estimates the posterior distribution of the effective reproduction number given a Gamma prior and Poisson distributed observations over a trailing window, under the assumption that the effective reproduction number is constant during that window. A larger window averages out more fluctuations, leading to smoother estimates, whereas, a shorter sliding window is more responsive to sudden spikes or declines. We tried the weekly sliding window, as well as a monthly window. However, since neither considerably outperforms the other across all scenarios, we defer the monthly results to the supplementary document. **EpiLPS** is another Bayesian approach that estimates

P-splines based on the Laplace approximation to the conditional posterior with negative  
371 binomial likelihood. **EpiFilter** is also a Bayesian approach that smooths  $\mathcal{R}_t$  at each  
372 timepoint given all observed incidence, improved upon the filtering methods that filter  
373  $\mathcal{R}_t$  given the observations prior to and on time  $t$ .  
374

We apply **RtEstim** with four degrees, piecewise constant  $k = 0$ , piecewise linear  
375  $k = 1$ , piecewise quadratic  $k = 2$ , and piecewise cubic  $k = 3$  polynomials, to solve all  
376 problem settings. We run 10-fold cross validation (CV) to choose the best tuning  
377 parameter from the candidate set of size 50, i.e.,  $\lambda = \{\lambda_1, \dots, \lambda_{50}\}$ , for long epidemics,  
378 and 5-fold CV for short epidemics (deferred to Sections A.3.2 and A.4.2 in the  
379 supplementary document). Specifically, we divide all samples (except the first and last  
380 entries) into 10 folds evenly and randomly, and build models on each subset of samples  
381 by leaving a fold out using each choice of the tuning parameter. We select the tuning  
382 parameter that gives the lowest averaged deviance between the estimated incidence and  
383 the observed samples averaged over all folds.  
384

We specify the parameters of the alternative methods, using the ones which were  
385 applied to their own experimental settings and so are deemed as the “best” tuned ones,  
386 in our experiments. Due to the limitations of the software implementations that some  
387 necessary hyperparameters are not allowed to choose, we can only specify the supported  
388 ones. This limitation does not only restrict the choices on tuning parameters which  
389 impacts the model fitting, but also those for optimization (as mentioned above). For  
390 example, in **EpiLPS**, one must specify the number of basis functions as well as 5 prior  
391 parameters. **EpiFilter** needs a grid of possible  $\mathcal{R}_t$  values, along with a fixed value for  
392 the diffusion noise, and a prior value for  $\mathcal{R}_t$ . **EpiNow2** has many prior parameters  
393 (depending on the particular model used) and does not compute a Bayes Factor or other  
394 model selection criterion. Had we attempted to tune some or all of these parameters, we  
395 would need to implement cross validation from scratch for each, as none of these provide  
396 ways to choose them. Here are the hyperparameters used in modelling for each  
397 alternative method. We consider both weekly and monthly sliding windows in  
398 **EpiEstim**, 40 basis functions in **EpiLPS** with the NelderMead method to maximize the  
399 hyperparameter posterior distribution. We input 2000 grid size in **EpiFilter** with 0.1  
400 diffusion noise and uniform prior on  $\mathcal{R}_t$  with mean 1/2000, and use the smoothed  $\mathcal{R}_t$   
401 given all observed incidence as the final estimates.  
402

For the  $\mathcal{R}_t$  estimation using all models for each problem, we use the same serial  
interval distribution, that was used to generate synthetic data. Taking different  
hyperparameters into consideration, we solve each problem using 8 methods including  
`EpiEstim` with weekly or monthly sliding windows, `EpiLPS`, `EpiFilter`, and `RtEstim`  
with piecewise constant, linear, quadratic, or cubic curves. Throughout the four  $\mathcal{R}_t$   
scenarios, the degrees of `RtEstim` can be correctly or wrongly specified. Our method  
can take the advantage of a correctly specified degree of piecewise polynomials  
compared to other methods, while the competitors only consider one fixed degree of  
smoothness which may not coincide with the “true” (assumed) degree of  $\mathcal{R}_t$ . Meanwhile,  
by using different degrees to solve the same problem, we will illustrate that a wrongly  
specified degree can still result in accurate  $\mathcal{R}_t$  estimation in our experiments.

`RtEstim` estimates can appear to be piecewise polynomials with a selected degree  $k$ .  
When faced with real data, the choice of  $k$  should be done either (1) based on the  
analyst’s preference for the result (e.g., “I want to find large jumps, so  $k = 0$ ”) or (2) in  
a data-driven manner, as a component of the estimation process. Our software enables  
both cases, and the second case can be implemented by simply fitting for different  $k$  and  
choosing the set  $k, \lambda$  that has smallest CV score. Thus, all necessary choices can be  
accomplished based solely on the data. Our software is a departure from existing  
methods in that we *allow* this choice and provide simple data-driven methods to  
accomplish it. `EpiEstim` has no such facility (although, implicitly, one must somehow  
choose the size of the rolling window). `EpiFilter` effectively uses cubic splines (similar  
to  $k = 3$ , but simply continuous rather than piecewise continuous). Similarly, `EpiLPS`  
specifically chooses the cubic B-spline basis, which is similar to degree  $k = 3$ . `EpiNow2`  
allows various choices through Gaussian Process kernels, and while one can put priors  
on the parameters of the kernel, the choice of kernel is required. In our experience,  
using  $k > 3$  is nearly indistinguishable from  $k = 3$ , though it is allowed. So if the  
analyst somehow imagines “ $\mathcal{R}_t$  is best described by a 10<sup>th</sup> order piecewise polynomial”  
then the software can easily accommodate this desire.

### 3.1.3 Accuracy measurement

To measure estimation accuracy, we compare the estimated  $\hat{\mathcal{R}}$  to “true”  $\mathcal{R}$  using the  
Kullback-Leibler (KL) divergence. The KL divergence for the Poisson distribution

(summed over across all  $t$ ) which measures the accuracy of the  $\mathcal{R}_t$  estimates is defined as 434

$$D_{KL}(\mathcal{R} \parallel \widehat{\mathcal{R}}) = \sum_{t=1}^N \eta_t \left( \mathcal{R}_t \log \left( \frac{\mathcal{R}_t}{\widehat{\mathcal{R}}_t} \right) + \widehat{\mathcal{R}}_t - \mathcal{R}_t \right), \quad (12)$$

where  $\mathcal{R} = \{\mathcal{R}_t\}_{t=1}^N$  and  $\eta_t$  is the total infectiousness. We use the scaled (mean) KL 435  
divergence:  $\overline{D_{KL}}(\mathcal{R} \parallel \widehat{\mathcal{R}}) := D_{KL}(\mathcal{R} \parallel \widehat{\mathcal{R}})/N$ , where  $N$  is the length of the estimated  $\widehat{\mathcal{R}}$  436  
sequence. To fairly compare across methods, we drop the estimates during the first 437  
week because estimates from **EpiEstim** are not available until  $t = 8$  (using a weekly 438  
sliding window). The details on the derivation of the KL divergence in Eq (12) is 439  
provided in Section A.1 in the supplementary document. 440

KL divergence is more appropriate for measuring accuracy because it connects 441  
directly to the Poisson likelihood used to generate the data, whereas standard measures 442  
like the mean-squared error correspond to Gaussian likelihood. Using Poisson likelihood 443  
has the effect of increasing the relative cost of mistakes when  $\Lambda_t$  is small. Other details 444  
of the experimental settings are deferred to the supplementary document. 445

### 3.2 Results for synthetic data 446

**RtEstim** overall outperforms the other competitors in the experimental study. Fig 3 and 447  
Fig 4 visualize the KL divergence across the seven methods. For low incidence in 448  
measles epidemics, **RtEstim** is the most accurate for all  $\mathcal{R}_t$  scenarios given both Poisson 449  
and negative binomial incidence. The best performance of **RtEstim** has the lowest 450  
median and has low or no overlap with other methods. For Scenario 1, **EpiFilter** is a 451  
competitive alternative given Poisson incidence, which has similar median to the best 452  
performance of our **RtEstim** and with a small variation. While given negative binomial 453  
incidence, **EpiFilter** loses its advantage and even has the largest medians in Scenarios 1 454  
and 2. The large incidence in SARS epidemics imposes more difficulty of  $\mathcal{R}_t$  estimation 455  
for all methods. The best performance of our method is quite robust in the scale of 456  
incidence given Poisson data, since the KL values are of the similar scale for two types 457  
of epidemics. Given negative binomial incidence, **EpiLPS** shows robustness in the scale 458  
of incident cases in Scenarios 2 and 4. Our **RtEstim** has similar KL divergence values as 459  
**EpiLPS**, where the counterpart boxes overlap to a large degree. We will examine a single 460  
realization of each experiment to investigate these global conclusions in more detail. 461

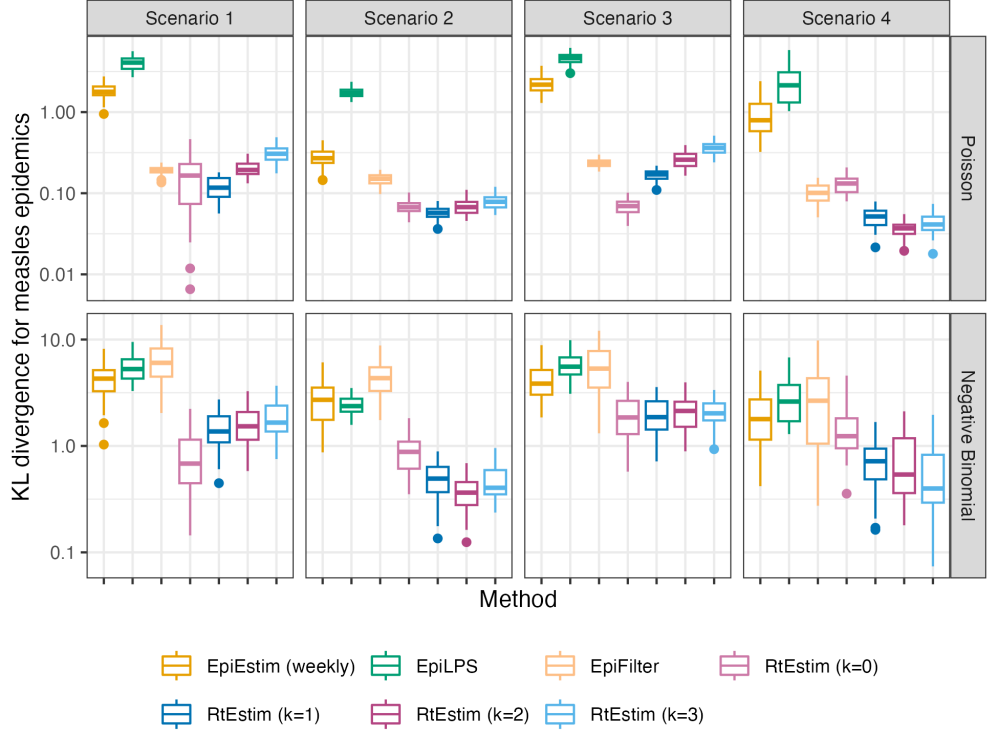


**Fig 3.** Boxplot of mean KL divergence between the estimated  $\hat{\mathcal{R}}_t$  and the true  $\mathcal{R}_t$  across 50 synthetic **measles** epidemics for each approach given Poisson incidence (*in top panels*) and negative binomial incidence (*in bottom panels*) respectively. The mean KL divergence ignores the first weeks in all experiments, since EpiEstim with the weekly sliding window does not provide estimates for the first week. Outliers beyond  $1.5 \times \text{IQR}$  of each box are excluded, and full illustration in provided in the Figure A.3.1 in the supplementary document.

Fig 5 shows one realization for the estimated effective reproduction number under the Poisson generative model in measles synthetic epidemics for all four scenarios. An expanded visualization with each estimated  $\mathcal{R}_t$  curve displayed in a separate panel is provided in Figure A.6.1 in the supplementary document. Compared to EpiEstim and EpiLPS, which have rather severe difficulties at the beginning of the time series with unreasonably large estimates at the beginning and decreases rapidly, RtEstim and EpiFilter estimates are more accurate without suffering from the initialization problem. Besides the edge problem, EpiEstim and EpiLPS produce “smooth” estimated curves that are continuous at the changepoint, which results in large mistakes in that neighbourhood. Since the piecewise constant RtEstim estimator does not force any smoothness in  $\mathcal{R}_t$ , it easily captures the sharp change and nearly overlaps with the true values. RtEstim also suffers from the difficulty to estimate the first few timepoints,

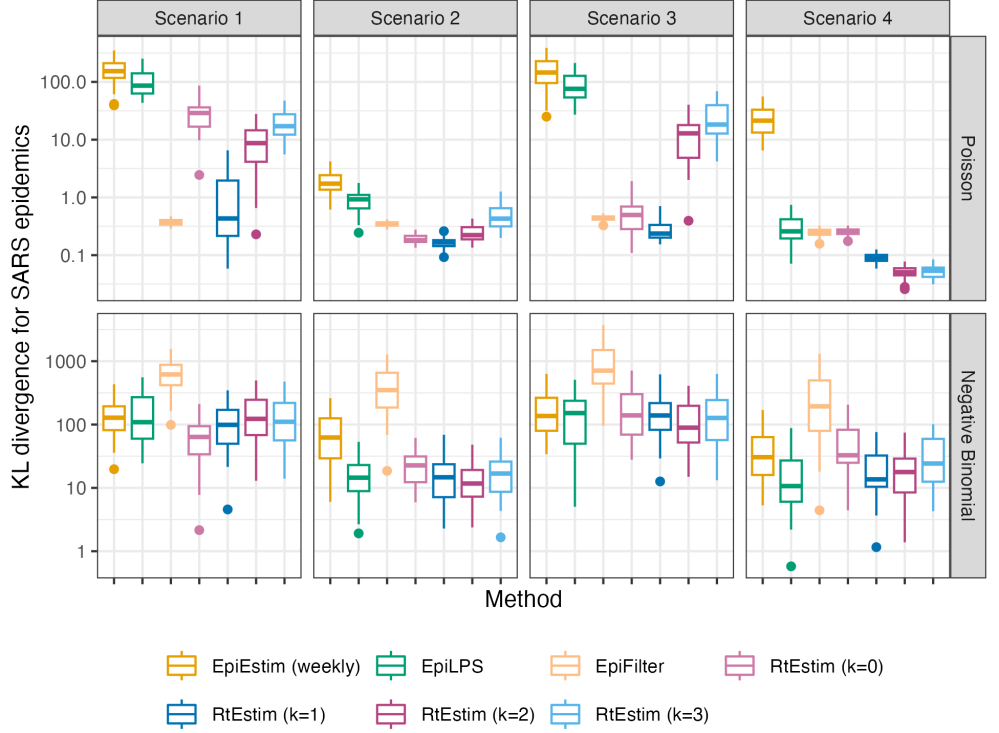


**Fig 4.** Boxplot of mean KL divergence between the estimated  $\hat{\mathcal{R}}_t$  and the true  $\mathcal{R}_t$  across 50 synthetic **SARS** epidemics for each approach given Poisson incidence (*in top panels*) and negative binomial incidence (*in bottom panels*) respectively. The mean KL divergence ignores the first weeks in all experiments, since EpiEstim with the weekly sliding window does not provide estimates for the first week. Outliers beyond  $1.5 \times \text{IQR}$  of each box are excluded, and full illustration in provided in the Figure A.3.1 in the supplementary document.

especially in the periodic case, where all methods miss to capture the first peak with an  
474 accurate value. Ignoring the start of the epidemics, all methods look accurate and  
475 recover the underlying curves quite well, except EpiEstim with monthly sliding  
476 windows, where the trajectories are shifted to the right.  
477

Fig 6 shows a realization of the estimated  $\mathcal{R}_t$  given negative binomial incidence in  
478 SARS epidemics for each setting. An expanded visualization with each estimated  $\mathcal{R}_t$   
479 curve displayed in a separate panel is provided in Figure A.6.4 in the supplementary  
480 document. Compared to the measles epidemics with Poisson data, all methods perform  
481 worse overall for SARS epidemics with negative binomial incidence due to two possible  
482 reasons, larger incidence and overdispersed data. The challenges to recover the start of  
483 epidemics are even harder in this setting for all methods. EpiFilter has much more  
484 wiggly estimates in this setting than the estimates of other methods compared to the  
485

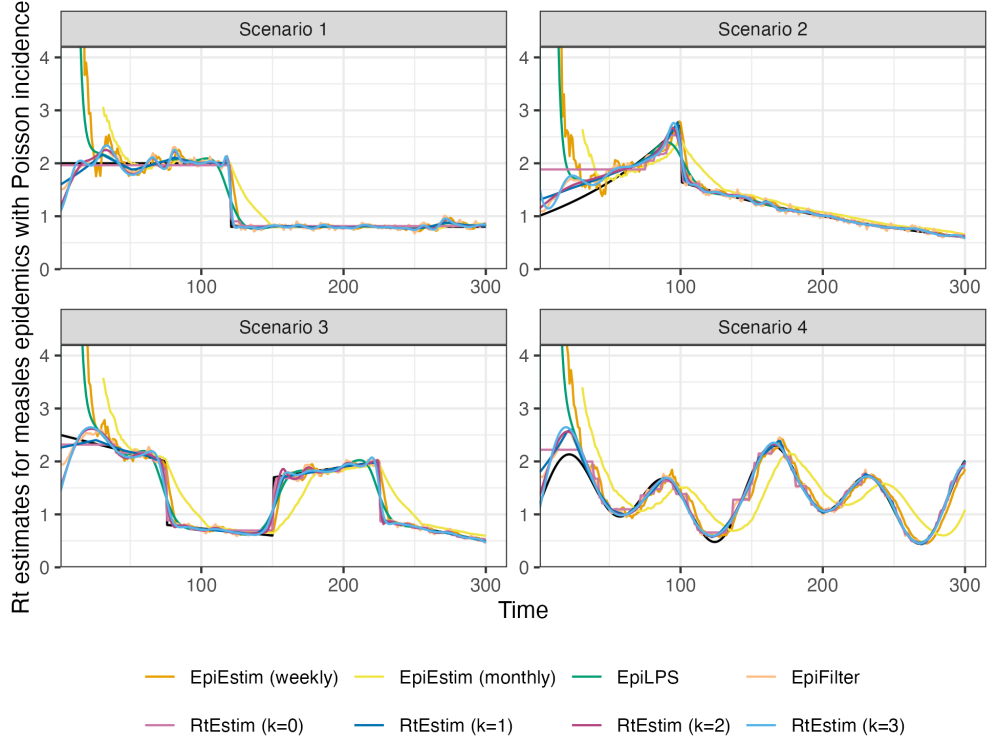


**Fig 5.** Example of effective reproduction number estimation for **measles** epidemics with **Poisson** observations. An expanded visualization with each estimated  $\mathcal{R}_t$  curve displayed in a separate panel is provided in Figure A.6.1 in the supplementary document.

setting in Fig 5. Our **RtEstim** estimates are close to the best performance in the first three  $\mathcal{R}_t$  scenarios, while face the challenge to recover the curve in the periodic scenario.

Finally, it is important to provide a brief comparison of the running times of all three models across the 8 experimental settings. We find that almost all models across all experiments complete within 10 seconds. **RtEstim** generally takes the longest, due to a relatively large number of estimates—50 values of  $\lambda$  and 10 folds of cross validation require 550 estimates—while other models run only a single time for a fixed setting of hyperparameters per experiment. Additional results on timing comparisons are deferred to the supplementary document.

### 3.3 Real-data results: Covid-19 incident cases in Canada

We implement **RtEstim** on Covid-19 confirmed incident cases in Canada (visualized in Fig 1). We use the weighted probabilities of serial interval distributions of four dominant variants used in Fig 1 as the serial interval distribution here for the

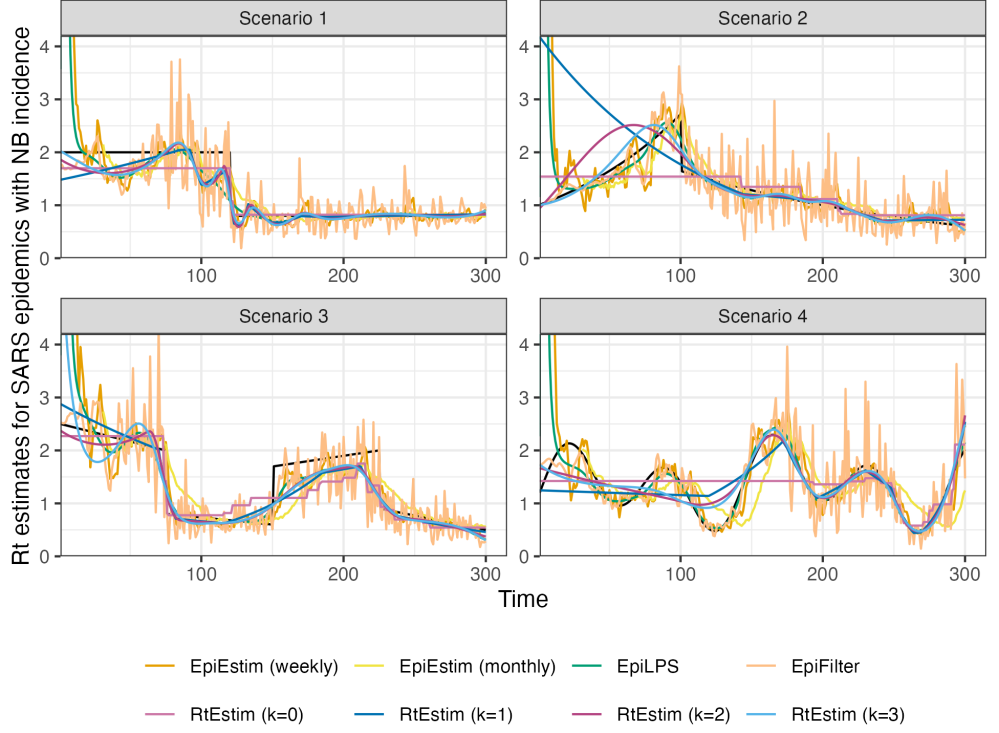


**Fig 6.** Example of effective reproduction number estimation for **SARS** epidemics with **negative binomial** observations. An expanded visualization with each estimated  $\mathcal{R}_t$  curve displayed in a separate panel is provided in Figure A.6.4 in the supplementary document.

comparison with other methods, which cannot incorporate time-varying serial interval distributions. We compute their percentages of days that they dominated throughout the pandemic as the weights in computation, specifically Ancestral lineage (32.6%), Alpha (8.5%), Delta (16.0%), and Omicron(42.9%) with sum 1. The estimates of our method is displayed in Fig 7, and the estimates of all competitors are deferred to Figures A.8.1 and A.8.2 in the supplementary document.

Considering the first, second, and third polynomial degrees,  $\hat{\mathcal{R}}_t$  for Covid-19 in Canada is always less than 2 except at the very early stage, which means that one distinct infected individual on average infects less than two other individuals in the population. Examining three different settings for  $k$ , the temporal evolution of  $\hat{\mathcal{R}}$  (across all regularization levels  $\lambda$ ) are similar near the highest peak around the end of 2021 before dropping shortly thereafter. Throughout the estimated curves, the peaks and troughs of the effective reproduction numbers precede the growth and decay cycles of confirmed cases, as expected. We also visualize 95% confidence bands for the point

estimates with  $\lambda$  chosen by minimizing cross-validated KL divergence in Fig 7.

513

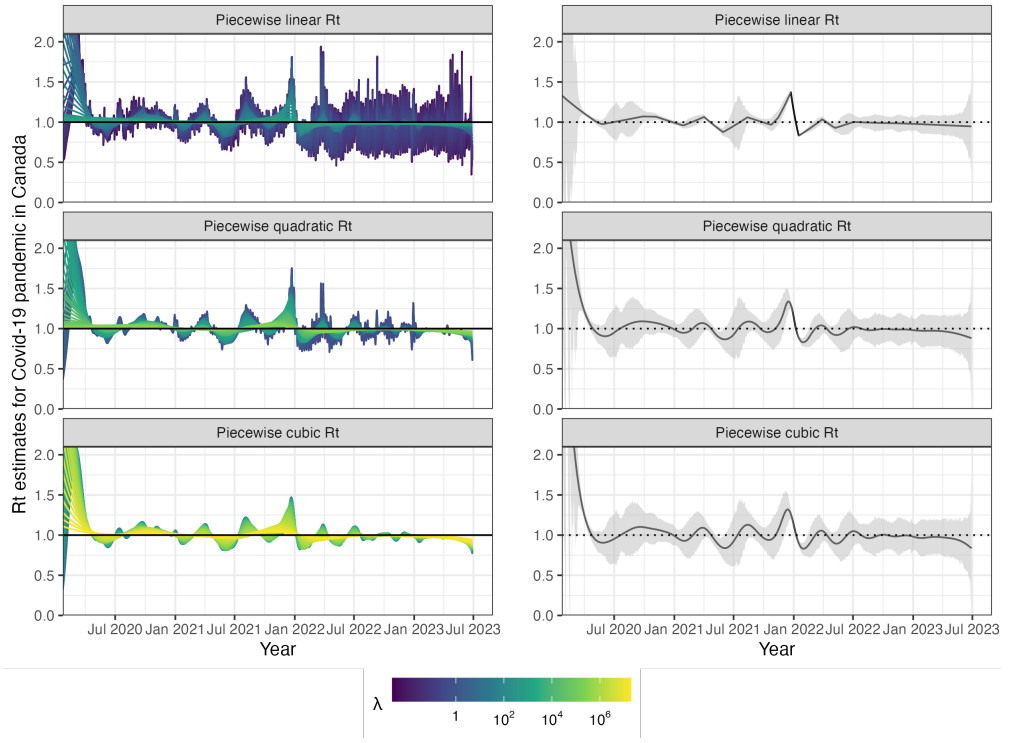


**Fig 7.** Estimated effective reproduction number based on Covid-19 daily confirmed incident cases between January 23rd, 2020 and June 28th, 2023 in Canada. The left panels show estimates corresponding to 50 tuning parameters. The right panels show the CV-tuned estimate along with approximate 95% confidence bands. The top, middle and bottom panels show the estimated  $R_t$  using the Poisson trend filtering in Eq (5) with degrees  $k = 1, 2, 3$  respectively. All estimates are fitted using a constant serial interval distribution, which is the weighted sum of probabilities of the 4 dominant variants per timepoint used in Fig 1. All panels are truncated in y-axes for better illustration. The CV-tuned  $R_t$  estimates rapidly decrease at the early stage from 3.37, 5.16 in  $R_t$  curves with  $k = 2, 3$  respectively.

The estimated effective reproduction numbers are relatively unstable before April, 514  
2022. The highest peak coincides with the emergence and global spread of the Omicron 515  
variant. The estimated effective reproduction numbers fall below 1 during a few time 516  
periods, where the most obvious troughs are roughly from April 2021 to July 2021 and 517  
from January, 2022 to April 2022. The first trough coincides with the introduction of 518  
Covid-19 vaccines in Canada. The second trough, shortly after the largest peak may be 519  
due to variety of factors resulting in the depletion of the susceptible population such as 520  
increased self-isolation in response to media coverage of the peak or immunity incurred 521  
via recent infection. Since April 2022, the estimated effective reproduction number has 522  
remained relatively stable (fluctuating around one) corresponding to low reported cases, 523

though reporting behaviours also changed significantly since the Omicron wave. 524

### 3.4 Real-data results: influenza in Baltimore, Maryland, 1918 525

We also apply `RtEstim` to daily reported influenza cases in Baltimore, Maryland 526 occurring during the world-wide pandemic of 1918 from September to November [44]. 527 The data, shown in Fig 8, is included in the `EpiEstim` R package. We use the serial 528 interval distribution provided by the `EpiEstim` R package for this pandemic in 529 modelling. The 1918 influenza outbreak, caused by the H1N1 influenza A virus, was 530 unprecedently deadly with case fatality rate over 2.5%, infecting almost one-third of 531 the population across the world [45]. The CV-tuned piecewise cubic estimates in Fig 9 532 better capture the growth at the beginning of the pandemic in Fig 8. The estimated  $\mathcal{R}_t$  533 curve suggests that the transmissibility of the pandemic grew rapidly over the first 534 30 days before declining below one after 50 days. However, it also suggests an increase in 535 infectiousness toward the end of the period. With this data, it is difficult to determine if 536 there is a second wave or a steady decline ahead. The CV-tuned piecewise constant and 537 linear estimates in Fig 9 both suggest a steady decline. This conclusion is supported by 538 the fact that incident cases decline to zero at the end of the period and matches  $\mathcal{R}$  539 estimates in [10], which are all lower than one. The estimation using alternatives is 540 deferred to Figures A.8.3 and A.8.4 in the supplementary document. 541

## 4 Discussion 542

The `RtEstim` methodology provides a locally adaptive estimator using Poisson trend 543 filtering on univariate data. It captures the heterogeneous smoothness of effective 544 reproduction numbers given observed incidence data rather than resulting in global 545 smoothness. This is a nonparametric regression model which can be written as a convex 546 optimization (minimization) problem. Minimizing the distance (KL divergence across 547 all coordinates) between the estimators and (functions of) observations guarantees data 548 fidelity while the penalty on divided differences between pairs of neighbouring 549 parameters imposes smoothness. The  $\ell_1$ -regularization results in sparsity of the divided 550 differences, which leads to heterogeneous smoothness across time. 551

The property of local adaptivity (heterogenous smoothness) is useful to 552

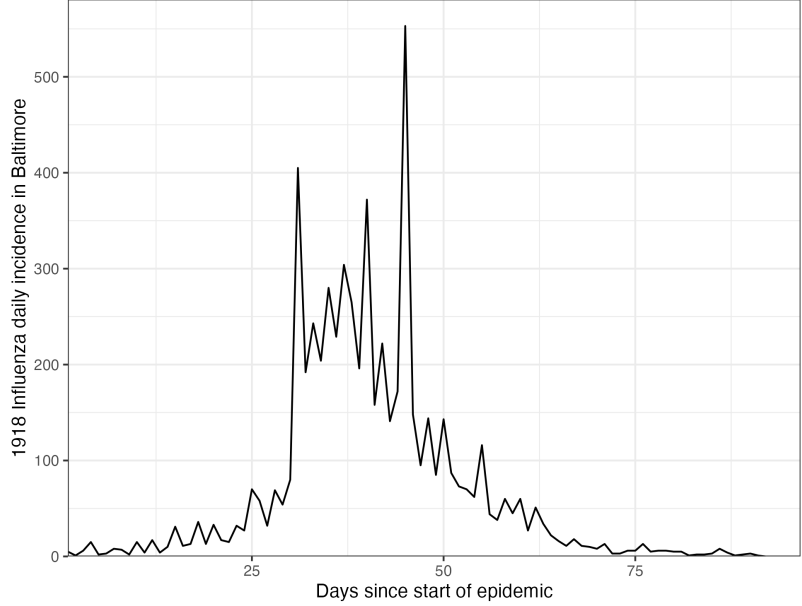


**Fig 8.** Daily incident influenza cases in Baltimore, Maryland between September and November in 1918.

automatically distinguish, for example, seasonal outbreaks from outbreaks driven by  
other factors (behavioural changes, foreign introduction, etc.). Given a well-chosen  
polynomial degree, the growth rates can be quickly detected, potentially advising public  
health authorities to implement policy changes. The effective reproduction numbers can  
be estimated retrospectively to examine the efficacy of such policies, whether they result  
in  $\mathcal{R}_t$  falling below 1 or the speed of their effects. The smoothness of  $\mathcal{R}_t$  curves  
(including the polynomial degrees and tuning parameters) should be chosen based on  
the purpose of the study in practice.

Our method `RtEstim` provides a natural way to deal with missing data, for example,  
on weekends and holidays or due to changes in reporting frequency. While solving the  
convex optimization problem, our method can easily handle uneven spacing or irregular  
reporting. Computing the total primary infectiousness is also easily generalized to  
irregular reporting by modifying the discretization of the serial interval distribution.  
There are many other aspects to be considered in choosing the delay distribution to  
make a more accurate estimation [46]. Imported cases can be distinguished from the  
local cases to avoid the biasness in effective reproduction number estimation, for  
example, [11] assumed the total past infectiousness of combined previous cases scaled by  
effective reproduction number to be the mean of the local incidence and illustrated that

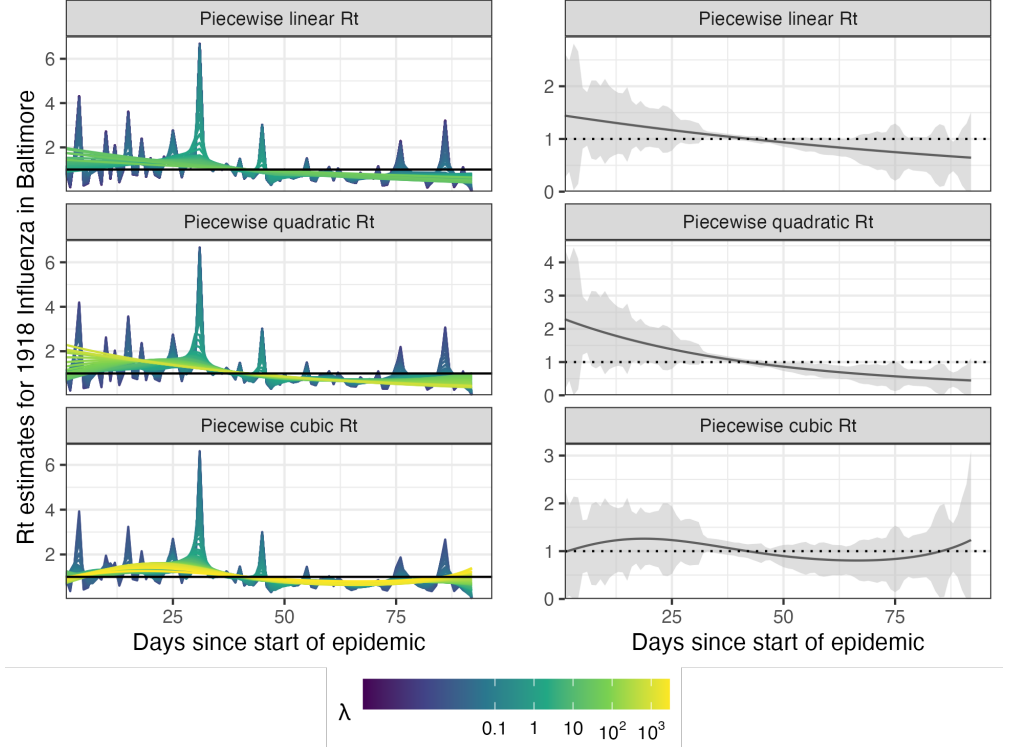


**Fig 9.** Estimated effective reproduction numbers for influenza in Baltimore, Maryland in 1918. The left panels show estimates for a set of 50 tuning parameters. The right column displays the CV-tuned estimates with approximate 95% confidence bands. The rows (top to bottom) show estimated effective reproduction numbers ( $\mathcal{R}_t$ ) using the Poisson trend filtering in Eq (5) with  $k = 1, 2, 3$  respectively.

failure of distinguishing the local cases from the imported cases may cause the  
 overestimation of  $\mathcal{R}$  using the MERS data in Saudi Arabia from August 2014 to  
 December 2015. Additionally, because the  $\ell_1$  penalty introduces sparsity (operating like  
 a median rather than a mean), this procedure is relatively insensitive to outliers  
 compared to  $\ell_2$  regularization.

There are a number of limitations that may influence the quality of  $\mathcal{R}_t$  estimation.  
 While our model is generic for incidence data rather than tailored to any specific  
 disease, it does assume that the generation interval is short relative to the period of  
 data collection. More specialized methodologies would be required for diseases with long  
 incubation periods such as HIV or Hepatitis. Our approach, does not explicitly model  
 imported cases, nor distinguish between subpopulations that may have different mixing  
 behaviour. While the Poisson assumption is common, it does not handle overdispersion  
 (observation variance larger than the mean). The negative binomial distribution is a

good alternative, but more difficult to estimate in this context. As described in 584  
section 1, the expression for  $\mathcal{R}$  assumes that a relatively constant proportion of true 585  
infections is reported. However, if this proportion varies with time (say, due to changes 586  
in surveillance practices or testing recommendations), the estimates may be biased over 587  
this window. A good example is in early January 2022, during the height of the 588  
Omicron wave, Canada moved from testing all symptomatic individuals to testing only 589  
those in at-risk groups. The result was a sudden change that would render  $\mathcal{R}_t$  estimates 590  
on either side of this timepoint incommensurable. 591

Our **RtEstim** implementation can take a fixed serial interval throughout the period 592  
of study (as implemented in simulation and in the real epidemics) or varying serial 593  
interval distributions at different timepoints (as implemented in Fig 1 for Covid-19 data 594  
in Canada). In reality, the serial interval may vary due to changes in the factors such as 595  
population immunity [12]. An issue regarding the serial interval distribution relates to 596  
equating serial and generation intervals (also mentioned above). The serial interval 597  
distribution is generally wider than that of the generation interval, because the serial 598  
interval involves the convolution of two distributions, and is unlikely to actually follow a 599  
named distribution like Gamma, though it may be reasonably well approximated by one. 600  
Our implementation allows for an arbitrary distribution to be used, but requires the 601  
user to specify the discretization explicitly, requiring more nuanced knowledge than is 602  
typically available. Pushing this analysis further, to accommodate other types of 603  
incidence data (hospitalizations or deaths), a modified generation interval distribution 604  
would be necessary, and further assumptions would be required as well. Or else, one 605  
would first need to deconvolve deaths to infection onset before using our software. 606

Nonetheless, our methodology is implemented in a lightweight R package **rtestim** 607  
and computed efficiently, especially for large-scale data, with a proximal Newton solver 608  
coded in C++. Given available incident case data, prespecified serial interval distribution, 609  
and a choice of degree  $k$ , **RtEstim** is able to produce accurate estimates of effective 610  
reproduction number and provide efficient tuning parameter selection via cross 611  
validation. 612

## Acknowledgments

613

This research was enabled in part by support provided by BC DRI group who manages Cedar cloud (<https://docs.alliancecan.ca/wiki/Cedar>) and the Digital Research Alliance of Canada ([alliancecan.ca](http://alliancecan.ca)).  
614  
615  
616

## References

1. Gostic KM, McGough L, Baskerville EB, Abbott S, Joshi K, Tedijanto C, et al. Practical considerations for measuring the effective reproductive number,  $R_t$ . PLoS Computational Biology. 2020;16(12):e1008409.
2. Nishiura H, Chowell G. The effective reproduction number as a prelude to statistical estimation of time-dependent epidemic trends. Mathematical and statistical estimation approaches in epidemiology. 2009; p. 103–121.
3. Fraser C. Estimating individual and household reproduction numbers in an emerging epidemic. PloS one. 2007;2(8):e758.
4. Anderson RM, May RM. Infectious diseases of humans: dynamics and control. Oxford university press; 1991.
5. Wallinga J, Teunis P. Different epidemic curves for severe acute respiratory syndrome reveal similar impacts of control measures. American Journal of epidemiology. 2004;160(6):509–516.
6. Hao X, Cheng S, Wu D, Wu T, Lin X, Wang C. Reconstruction of the full transmission dynamics of COVID-19 in Wuhan. Nature. 2020;584(7821):420–424.
7. Goldstein IH, Parker DM, Jiang S, Minin VM. Semiparametric inference of effective reproduction number dynamics from wastewater pathogen surveillance data. arXiv preprint arXiv:230815770. 2023;.
8. Goldstein IH, Wakefield J, Minin VM. Incorporating testing volume into estimation of effective reproduction number dynamics. Journal of the Royal Statistical Society Series A: Statistics in Society. 2024;187(2):436–453.

9. Cori A, Cauchemez S, Ferguson NM, Fraser C, Dahlqvist E, Demarsh PA, et al.. EpiEstim: estimate time varying reproduction numbers from epidemic curves; 2020.
10. Cori A, Ferguson NM, Fraser C, Cauchemez S. A new framework and software to estimate time-varying reproduction numbers during epidemics. *American Journal of Epidemiology*. 2013;178(9):1505–1512.
11. Thompson RN, Stockwin JE, van Gaalen RD, Polonsky JA, Kamvar ZN, Demarsh PA, et al. Improved inference of time-varying reproduction numbers during infectious disease outbreaks. *Epidemics*. 2019;29:100356.
12. Nash RK, Bhatt S, Cori A, Nouvellet P. Estimating the epidemic reproduction number from temporally aggregated incidence data: A statistical modelling approach and software tool. *PLoS Computational Biology*. 2023;19(8):e1011439.
13. Abbott S, Funk S, Hickson J, Badr HS, Monticone P, Ellis P, et al.. epiforecasts/EpiNow2: 1.4.0 release; 2023.
14. Abbott S, Hellewell J, Thompson RN, Sherratt K, Gibbs HP, Bosse NI, et al. Estimating the time-varying reproduction number of SARS-CoV-2 using national and subnational case counts. *Wellcome Open Research*. 2020;5:112.
15. Lison A, Abbott S, Huisman J, Stadler T. Generative Bayesian modeling to nowcast the effective reproduction number from line list data with missing symptom onset dates. *PLoS Computational Biology*. 2024;20(4):e1012021.
16. Parag KV. Improved estimation of time-varying reproduction numbers at low case incidence and between epidemic waves. *PLoS Computational Biology*. 2021;17(9):e1009347.
17. Gressani O, Wallinga J, Althaus CL, Hens N, Faes C. EpiLPS: A fast and flexible Bayesian tool for estimation of the time-varying reproduction number. *PLoS Computational Biology*. 2022;18(10):e1010618.
18. Trevisin C, Bertuzzo E, Pasetto D, Mari L, Miccoli S, Casagrandi R, et al. Spatially explicit effective reproduction numbers from incidence and mobility data. *Proceedings of the National Academy of Sciences*. 2023;120(20):e2219816120.

19. Abry P, Pustelnik N, Roux S, Jensen P, Flandrin P, Gribonval R, et al. Spatial and temporal regularization to estimate COVID-19 reproduction number  $R(t)$ : Promoting piecewise smoothness via convex optimization. *PLoS ONE*. 2020;15(8):e0237901.
20. Pascal B, Abry P, Pustelnik N, Roux S, Gribonval R, Flandrin P. Nonsmooth convex optimization to estimate the Covid-19 reproduction number space-time evolution with robustness against low quality data. *IEEE Transactions on Signal Processing*. 2022;70:2859–2868.
21. Pircalabelu E. A spline-based time-varying reproduction number for modelling epidemiological outbreaks. *Journal of the Royal Statistical Society Series C: Applied Statistics*. 2023;72(3):688–702.
22. Ho F, Parag KV, Adam DC, Lau EH, Cowling BJ, Tsang TK. Accounting for the Potential of Overdispersion in Estimation of the Time-varying Reproduction Number. *Epidemiology*. 2023;34(2):201–205.
23. Azmon A, Faes C, Hens N. On the estimation of the reproduction number based on misreported epidemic data. *Statistics in Medicine*. 2014;33(7):1176–1192.
24. Gressani O, Faes C, Hens N. An approximate Bayesian approach for estimation of the instantaneous reproduction number under misreported epidemic data. *Biometrical Journal*. 2022;65(6):2200024.
25. Jin S, Dickens BL, Lim JT, Cook AR. EpiMix: A novel method to estimate effective reproduction number. *Infectious Disease Modelling*. 2023;8(3):704–716.
26. Hettinger G, Rubin D, Huang J. Estimating the instantaneous reproduction number with imperfect data: a method to account for case-reporting variation and serial interval uncertainty. *arXiv preprint arXiv:230212078*. 2023;.
27. Berry I, O'Neill M, Sturrock SL, Wright JE, Acharya K, Brankston G, et al. A sub-national real-time epidemiological and vaccination database for the COVID-19 pandemic in Canada. *Scientific Data*. 2021;8(1). doi:10.1038/s41597-021-00955-2.

28. Coronavirus Variants Rapid Response Network Computational Analysis M, Group EOC. CoVaRR-NET/duotang: Release for Zenodo Archive; 2023. Available from: <https://doi.org/10.5281/zenodo.10367461>.
29. Xu X, Wu Y, Kummer AG, Zhao Y, Hu Z, Wang Y, et al. Assessing changes in incubation period, serial interval, and generation time of SARS-CoV-2 variants of concern: a systematic review and meta-analysis. *BMC medicine*. 2023;21(1):374.
30. Park SW, Sun K, Champredon D, Li M, Bolker BM, Earn DJ, et al. Forward-looking serial intervals correctly link epidemic growth to reproduction numbers. *Proceedings of the National Academy of Sciences*. 2021;118(2):e2011548118.
31. Pitzer VE, Chitwood M, Havumaki J, Menzies NA, Perniciaro S, Warren JL, et al. The impact of changes in diagnostic testing practices on estimates of COVID-19 transmission in the United States. *American Journal of Epidemiology*. 2021;190(9):1908–1917.
32. Hitchings MD, Dean NE, García-Carreras B, Hladish TJ, Huang AT, Yang B, et al. The usefulness of the test-positive proportion of severe acute respiratory syndrome coronavirus 2 as a surveillance tool. *American Journal of Epidemiology*. 2021;190(7):1396–1405.
33. Pellis L, Scarabel F, Stage HB, Overton CE, Chappell LH, Fearon E, et al. Challenges in control of COVID-19: short doubling time and long delay to effect of interventions. *Philosophical Transactions of the Royal Society B*. 2021;376(1829):20200264.
34. Kim SJ, Koh K, Boyd S, Gorinevsky D.  $\ell_1$  trend filtering. *SIAM Review*. 2009;51(2):339–360.
35. Tibshirani RJ. Adaptive piecewise polynomial estimation via trend filtering. *The Annals of Statistics*. 2014;42(1):285–323.
36. Tibshirani RJ. Divided differences, falling factorials, and discrete splines: Another look at trend filtering and related problems. *Foundations and Trends® in Machine Learning*. 2022;15(6):694–846.

37. Sadhanala V, Bassett R, Sharpnack J, McDonald DJ. Exponential family trend filtering on lattices. *Electronic Journal of Statistics*. 2024;18(1):1749–1814.
38. Vaiter S, Deledalle C, Fadili J, Peyré G, Dossal C. The degrees of freedom of partly smooth regularizers. *Annals of the Institute of Statistical Mathematics*. 2017;69:791–832.
39. Cori A, Kamvar Z, Stockwin J, Jombart T, Dahlqwist E, FitzJohn R, et al.. EpiEstim v2.2-4: A tool to estimate time varying instantaneous reproduction number during epidemics; 2022. <https://github.com/mrc-ide/EpiEstim>.
40. Gressani O. EpiLPS: A Fast and Flexible Bayesian Tool for Estimating Epidemiological Parameters.; 2021. <https://epilps.com/>.
41. Parag KV. EpiFilter; 2020.  
<https://github.com/kpzoo/EpiFilter?tab=readme-ov-file>.
42. Groendyke C, Welch D, Hunter DR. Bayesian inference for contact networks given epidemic data. *Scandinavian Journal of Statistics*. 2011;38(3):600–616.
43. Lipsitch M, Cohen T, Cooper B, Robins JM, Ma S, James L, et al. Transmission dynamics and control of severe acute respiratory syndrome. *science*. 2003;300(5627):1966–1970.
44. Frost WH, Sydenstricker E. Influenza in Maryland: preliminary statistics of certain localities. *Public Health Reports (1896-1970)*. 1919; p. 491–504.
45. Taubenberger JK, Morens DM. 1918 Influenza: the mother of all pandemics. *Emerging Infectious Diseases*. 2006;17(1):69–79.
46. Park SW, Akhmetzhanov AR, Charniga K, Cori A, Davies NG, Dushoff J, et al. Estimating epidemiological delay distributions for infectious diseases. *medRxiv*. 2024; p. 2024–01.

# Supplementary details on experiments of effective reproduction number estimation with trend filtering

Jiapeng Liu, Zhenglun Cai, Paul Gustafson, and Daniel J. McDonald

## A.1 Derivation of Kullback Leibler divergence for accuracy comparison

We provide the detailed derivation of the Kullback Leibler (KL) divergence in (11) that is used to compare the accuracy of the estimated effective reproduction number with the true ones. Given the total infectiousness  $\eta$ , we compare the distance between the Poisson distributions  $f_1(y; \eta, \hat{\mathcal{R}}) = Pois(\eta\hat{\mathcal{R}})$  and  $f_0(y; \eta, \mathcal{R}) = Pois(\eta\mathcal{R})$ , where  $y, \mathcal{R} \in \mathbb{N}_0^n$  are natural numbers including 0,  $\eta \in \mathbb{R}^n$ ,  $f_0(y) = \prod_{t=1}^n \frac{(\eta_t \mathcal{R}_t)^{y_t} e^{-\eta_t \mathcal{R}_t}}{y_t!}$ ,  $f_1(y) = \prod_{t=1}^n \frac{(\eta_t \hat{\mathcal{R}}_t)^{y_t} e^{-\eta_t \hat{\mathcal{R}}_t}}{y_t!}$ ,  $y_t \in \mathbb{N}_0 = \{0, 1, 2, \dots\}$ . Then, the KL divergence between them is defined as

$$\begin{aligned}
D_{KL}(\mathcal{R} || \hat{\mathcal{R}}) &= D_{KL}(f_0(y) || f_1(y)) \\
&= \sum_{y \in \mathbb{N}_0^n} f_0(y) \log \frac{f_0(y)}{f_1(y)} \\
&= \sum_{y \in \mathbb{N}_0^n} \prod_{t=1}^n \frac{(\eta_t \mathcal{R}_t)^{y_t} e^{-\eta_t \mathcal{R}_t}}{y_t!} \log \prod_{t=1}^n \frac{\mathcal{R}_t^{y_t} e^{-\eta_t \mathcal{R}_t}}{\hat{\mathcal{R}}_t^{y_t} e^{-\eta_t \hat{\mathcal{R}}_t}} \\
&= \sum_{y_n=0}^{\infty} \dots \sum_{y_1=0}^{\infty} \prod_{t=1}^n \frac{(\eta_t \mathcal{R}_t)^{y_t} e^{-\eta_t \mathcal{R}_t}}{y_t!} \sum_{t=1}^n \left( y_t \log \frac{\mathcal{R}_t}{\hat{\mathcal{R}}_t} - \eta_t (\mathcal{R}_t - \hat{\mathcal{R}}_t) \right) \text{ for independent } y_t, t = 1, \dots, n \\
&= \sum_{y_n=0}^{\infty} \frac{(\eta_n \mathcal{R}_n)^{y_n} e^{-\eta_n \mathcal{R}_n}}{y_n!} \dots \sum_{y_1=0}^{\infty} \frac{(\eta_1 \mathcal{R}_1)^{y_1} e^{-\eta_1 \mathcal{R}_1}}{y_1!} \left( y_1 \log \frac{\mathcal{R}_1}{\hat{\mathcal{R}}_1} + \sum_{t=2}^n y_t \log \frac{\mathcal{R}_t}{\hat{\mathcal{R}}_t} - \sum_{t=1}^n \eta_t (\mathcal{R}_t - \hat{\mathcal{R}}_t) \right) \\
&= \sum_{y_n=0}^{\infty} \frac{(\eta_n \mathcal{R}_n)^{y_n} e^{-\eta_n \mathcal{R}_n}}{y_n!} \dots \sum_{y_2=0}^{\infty} \frac{(\eta_2 \mathcal{R}_2)^{y_2} e^{-\eta_2 \mathcal{R}_2}}{y_2!} \left( \eta_1 \mathcal{R}_1 \log \frac{\mathcal{R}_1}{\hat{\mathcal{R}}_1} + \sum_{t=2}^n y_t \log \frac{\mathcal{R}_t}{\hat{\mathcal{R}}_t} - \sum_{t=1}^n \eta_t (\mathcal{R}_t - \hat{\mathcal{R}}_t) \right) \\
&= \sum_{y_n=0}^{\infty} \frac{(\eta_n \mathcal{R}_n)^{y_n} e^{-\eta_n \mathcal{R}_n}}{y_n!} \left( \sum_{t=1}^{n-1} \eta_t \mathcal{R}_t \log \frac{\mathcal{R}_t}{\hat{\mathcal{R}}_t} + y_n \log \frac{\mathcal{R}_n}{\hat{\mathcal{R}}_n} - \sum_{t=1}^n \eta_t (\mathcal{R}_t - \hat{\mathcal{R}}_t) \right) \\
&= \sum_{t=1}^n \eta_t \left( \mathcal{R}_t \log \frac{\mathcal{R}_t}{\hat{\mathcal{R}}_t} + \hat{\mathcal{R}}_t - \mathcal{R}_t \right),
\end{aligned}$$

where

$$\begin{aligned}
& \sum_{y_1=0}^{\infty} \frac{(\eta_1 \mathcal{R}_1)^{y_1} e^{-\eta_1 \mathcal{R}_1}}{y_1!} \left( y_1 \log \frac{\mathcal{R}_1}{\hat{\mathcal{R}}_1} + \sum_{t=2}^n y_t \log \frac{\mathcal{R}_t}{\hat{\mathcal{R}}_t} - \sum_{t=1}^n \eta_t (\mathcal{R}_t - \hat{\mathcal{R}}_t) \right) \\
&= \left( \sum_{y_1=0}^{\infty} \frac{(\eta_1 \mathcal{R}_1)^{y_1-1} e^{-\eta_1 \mathcal{R}_1}}{(y_1-1)!} \eta_1 \mathcal{R}_1 \log \frac{\mathcal{R}_1}{\hat{\mathcal{R}}_1} \right) + \sum_{t=2}^n y_t \log \frac{\mathcal{R}_t}{\hat{\mathcal{R}}_t} - \sum_{t=1}^n \eta_t (\mathcal{R}_t - \hat{\mathcal{R}}_t) \\
&= \eta_1 \mathcal{R}_1 \log \frac{\mathcal{R}_1}{\hat{\mathcal{R}}_1} + \sum_{t=2}^n y_t \log \frac{\mathcal{R}_t}{\hat{\mathcal{R}}_t} - \sum_{t=1}^n \eta_t (\mathcal{R}_t - \hat{\mathcal{R}}_t).
\end{aligned}$$

We use mean KL divergence (denoted,  $\overline{D_{KL}}(\mathcal{R}||\hat{\mathcal{R}}) := D_{KL}(\mathcal{R}||\hat{\mathcal{R}})/n$ , which is the KL divergence divided by the sequence length) in experiments for accuracy comparison.

## A.2 Supplementary details on experimental settings

We compare the accuracy of the estimated effective reproduction numbers using the mean Kullback Leibler (KL) divergence (with Poisson distributional assumption on incidence) in (10) across our **RtEstim** and several alternative methods including **EpiEstim** with weekly and monthly sliding windows, **EpiLPS**, **EpiFilter**, **EpiNow2**, and **RtEstim** with degrees  $k=0,1,2,3$ , which yields 9 methods in total. We consider two lengths of epidemics with  $n = 50$  or  $n = 300$  timepoints respectively. Since **EpiNow2** runs too long (specifically, for a long **measles** epidemic, it takes almost 2 hours (115 minutes computed on Cedar cluster provided by Compute Canada), we only compare it with other methods for short epidemics.

We consider serial interval (SI) distributions of **measles** and **SARS** to generate long synthetic epidemics, and **flu** for short epidemics, inspired by Cori et al. (2013). The means and standard deviations of SI distributions are estimated by existing literatures; specifically, (14.9, 3.9) for **measles** (Groendyke, Welch, and Hunter (2011)), (8.4, 3.8) for **SARS** (Lipsitch et al. (2003)), and (2.6, 1.5) for **flu** (Ferguson et al. (2005), Boëlle et al. (2011)). Incident cases in synthetic **measles** epidemics are relatively low (within 1000 at the peak overall), and **SARS** incident cases are relatively large (between 15000 and 20000 at the peak overall). We consider a reasonably large overdispersion level of negative Binomial incidence with size 5. Figure A.2.1 displays the ratio of standard deviation over mean (called, sigma to mean ratio) of incidence across different settings using the same set of sample epidemics in Fig 5, Fig 6, and all figures in section A.6.1. Compared to the counterpart of Poisson incidence (which decreases quickly to 0 and remains to be under 0.25) per  $\mathcal{R}_t$  scenario for each epidemic, the negative Binomial incidence appears to have an apparently larger sigma to mean ratio (staying at around 0.5 or above), which implies a distinguishable overdispersion level.

In model fitting, we use both true and misspecified serial interval (SI) distributions to test the robustness of our method, compared to other alternatives. The misspecification of serial interval distributions are either mild or major, where, in the major misspecification, we use a completely different pair of SI parameters, e.g., we use SI of **SARS** to solve measles epidemics, and SI of measles to solve short **flu** epidemics. While, in the mild SI misspecification, we consider slightly adjusted parameters for both **measles** and **flu** epidemics, where the mean is decreased by 2 for **measles** and increased by 2 for **flu** and the standard deviation is increased by 10, denoted as **adj\_flu** and **adj\_measles** respectively. These settings result in 7 pairs of SI distributions (for epidemic generating, model fitting), i.e., (**measles**, **measles**), (**SARS**, **SARS**), (**measles**, **adj\_measles**), (**measles**, **SARS**) for long epidemics and (**flu**, **flu**), (**flu**, **adj\_flu**), (**flu**, **measles**) for short

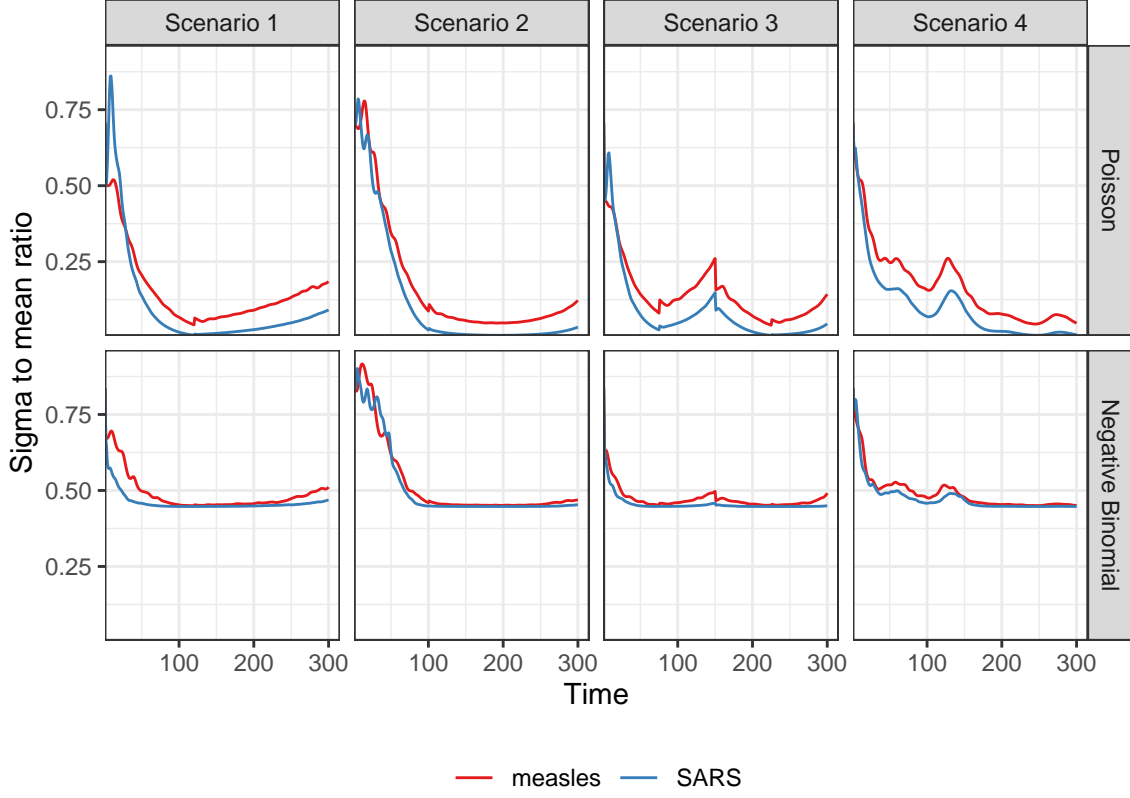


Figure A.2.1: Dispersion level of incidence of sample epidemics

Table 1: Summary of experimental setting on accuracy comparison

Length	SI	Rt scenario	Incidence	SI for modelling	Method
300	measles	1-4	Poisson, NB	measles, adj_measles, SARS	8 methods
300	SARS	1-4	Poisson, NB	SARS	8 methods
50	flu	3	Poisson, NB	flu, adj_flu, measles	9 methods

epidemics. Figure A.2.2 displays all SI distributions (`measles`, `adj_measles`, `SARS`, `flu`, and `adj_flu`) used in the experiments.

Table 1 summarizes the aforementioned experimental setting for accuracy comparison. Poisson and negative Binomial (NB) distributions for incidence and 4  $\mathcal{R}_t$  scenarios are used for all long epidemics. We only consider one  $\mathcal{R}_t$  scenario for short epidemics. Each experimental setting is replicated for 50 times, which yields 12800 experiments for long epidemics and 2700 for short epidemics.

We visualize the selected key results of the accuracy comparison using long synthetic epidemics in Section 3.2. Other main experimental results are displayed in Section A.3.

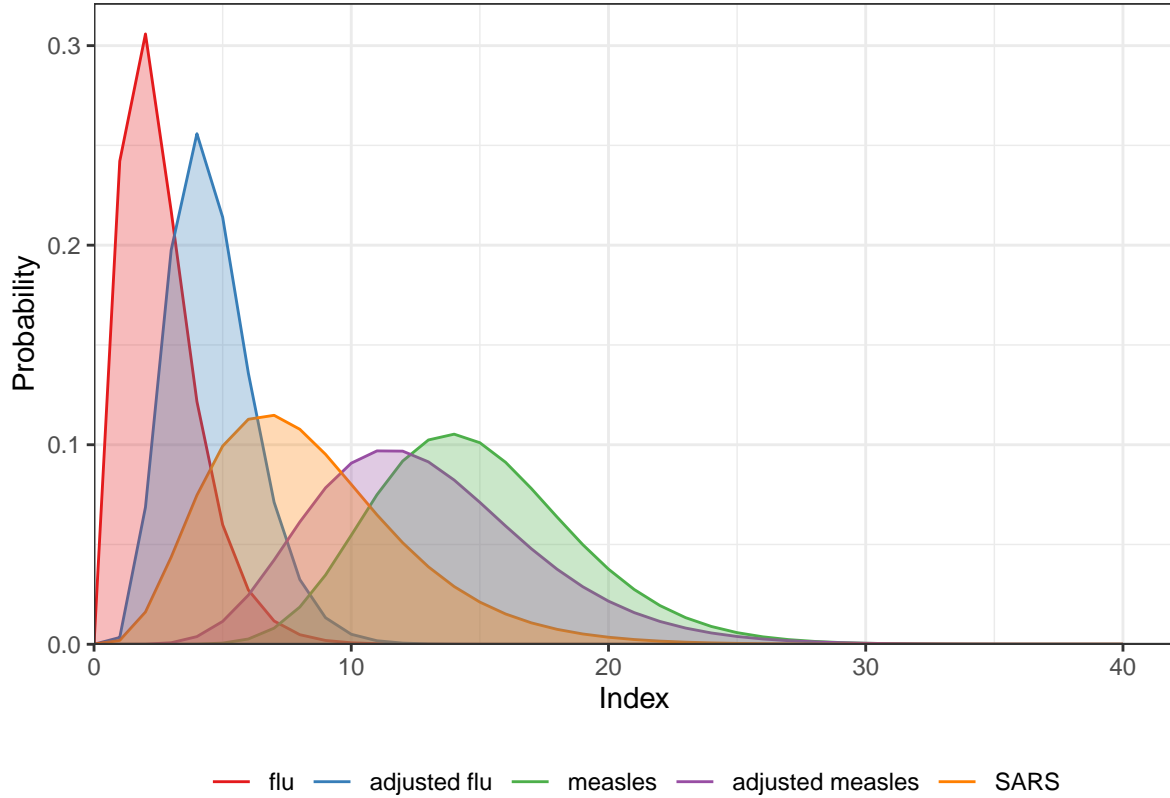


Figure A.2.2: Density curves of serial interval distributions used in the experiments

## A.3 Supplementary experimental results on accuracy comparison

### A.3.1 Long epidemics

We display the accuracy of all methods (where **EpiEstim** uses weekly sliding window) for measles and SARS sample epidemics (by excluding the first weeks in computing KL divergence) in Fig 3 and Fig 4, where we exclude the outliers. A full visualization is in A.3.1.

Figure A.3.2 compares **EpiEstim** with *monthly* sliding windows with other methods. We average the KL divergence per coordinate excluding the timepoints in the first months for all approaches, since **EpiEstim** estimates with the monthly sliding windows are not available until the second months. The *y*-axis is displayed on a logarithmic scale for a better visualization, since a few values are much larger than others.

The relative performance of **EpiEstim** with monthly sliding windows, in general, is not as good as its weekly sliding window based on the relative positions of its boxes and the counterparts of the other methods, except for the Scenario 2 with negative Binomial incidence. It can be explained by **EpiEstim** with longer sliding windows assume similarity of neighbouring  $\mathcal{R}_t$  across longer periods, and thus, is smoother and less accurate compared to the one with shorter sliding windows.

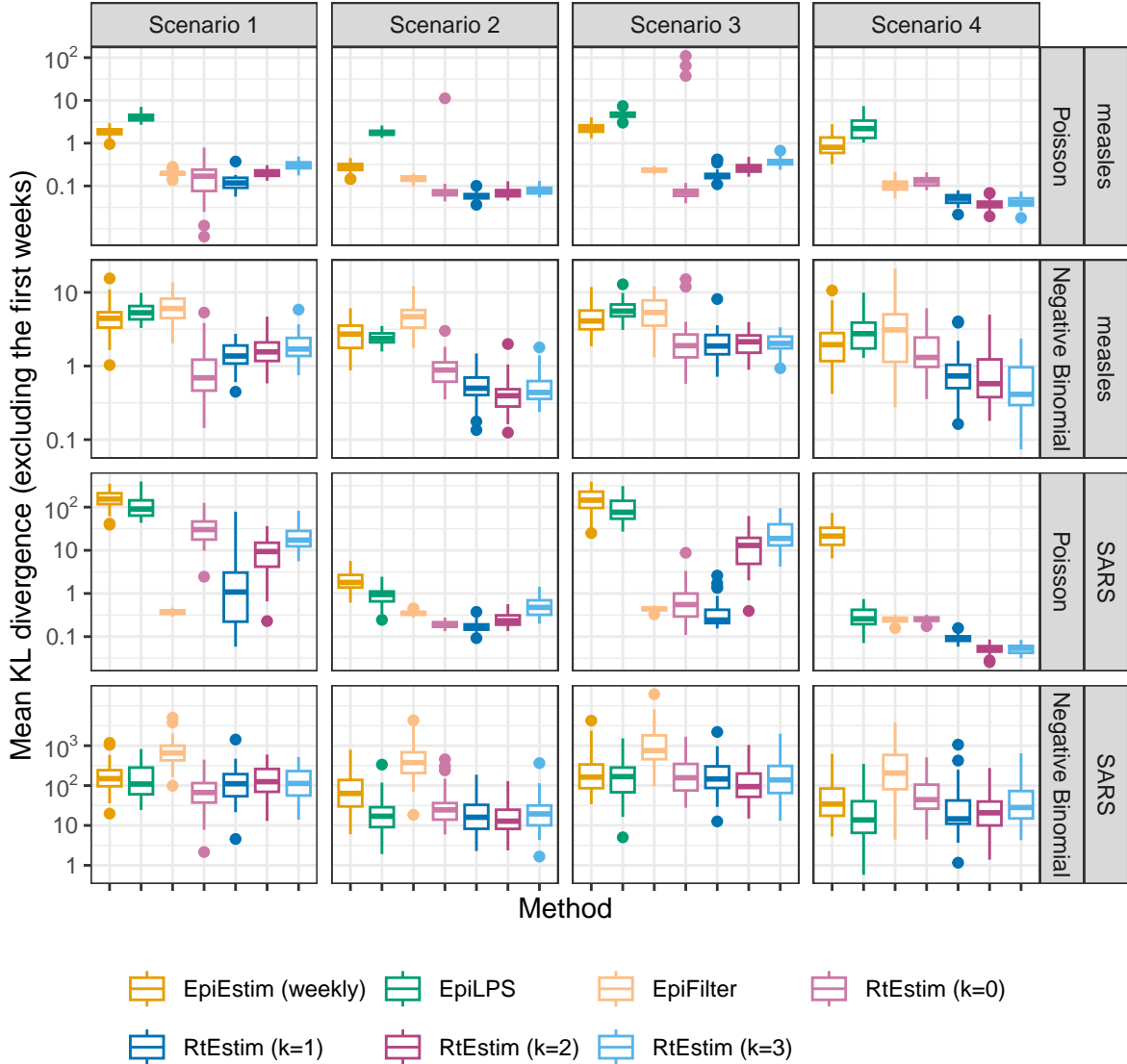


Figure A.3.1: Mean KL divergence excluding the first weeks for measles and SARS epidemics, since EpiEstim with the weekly sliding window does not provide estimates for the first week. Y-axis is on a logarithmic scale.

### A.3.2 Short epidemics

Figures A.3.3 and A.3.4 display the KL divergence for short epidemics aggregated over per coordinate excluding the first weeks and months respectively.

## A.4 Experimental results on accuracy under misspecification of serial interval distributions

### A.4.1 SI misspecification for long epidemics

Figures A.4.1 and A.4.2 display KL divergence (excluding first weeks and months respectively) for all 8 methods with mild misspecification (shaped and scaled **measles** SI parameters) and major misspecification

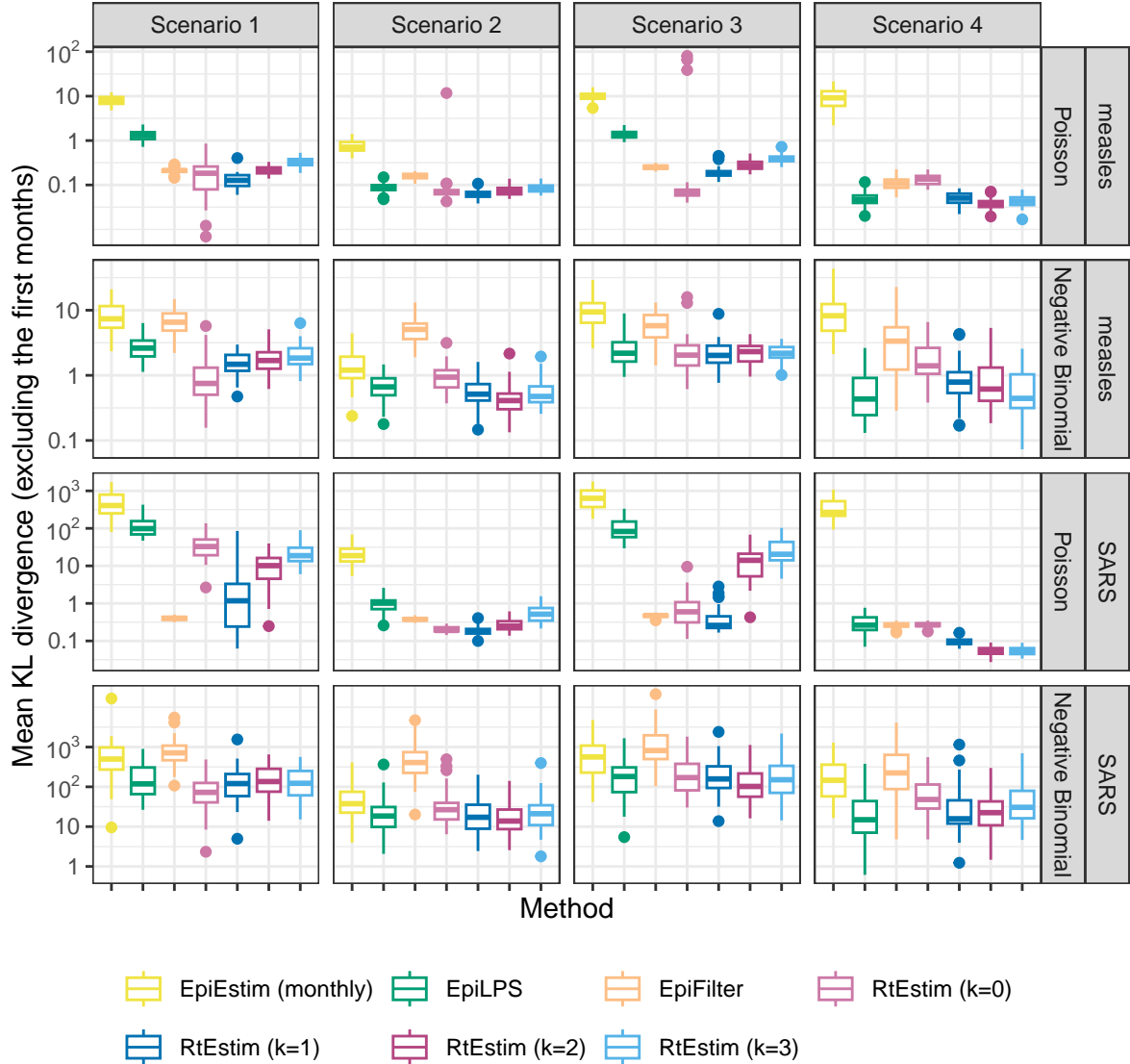


Figure A.3.2: Mean KL divergence excluding the first months for measles and SARS epidemics, since EpiEstim with the monthly sliding window does not provide estimates for the first month. Y-axis is on a logarithmic scale.

(SARS SI parameters) for long `measles` epidemics across all settings.

#### A.4.2 SI misspecification for short epidemics

Figures A.4.3 and A.4.4 display KL divergence (excluding first weeks and months respectively) for all 9 methods with minor misspecification (shaped and scaled `flu` SI parameters) and major misspecification (measles parameters) for short `flu` epidemics across all settings.

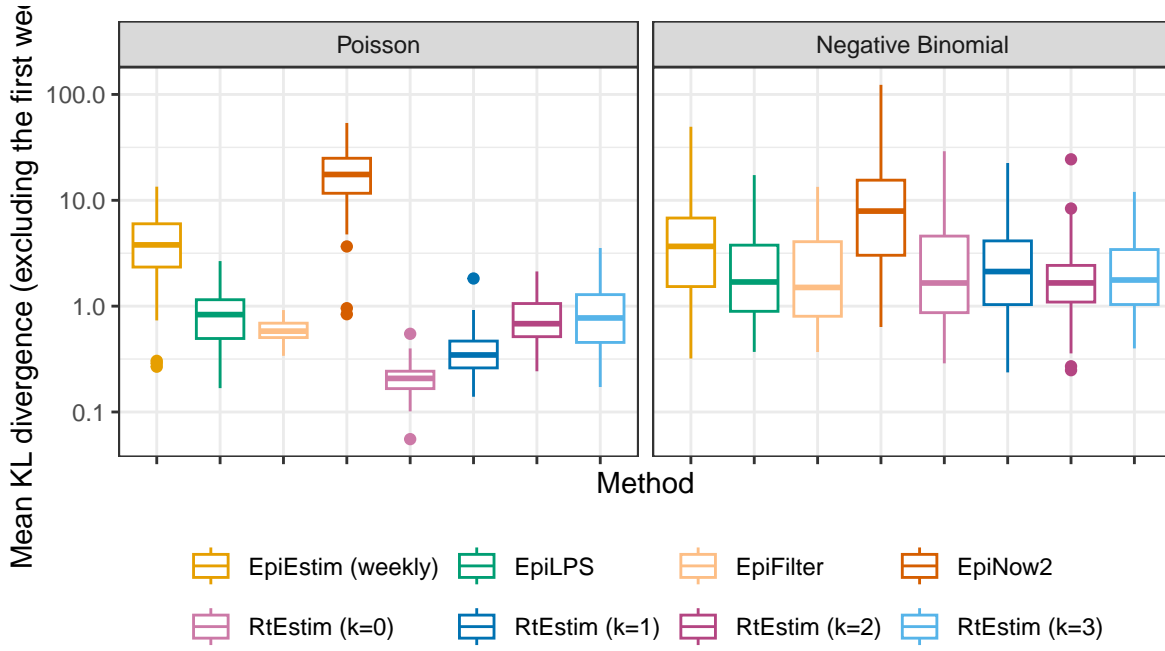


Figure A.3.3: Mean KL divergence excluding the first weeks for flu epidemics, since EpiEstim with the weekly sliding window does not provide estimates for the first week. Y-axis is on a logarithmic scale.

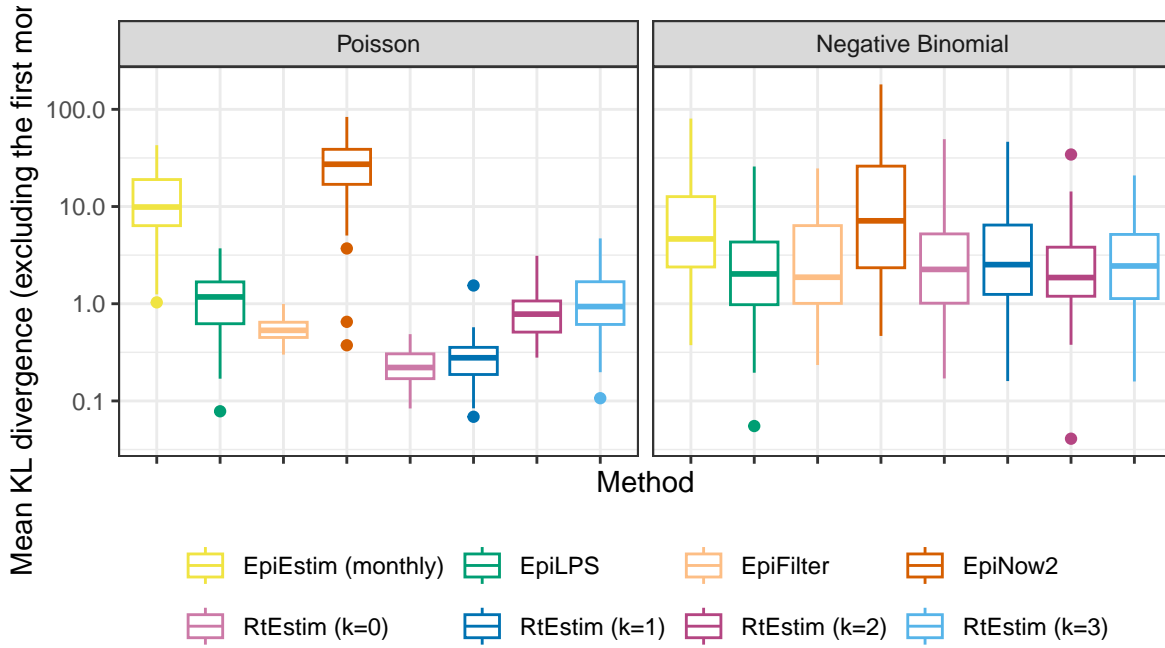


Figure A.3.4: Mean KL divergence excluding the first months for flu epidemics, since EpiEstim with the monthly sliding window does not provide estimates for the first month. Y-axis is on a logarithmic scale.

## A.5 Time comparisons of all methods

Figures A.5.1 show the time comparisons across all methods for long (measles and SARS) epidemics. **EpiEstim** with both weekly and monthly sliding windows are very fast and converge in less than 0.1 seconds. Piecewise

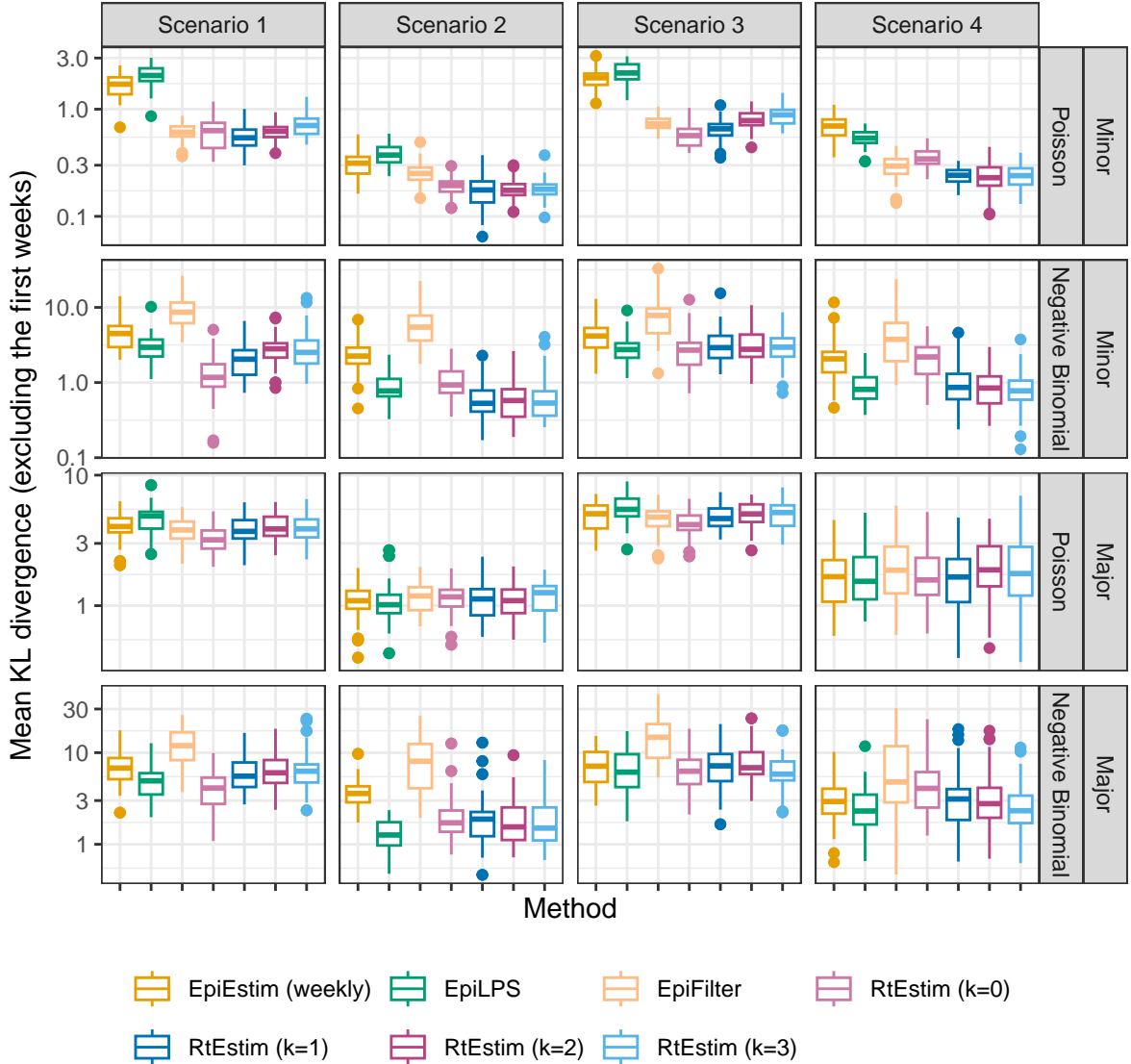


Figure A.4.1: Mean KL divergence excluding the first weeks for measles epidemics with SI misspecification, since EpiEstim with the weekly sliding window does not provide estimates for the first week. Y-axis is on a logarithmic scale.

constant **RtEstim** (with  $k=0$ ) estimates can be generated within 0.1 seconds as well. **EpiLPS** is slightly slower, but still very fast and within 1 second for all experiments. Piecewise linear and cubic **RtEstim** (with  $k = 1$  and  $k = 3$  respectively) are slower, but mostly within 10 seconds.

It is remarkable that our **RtEstim** computes 50 lambda values with 10-fold CV for each experiment, which results in 550 times of modelling per experiment (including modelling for all folds). The running times are no more than 10 seconds for most of the experiments, which means the running time for each time of modelling is very fast, and on average can be less than 0.02 seconds. The other two methods only run once for a fixed set of hyperparameters for each experiment.

We visualize the running times of each case in separate panels in Figures A.5.2 and A.5.3 for measles and SARS epidemics respectively. Similar results as in Figure A.5.1 are found in each setting.

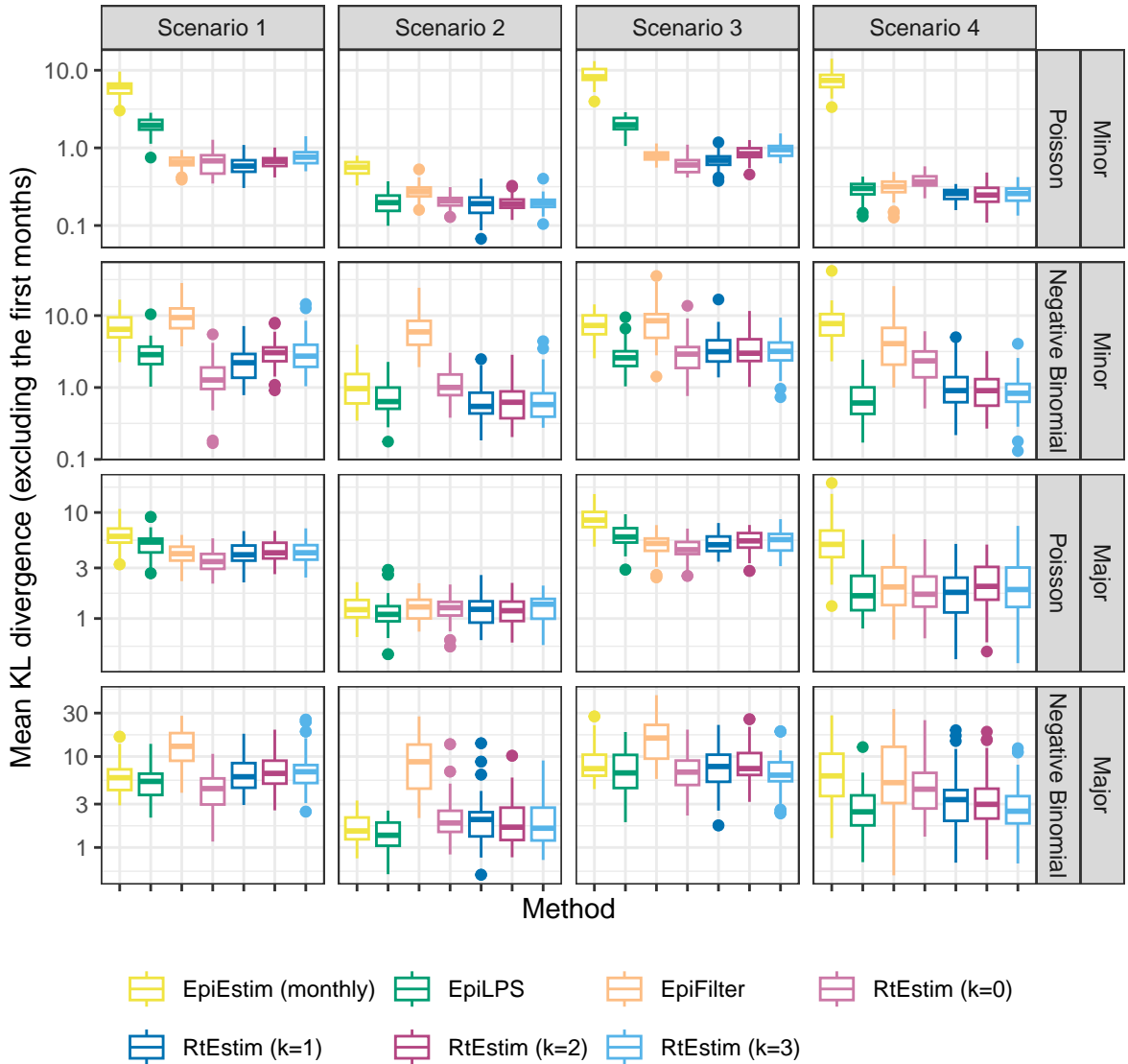


Figure A.4.2: Mean KL divergence excluding the first months for measles epidemics with SI misspecification, since EpiEstim with the monthly sliding window does not provide estimates for the first month. Y-axis is on a logarithmic scale.

Figure A.5.4 displays the running times of all methods for short (flu) epidemics. Figure A.5.5 displays the running times for each setting separately, and finds similar results as in the overall running time comparison.

## A.6 Confidence interval coverage

### A.6.1 Display estimates and confidence intervals for sample epidemics

Let's take a clearer view of the estimated  $\mathcal{R}_t$  with 95% confidence intervals for the sample long epidemics by all methods in Fig 5 and Fig 6 in Figures A.6.1 and A.6.4 respectively. The full view of other example epidemics are visualized in Figures A.6.2 and A.6.3 as follows.

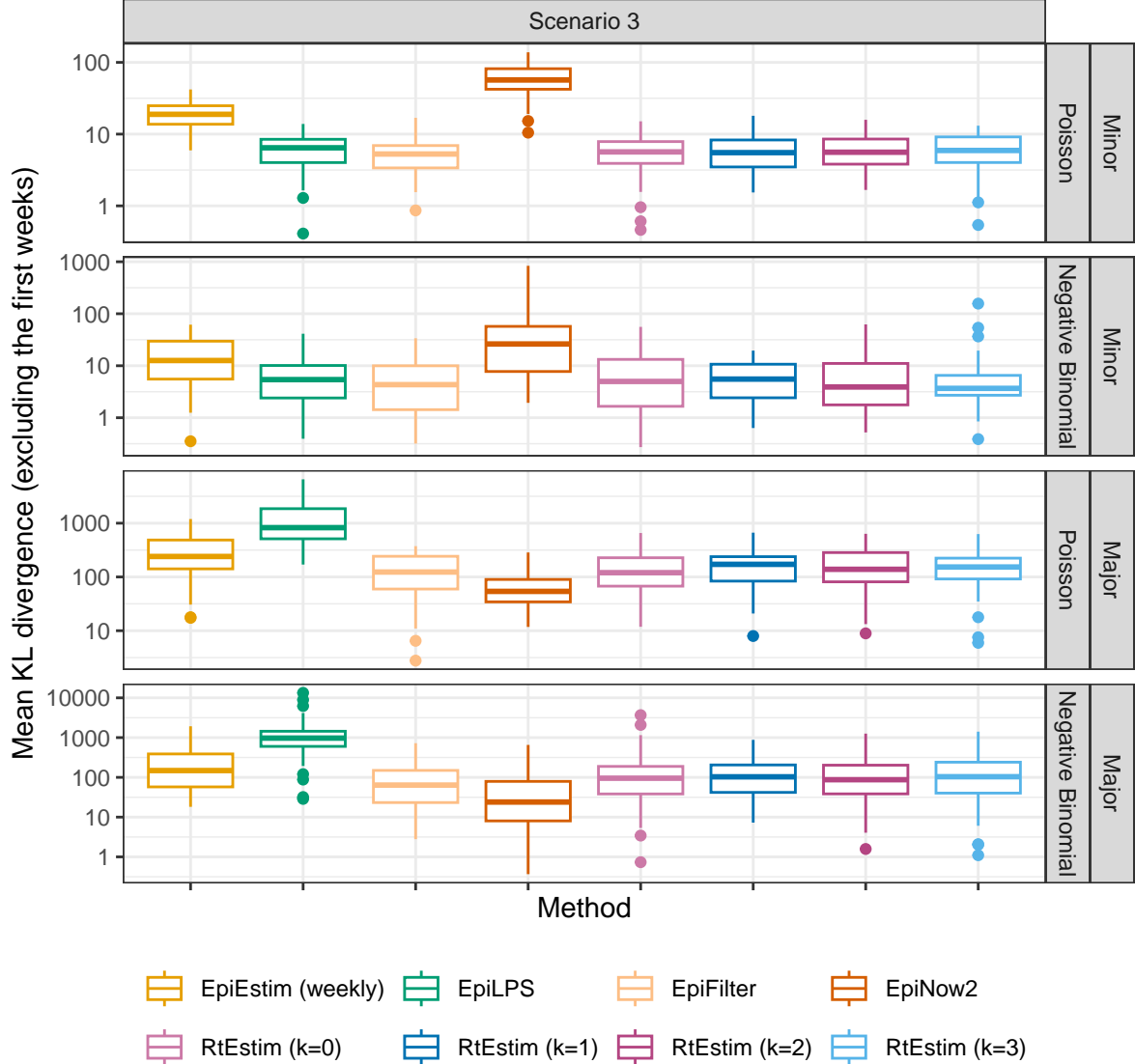


Figure A.4.3: Mean KL divergence excluding the first weeks for flu epidemics with SI misspecification, since EpiEstim with the weekly sliding window does not provide estimates for the first week. Y-axis is on a logarithmic scale.

## A.6.2 Experimental settings on coverage level comparison of confidence intervals

We focus on a specific  $\mathcal{R}_t$  scenario, the piecewise linear case, and only long epidemics to compare the coverage of 95% confidence intervals across all 8 methods. We use the true serial interval distributions in modelling. Table 2 summarizes the experimental settings.

## A.6.3 Experimental results on interval coverage comparison

Figures A.6.5 and A.6.6 displays the percentages of coverage of 95% CI per coordinate over 50 random samples for measles and SARS epidemics respectively.

Figures A.6.7 and A.6.8 displays the percentages of coverage of 95% CI across all timepoints averaged over 50 random measles and SARS epidemics respectively.

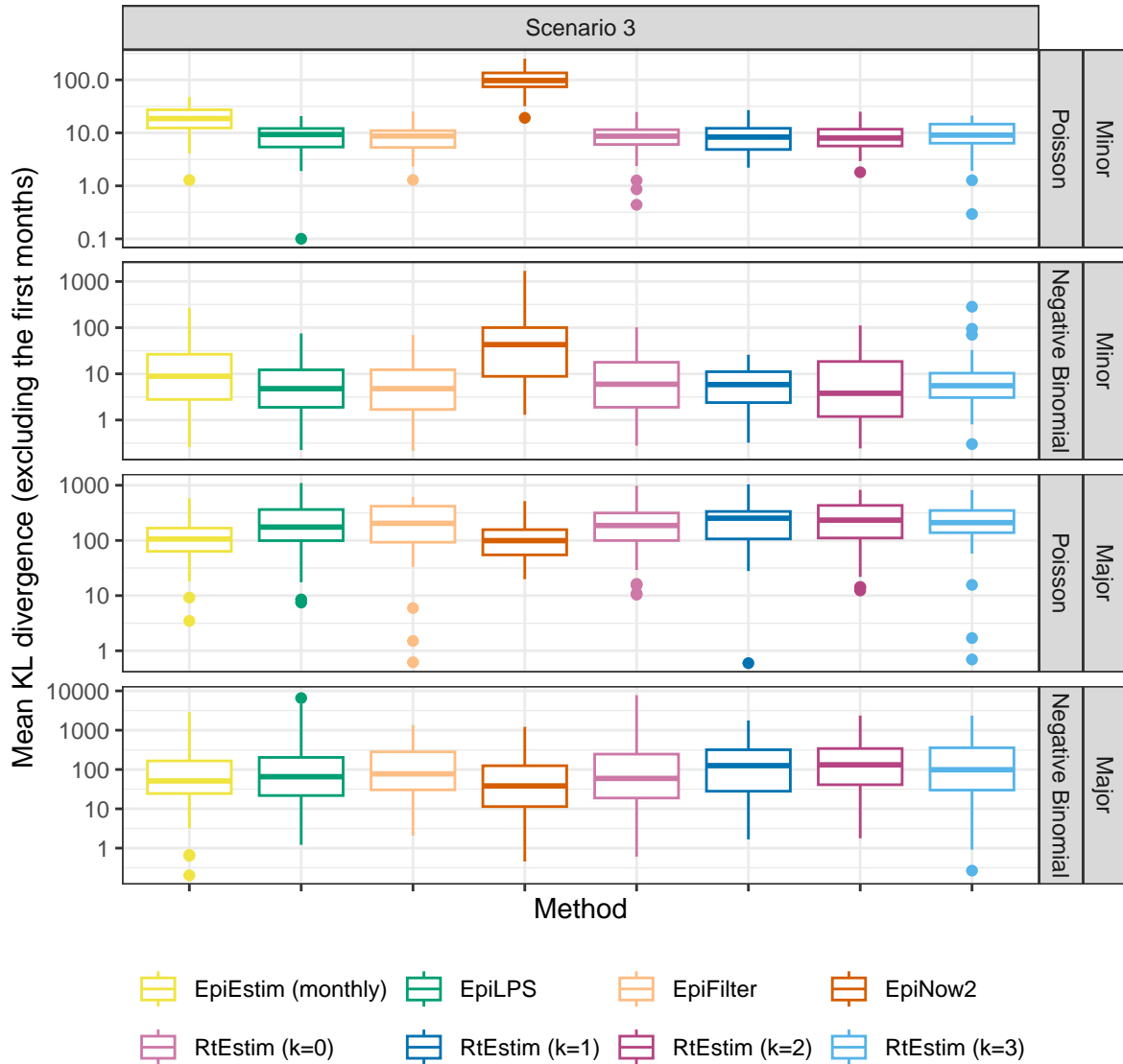


Figure A.4.4: Mean KL divergence excluding the first months for flu epidemics with SI misspecification, since EpiEstim with the monthly sliding window does not provide estimates for the first month. Y-axis is on a logarithmic scale.

We output a vector of the CI coverage for each timepoint per experiment, the percentage of coverage of all timepoints, and the interval score

$$score_\alpha(\mathcal{R}, u, l) = \frac{1}{n} \sum_{t=1}^n (u_t - l_t) + \frac{2}{\alpha} (l_t - \mathcal{R}_t) \mathbf{1}_{(\mathcal{R}_t < l_t)} + \frac{2}{\alpha} (\mathcal{R}_t - u_t) \mathbf{1}_{(\mathcal{R}_t > u_t)}$$

, where  $\alpha = 0.05$  is the significance level,  $l, u$  are the lower and upper bounds,  $\mathcal{R}_t$  is the true effective reproduction number, and  $\mathbf{1}_X$  is the indicator function of the condition  $X$ . (Bracher et al. 2021). Figures A.6.9 and A.6.10 displays the interval scores of 95% CI averaged over 50 random measles and SARS epidemics respectively.

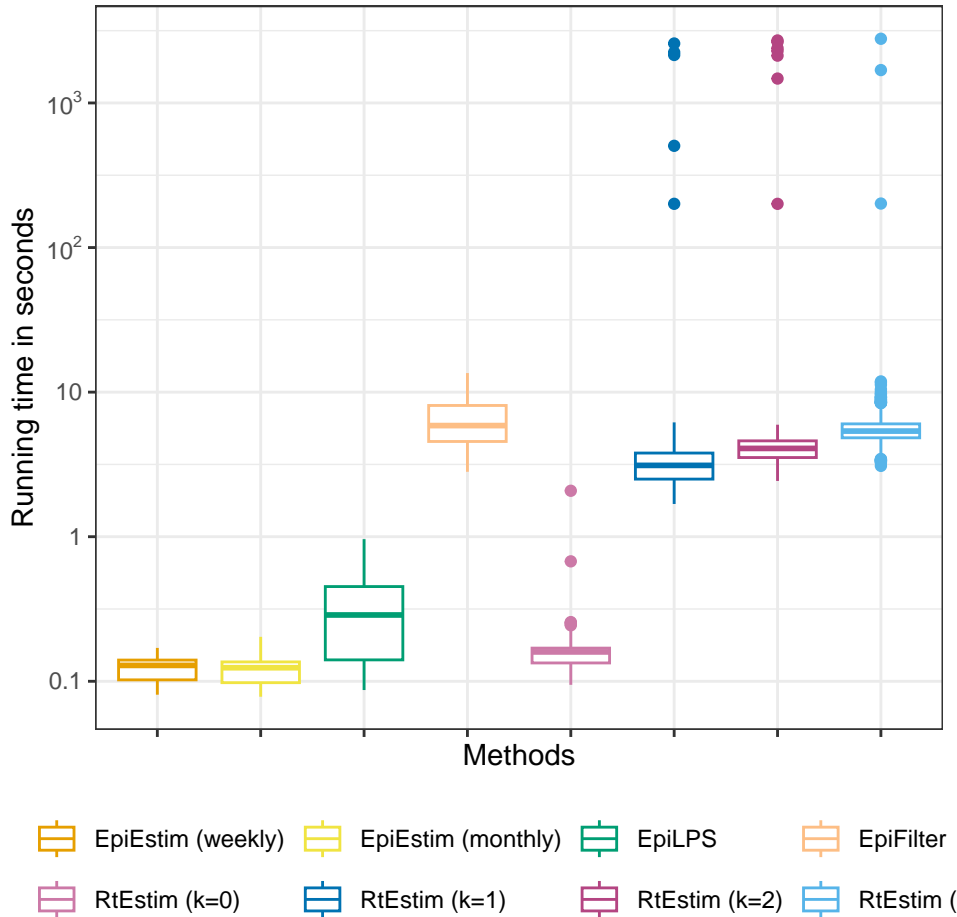


Figure A.5.1: Time comparisons of all methods for long (measles and SARS) epidemics across all cases. Y-axis is on a logarithmic scale.

## A.7 Data examples and alternative visualizations of Figs 5 and 6

### A.7.1 More visualization of example epidemics

We generate measles and SARS epidemics using Poisson and negative Binomial incidence distributions for each experimental settings. The condensed display of estimates for measles with Poisson incidence and SARS with negative Binomial incidence are provided in Fig 5 and Fig 6. A full visualization of each case is provided in Section A.6.1. The condensed visualization of other cases is provided below in Figures A.7.1 and A.7.2.

Table 2: Summary of experimental setting on coverage of confidence intervals

Length	SI	Rt scenario	Incidence	SI for modelling	Method
300	measles		3	Poisson, NB	measles
300	SARS		3	Poisson, NB	SARS

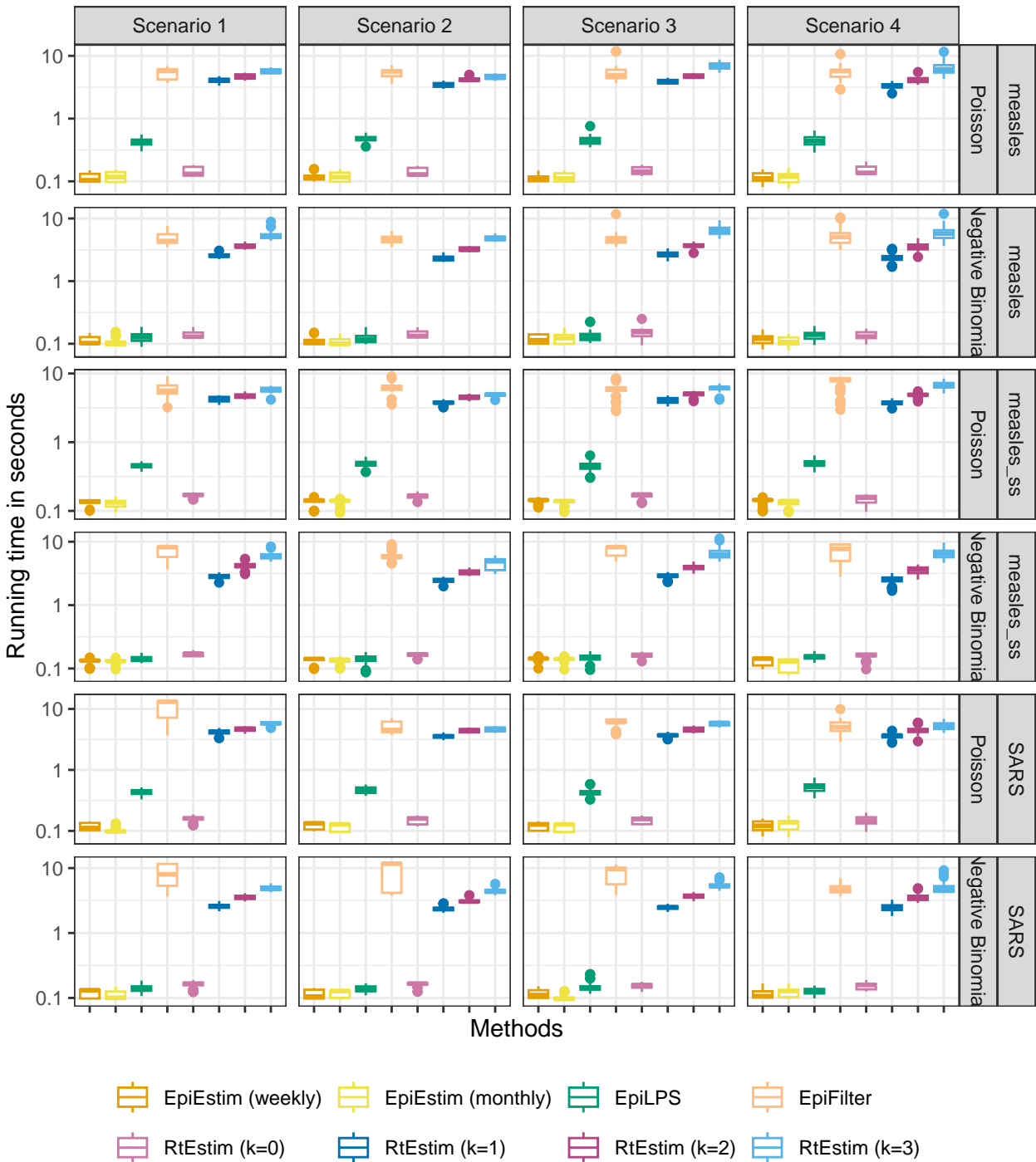


Figure A.5.2: Time comparisons of all methods for measles epidemics with each choice of SI parameter for modelling per incidence distribution per Rt scenario (excluding outliers for better illustration). Y-axis is on a logarithmic scale.

### A.7.2 Alternative view of difference between fitted and true Rt estimates

Here, we also provide an alternative view of Fig 5 & Fig 6 by plotting  $\mathcal{R}_t - \hat{\mathcal{R}}_t$  per coordinate  $t$  in A.7.3 and A.7.4 respectively. Figures A.7.5 and A.7.6 provide the alternative view of A.7.1 and A.7.2 respectively.

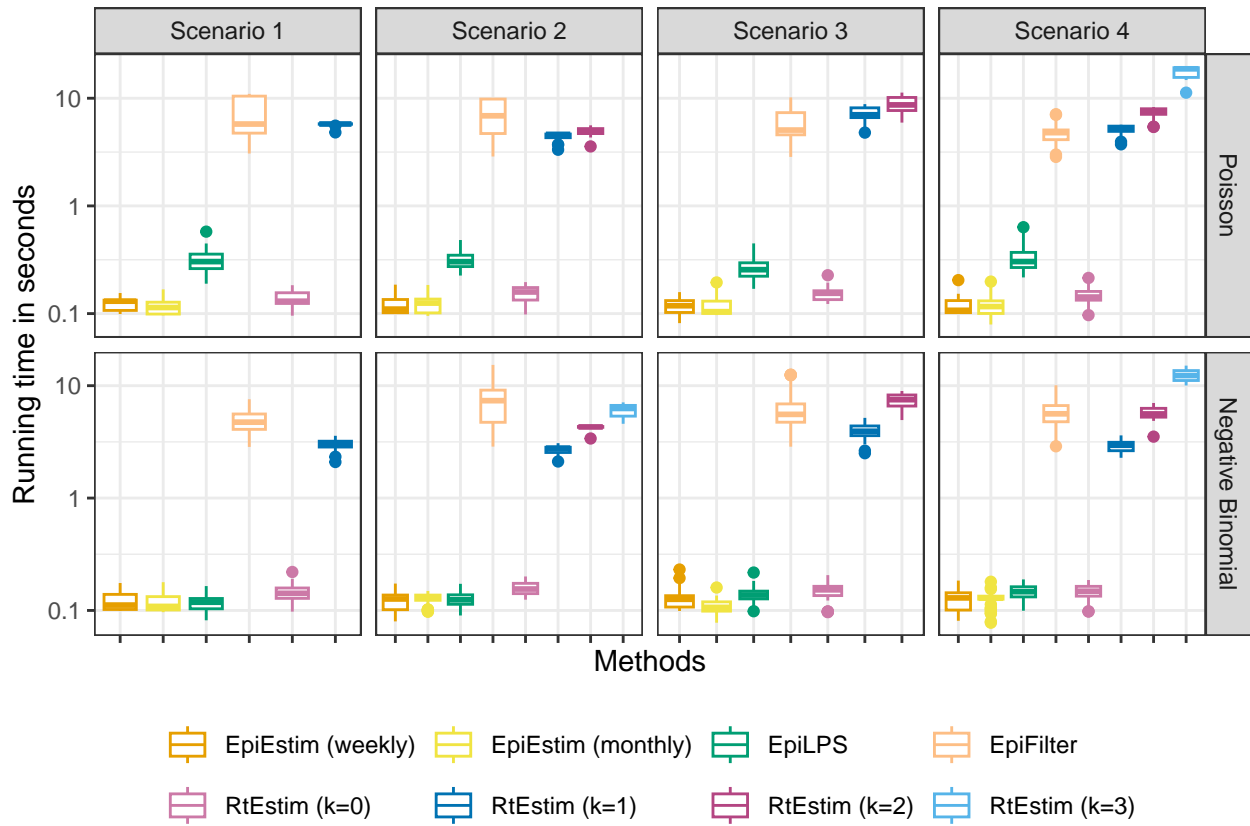


Figure A.5.3: Time comparisons of all methods for SARS epidemics with each choice of SI parameter for modelling per incidence distribution per Rt scenario (excluding outliers for better illustration). Y-axis is on a logarithmic scale.

## A.8 Application of RtEstim and all competitors on real epidemics

We apply all methods on Covid19 incidence in BC, and the estimated are displayed in ???. An alternative display which plot all estimated curves in one panel for an easier comparison is provided in ???.

We also apply all methods on Flu in 1918 as well. The results are visualized in Figures A.8.3 and A.8.4.

Boëlle, Pierre-Yves, Severine Ansart, Anne Cori, and Alain-Jacques Valleron. 2011. “Transmission Parameters of the a/H1N1 (2009) Influenza Virus Pandemic: A Review.” *Influenza and Other Respiratory Viruses* 5 (5): 306–16.

Bracher, Johannes, Evan L. Ray, Tilmann Gneiting, and Nicholas G. Reich. 2021. “Evaluating Epidemic Forecasts in an Interval Format.” Edited by Virginia E. Pitzer. *PLoS Computational Biology* 17 (2): e1008618. <https://doi.org/10.1371/journal.pcbi.1008618>.

Cori, Anne, Neil M Ferguson, Christophe Fraser, and Simon Cauchemez. 2013. “A New Framework and Software to Estimate Time-Varying Reproduction Numbers During Epidemics.” *American Journal of Epidemiology* 178 (9): 1505–12.

Ferguson, Neil M, Derek AT Cummings, Simon Cauchemez, Christophe Fraser, Steven Riley, Aronrag Meeyai, Sopon Iamsirithaworn, and Donald S Burke. 2005. “Strategies for Containing an Emerging Influenza Pandemic in Southeast Asia.” *Nature* 437 (7056): 209–14.

Groendyke, Chris, David Welch, and David R Hunter. 2011. “Bayesian Inference for Contact Networks Given

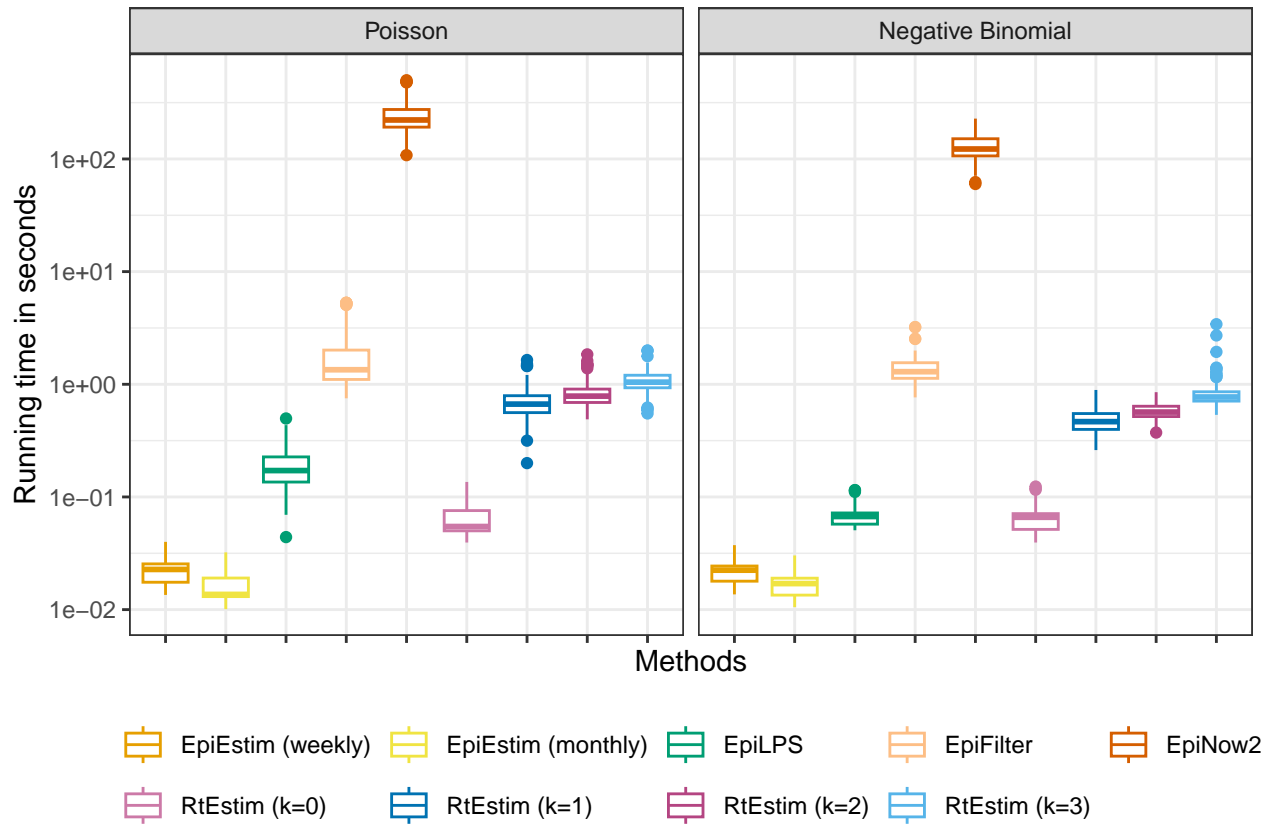


Figure A.5.4: Time comparisons of methods for short (flu) epidemics across all cases. Y-axis is on a logarithmic scale.

Epidemic Data.” *Scandinavian Journal of Statistics* 38 (3): 600–616.

Lipsitch, Marc, Ted Cohen, Ben Cooper, James M Robins, Stefan Ma, Lyn James, Gowri Gopalakrishna, et al. 2003. “Transmission Dynamics and Control of Severe Acute Respiratory Syndrome.” *Science* 300 (5627): 1966–70.

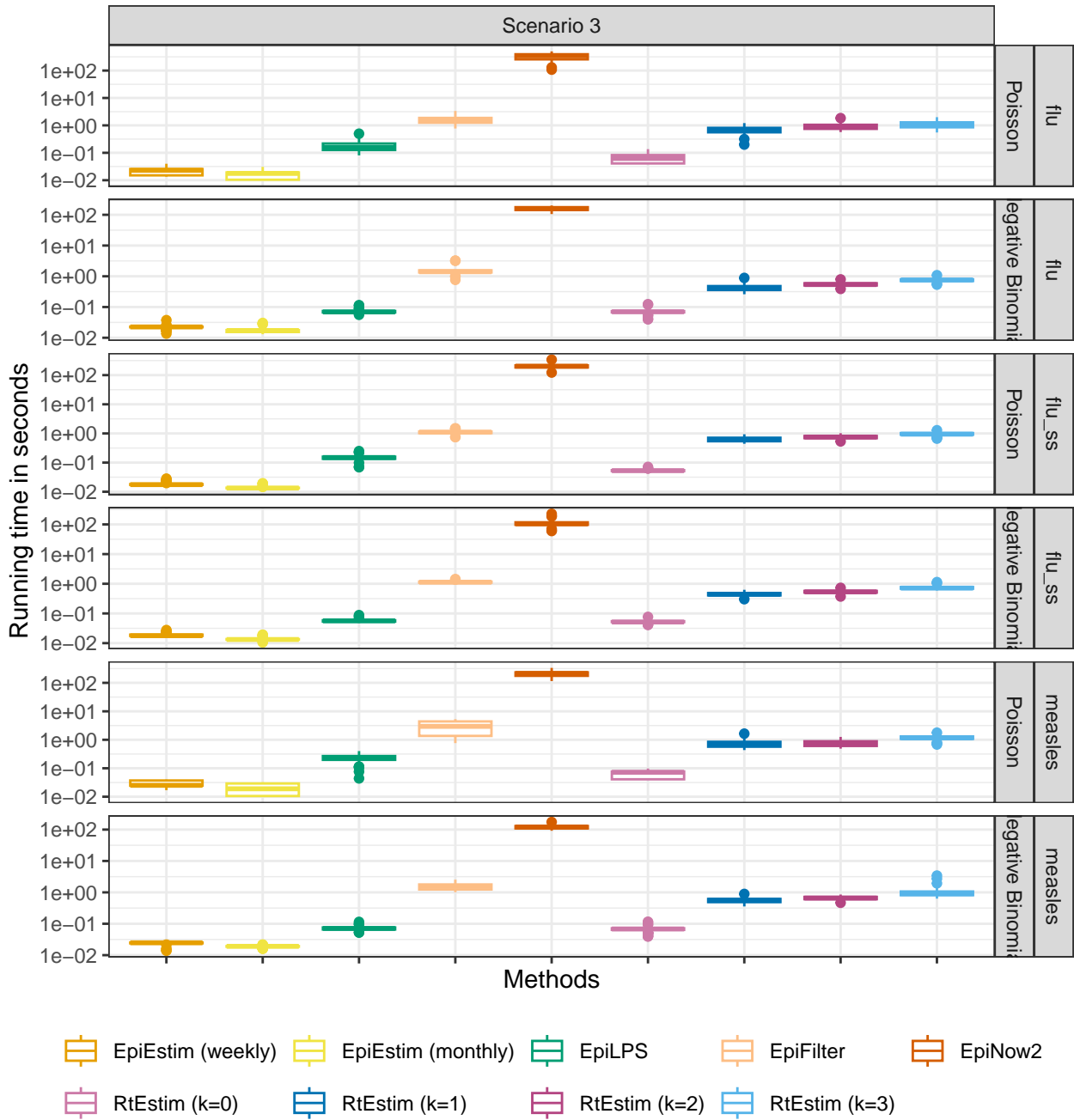


Figure A.5.5: Time comparisons of methods for short (flu) epidemics with different cases in different panels. Y-axis is on a logarithmic scale.

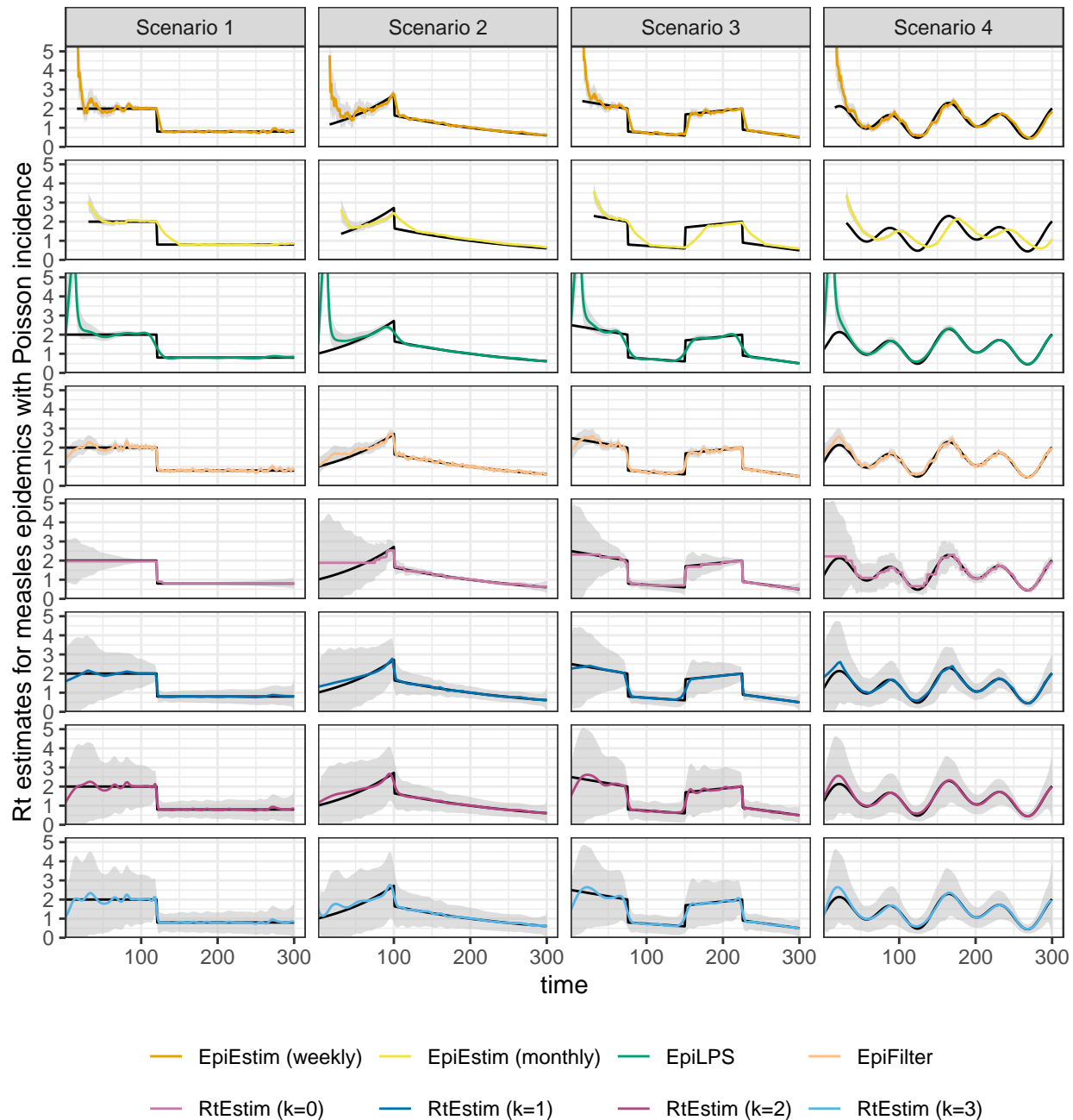


Figure A.6.1: Example measles epidemics with Poisson incidence.

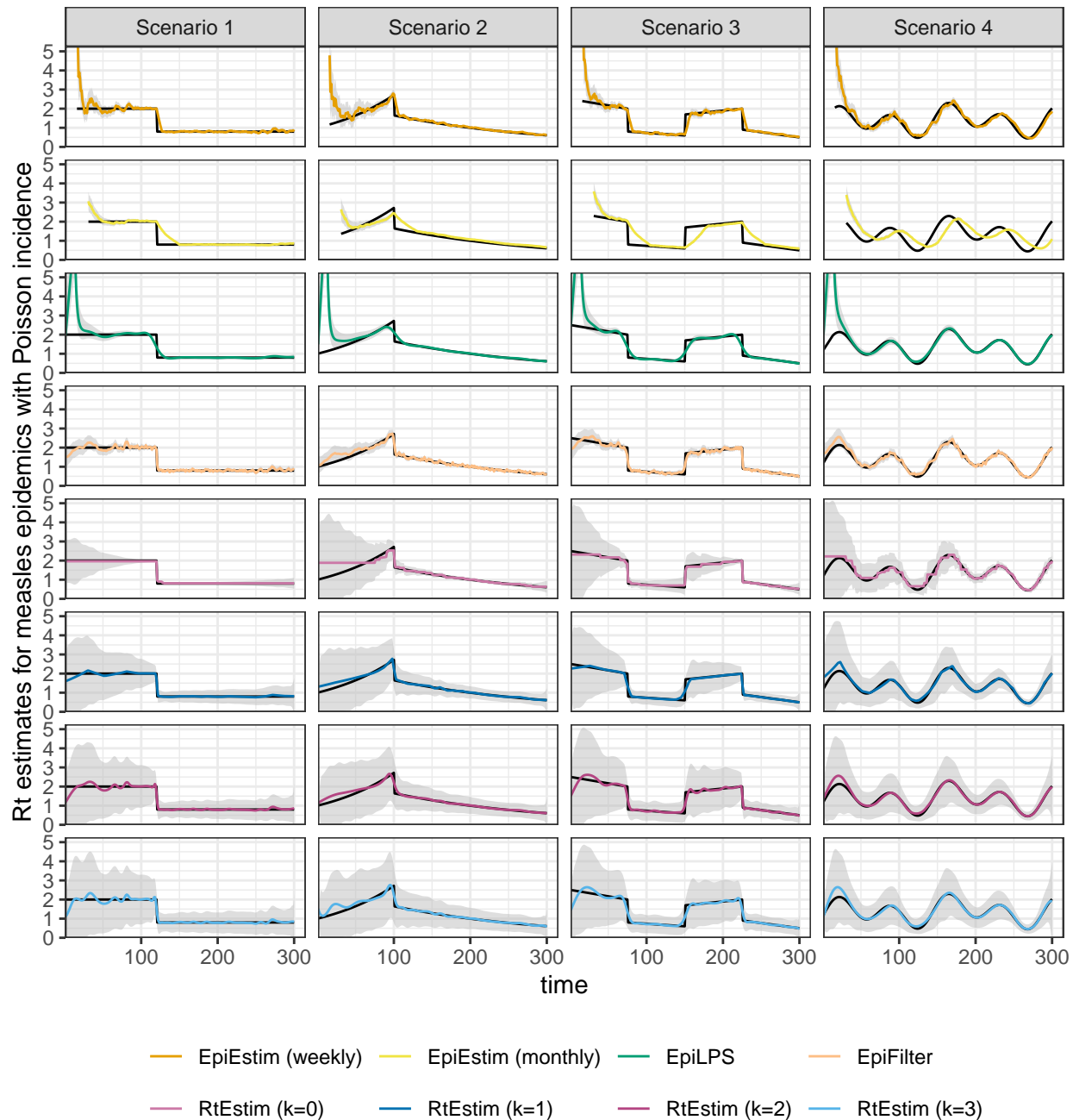


Figure A.6.2: Example measles epidemics with negative Binomial incidence.

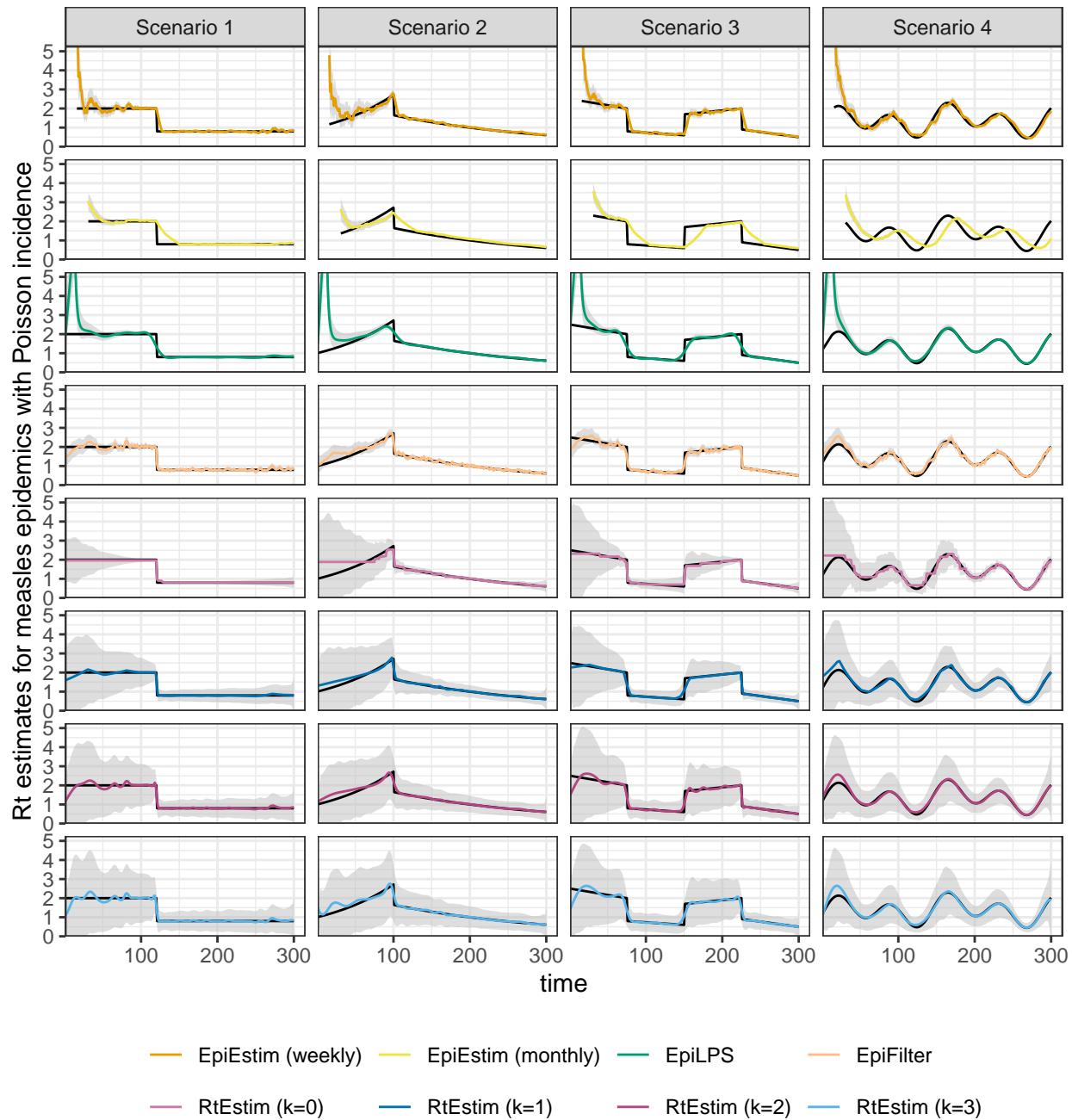


Figure A.6.3: Example SARS epidemics with Poisson incidence.

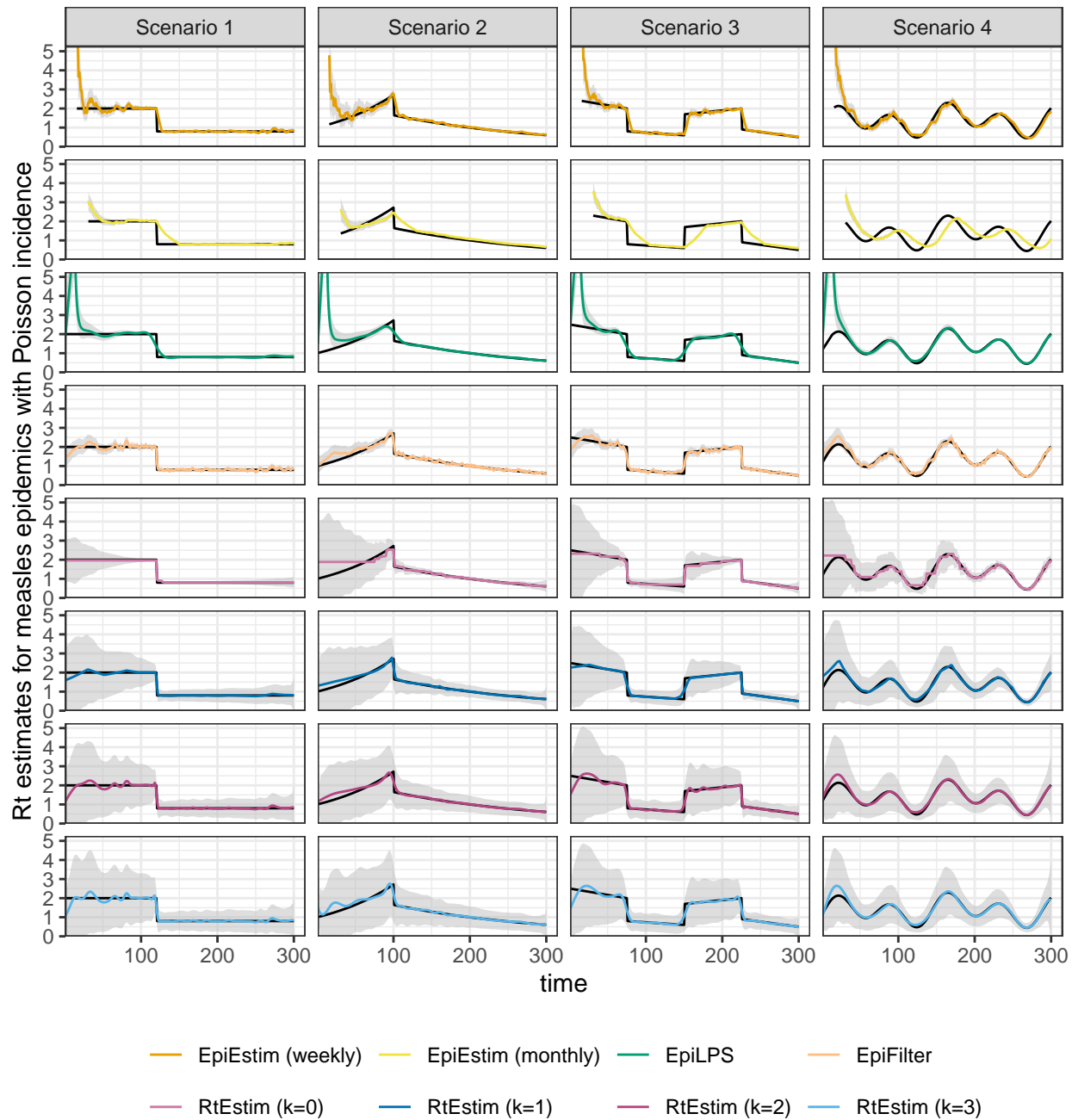


Figure A.6.4: Example SARS epidemics with negative Binomial incidence.

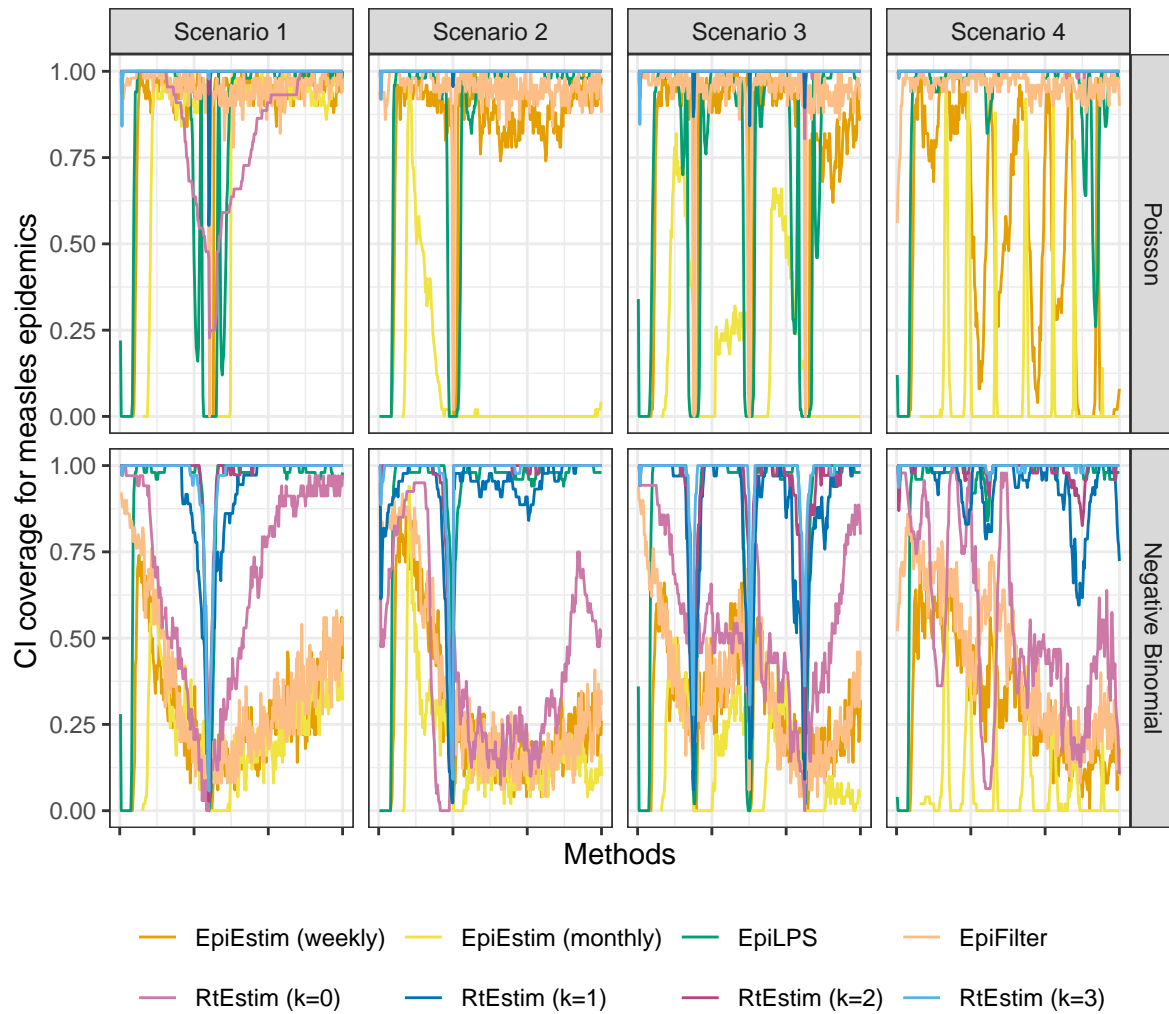


Figure A.6.5: Averaged coverage of CI per coordinate with measles epidemics.

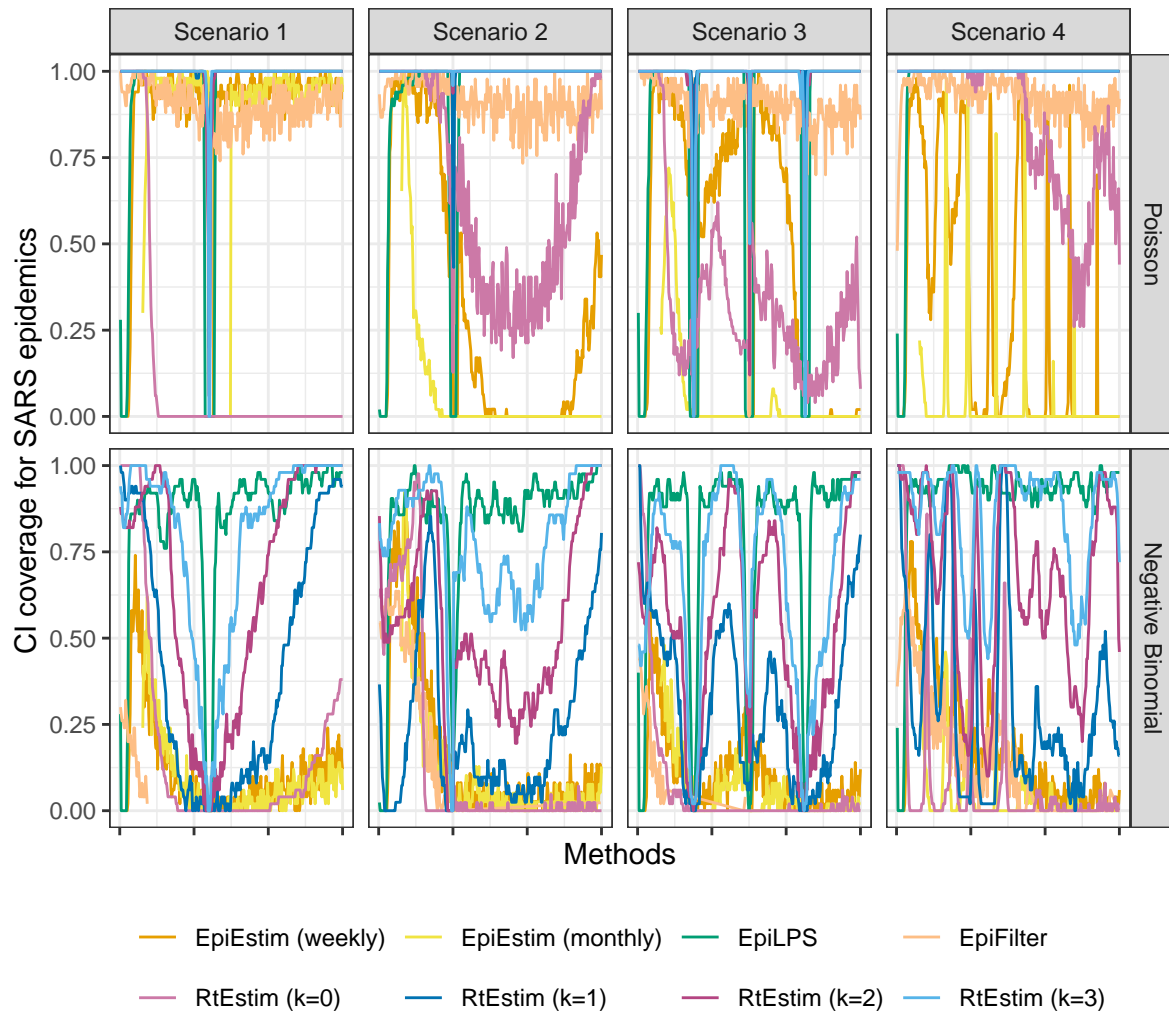


Figure A.6.6: Averaged coverage of CI per coordinate with SARS epidemics.

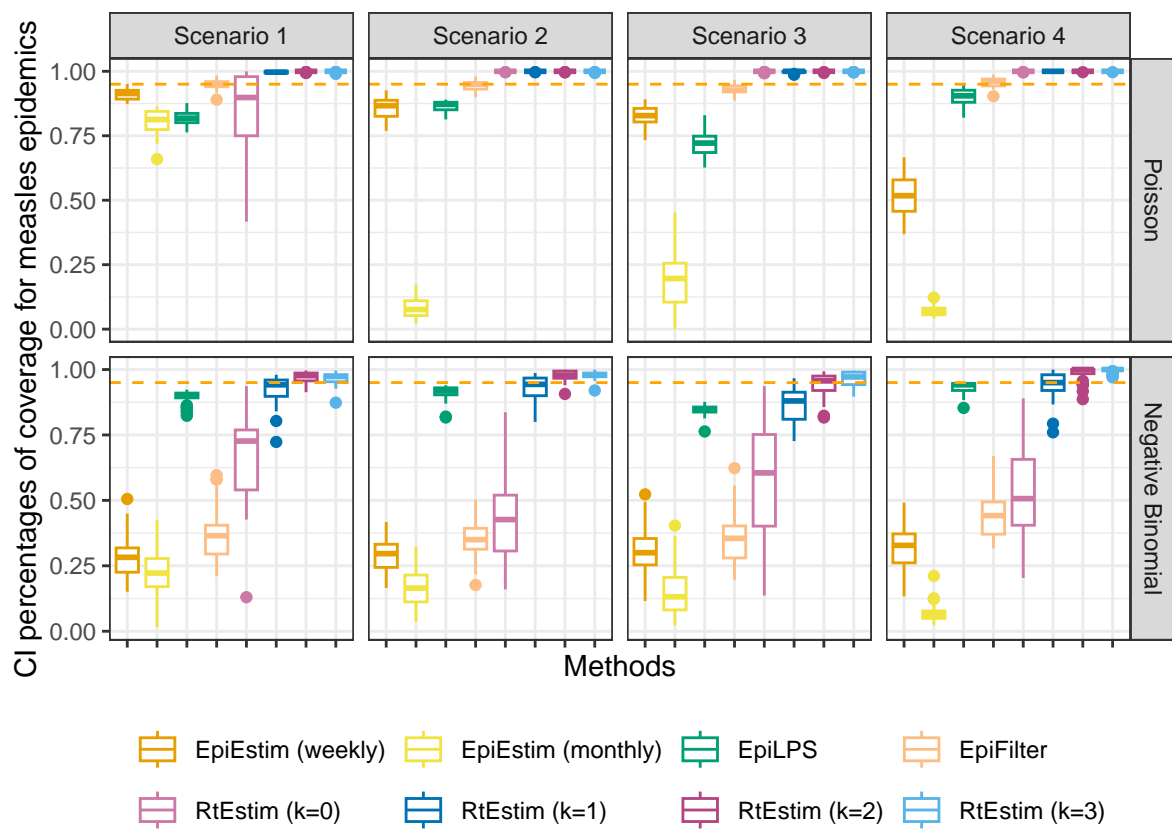


Figure A.6.7: Averaged percentages of CI coverage with measles epidemics.

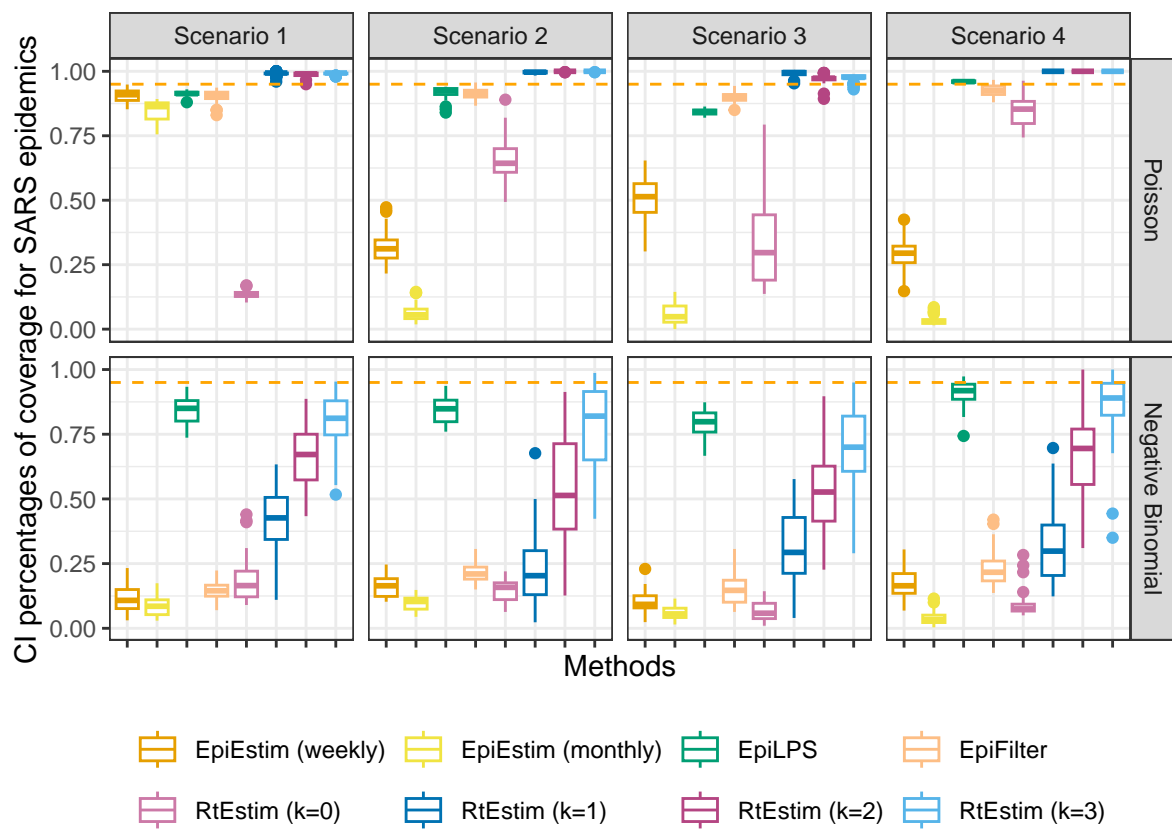


Figure A.6.8: Averaged percentages of CI coverage with SARS epidemics.

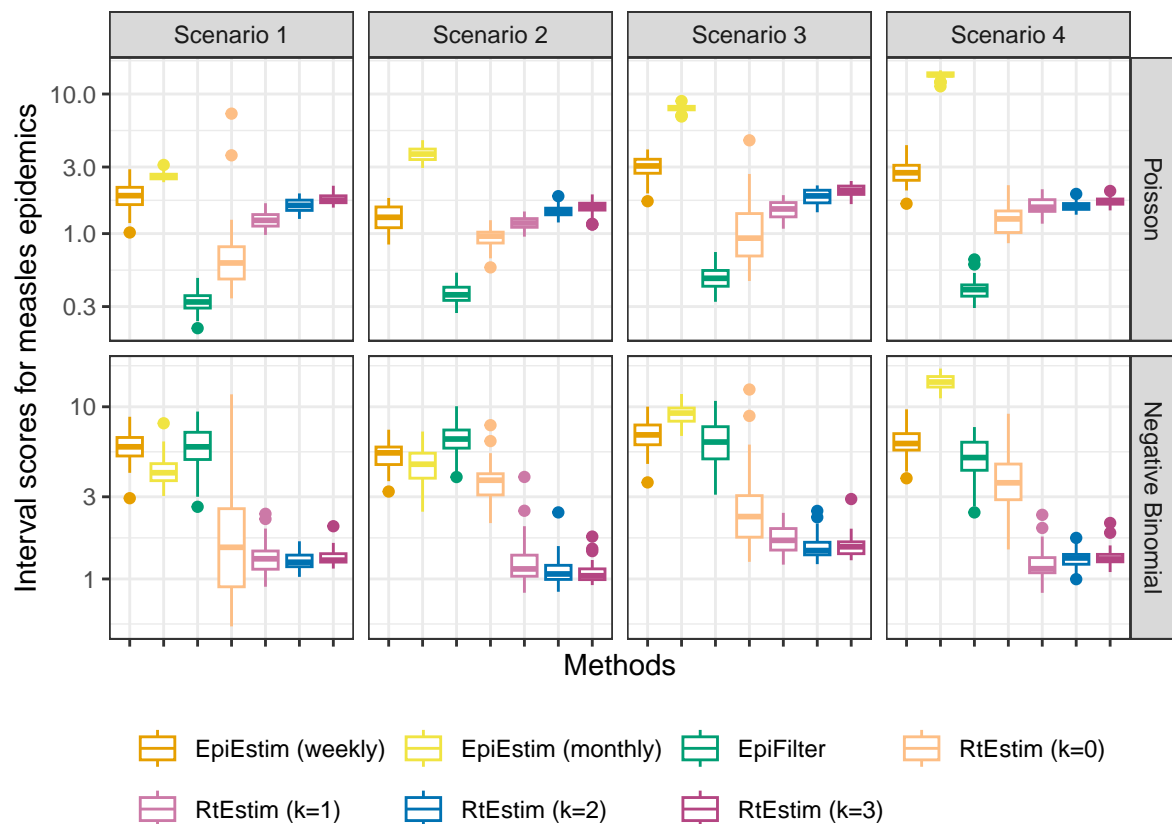


Figure A.6.9: Averaged interval scores with measles epidemics. EpiLPS is excluded, since it's scores are always larger than 100.

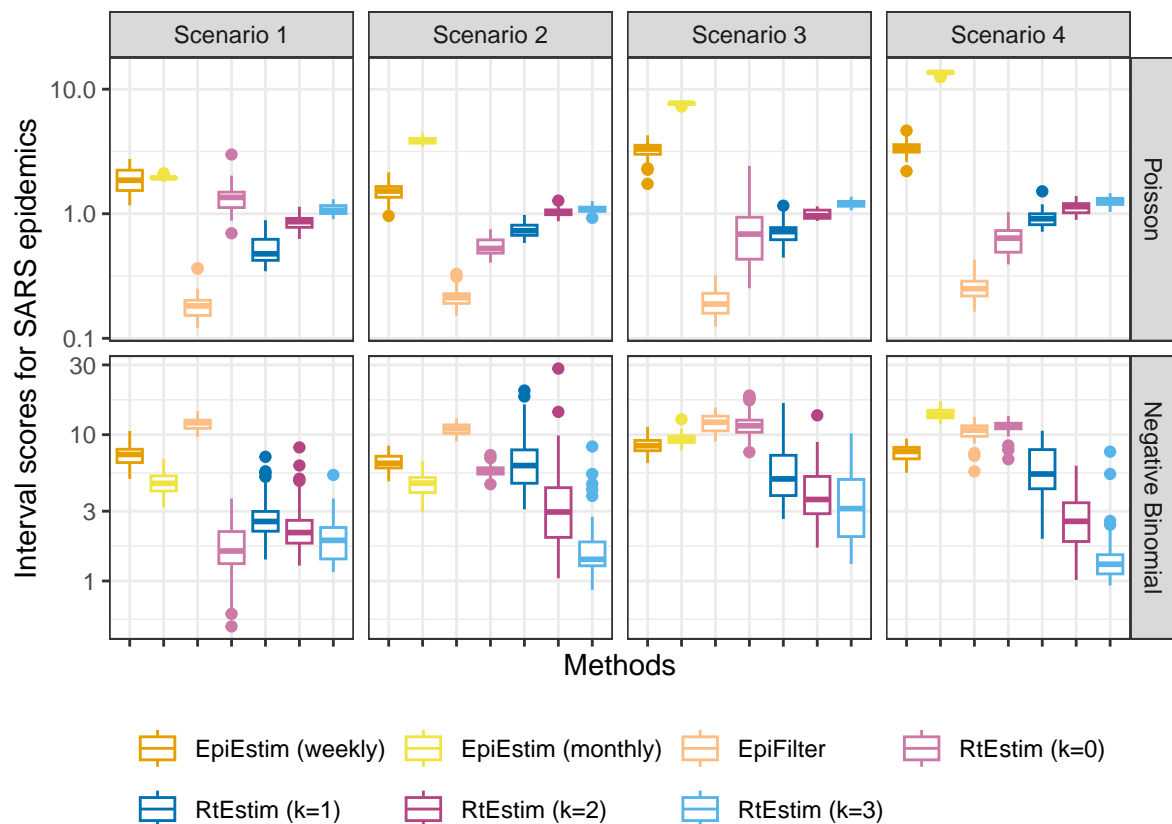


Figure A.6.10: Averaged interval scores with SARS epidemics. EpiLPS is excluded, since it's scores are always larger than 100.

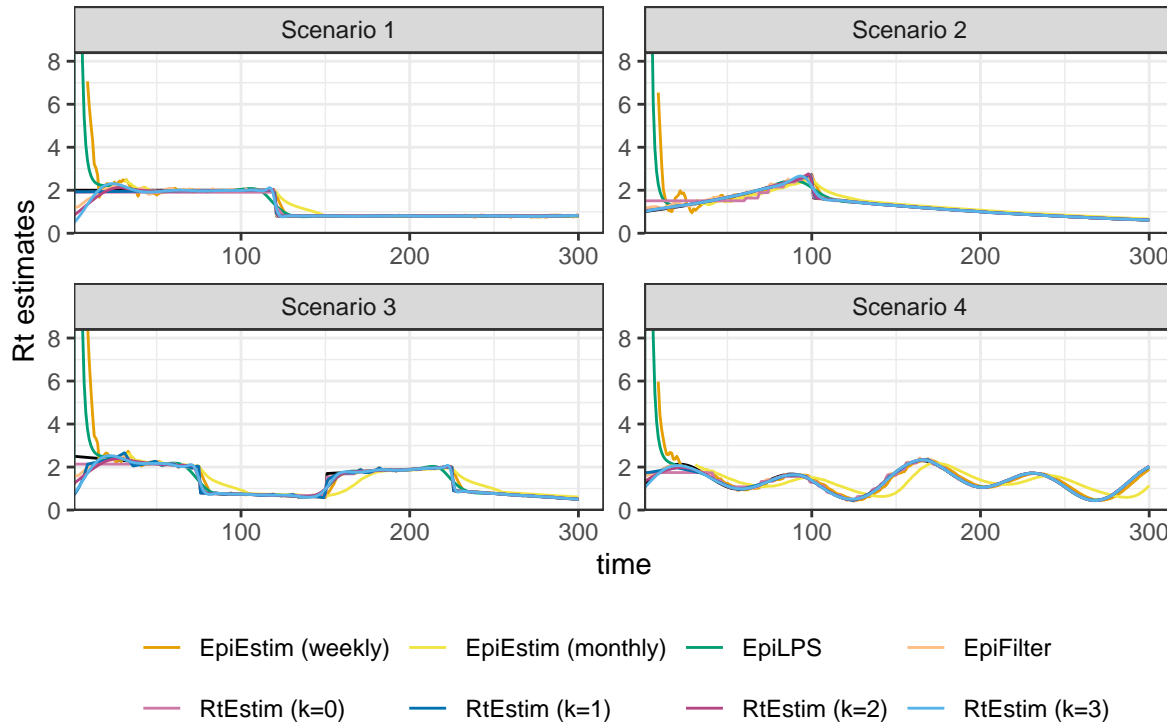


Figure A.7.1: Example of effective reproduction number estimation for SARS epidemics with Poisson observations.

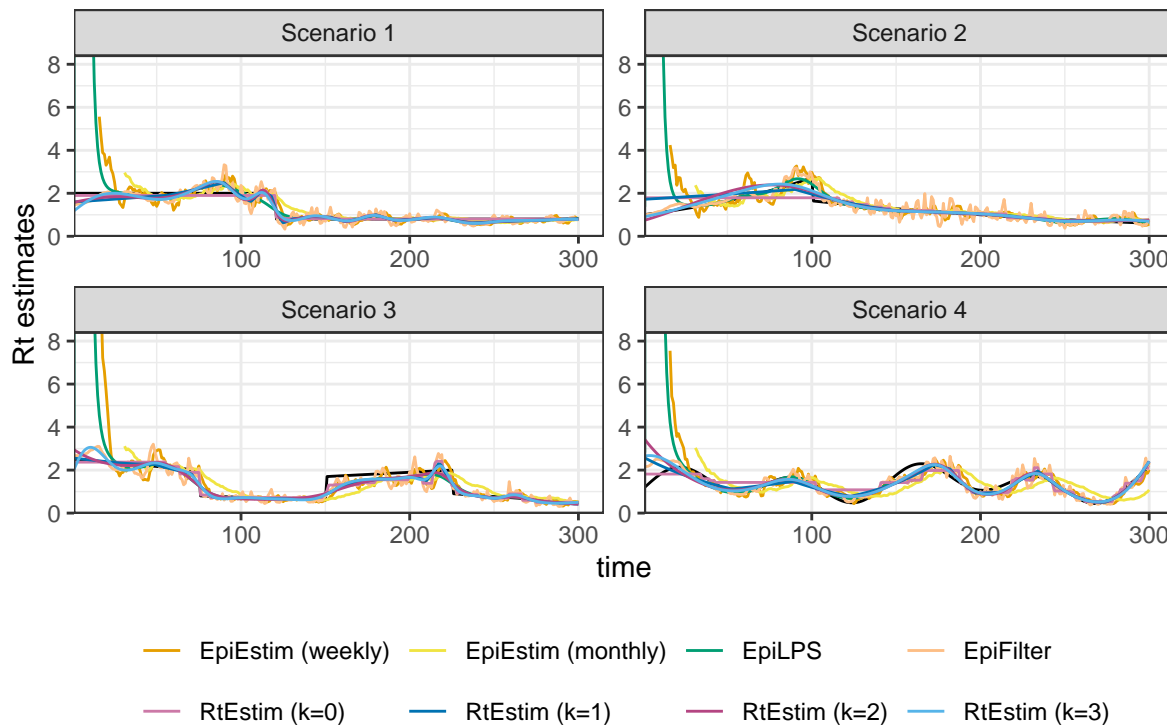


Figure A.7.2: Example of effective reproduction number estimation for measles epidemics with negative Binomial observations.

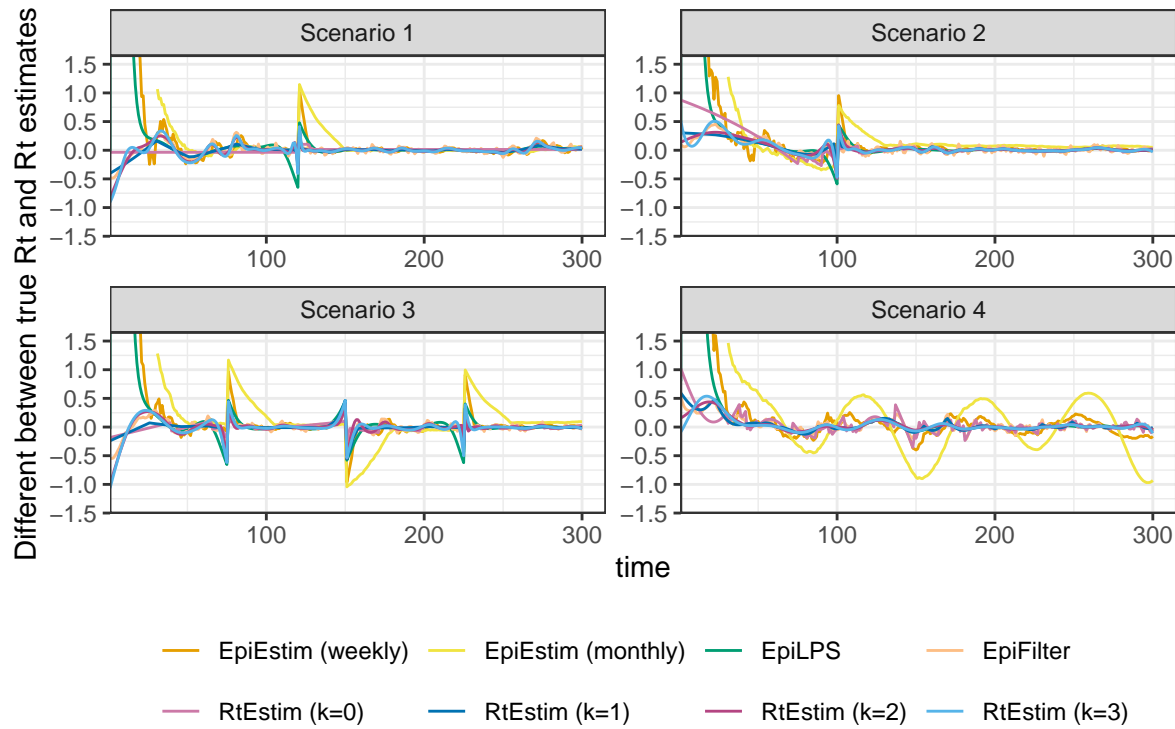


Figure A.7.3: Difference between of the true effective reproduction number and its estimation for measles epidemics with Poisson observations.

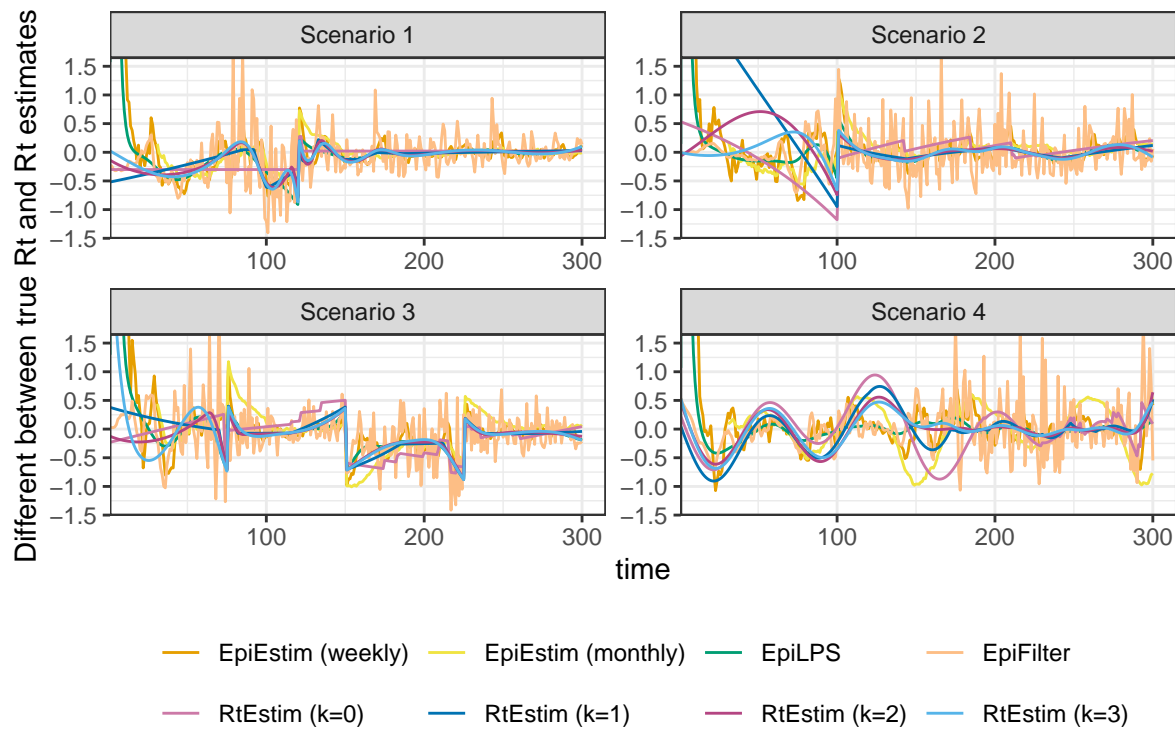


Figure A.7.4: Difference between of the true effective reproduction number and its estimation for SARS epidemics with negative Binomial observations.

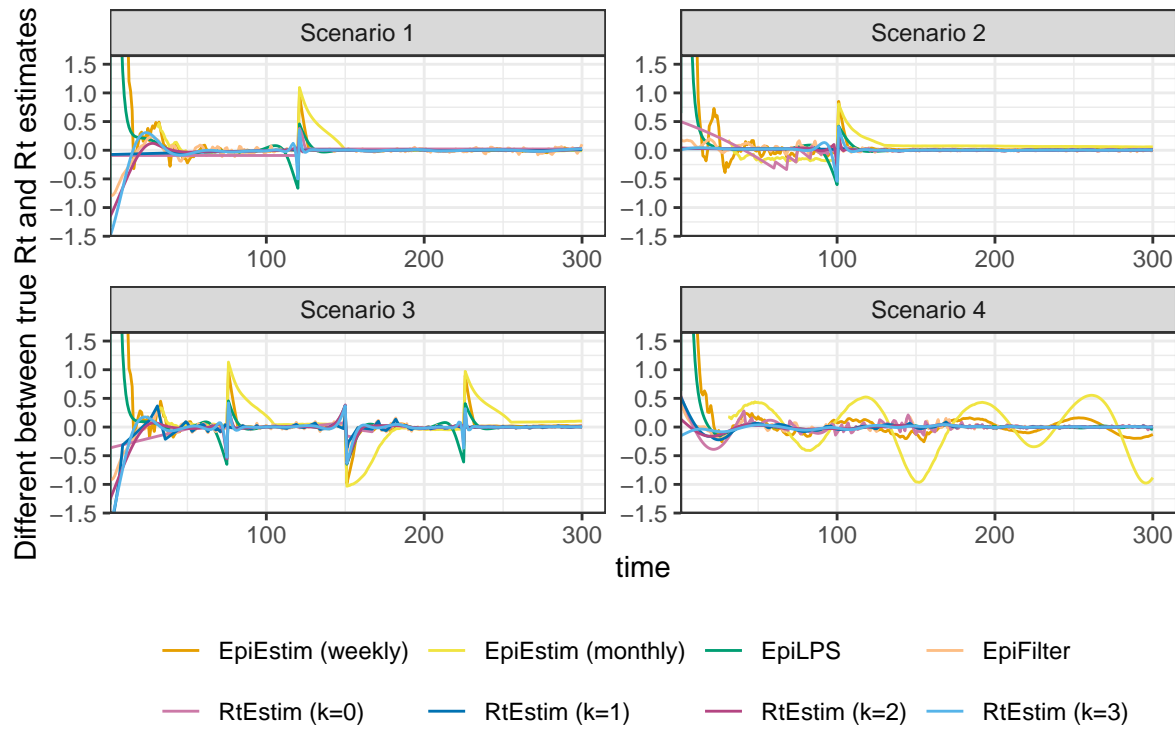


Figure A.7.5: Difference between of the true effective reproduction number and its estimation for SARS epidemics with Poisson observations.

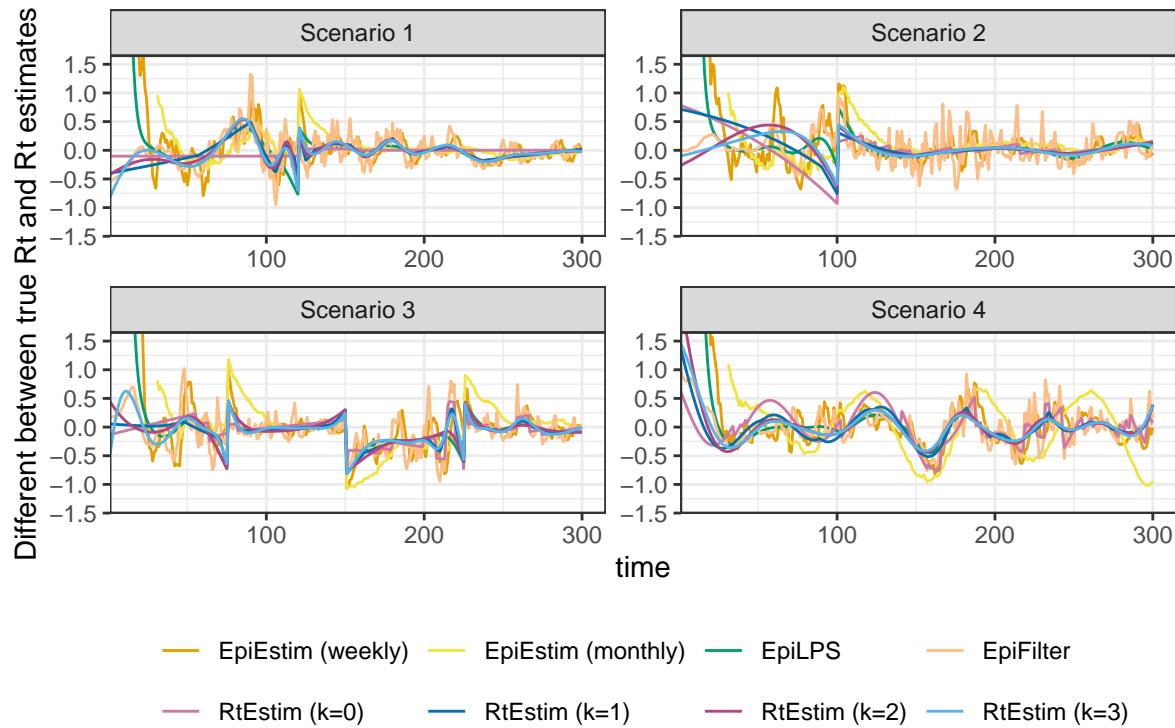


Figure A.7.6: Difference between of the true effective reproduction number and its estimation for measles epidemics with negative Binomial observations.

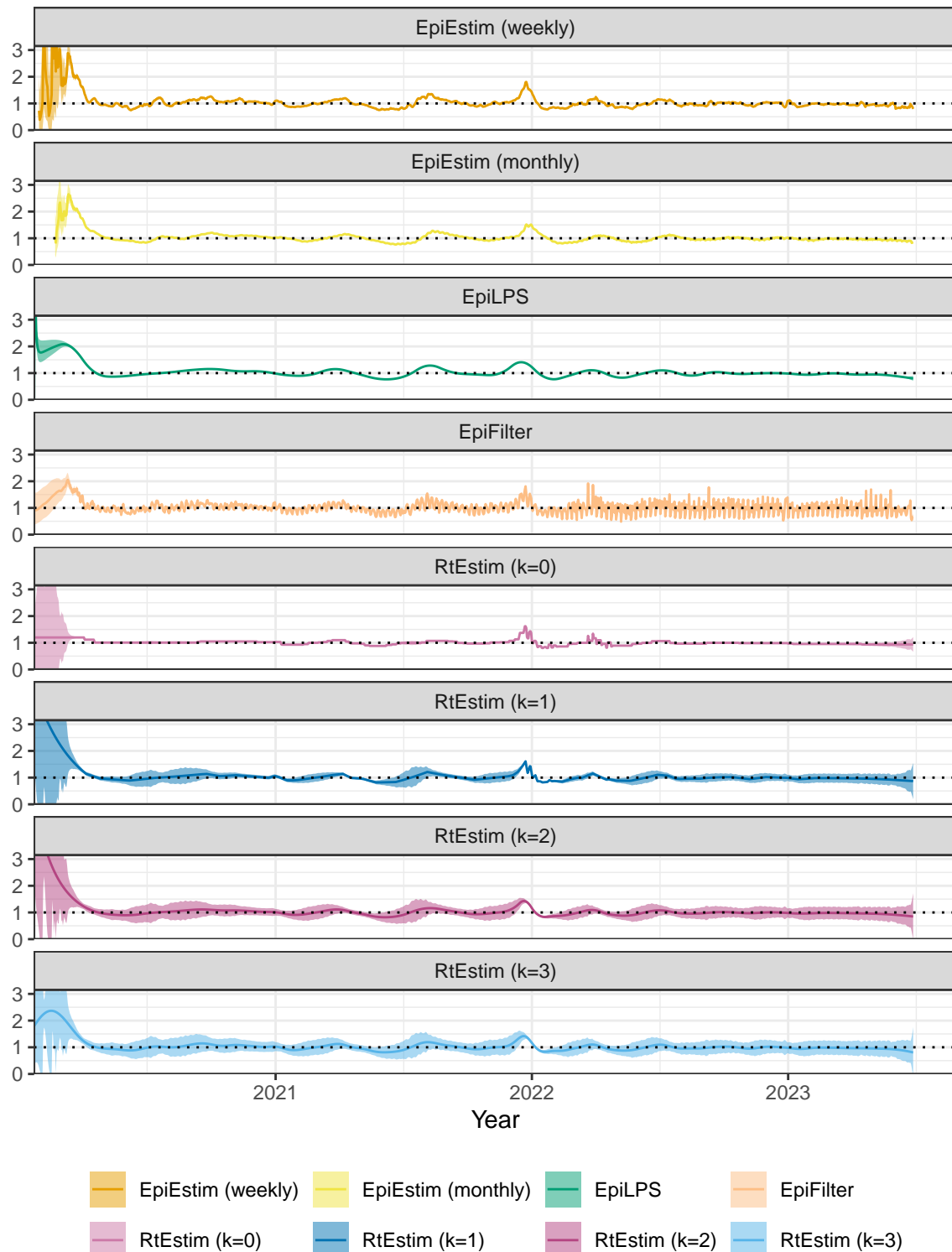


Figure A.8.1: Rt estimates with CIs for Covid19.

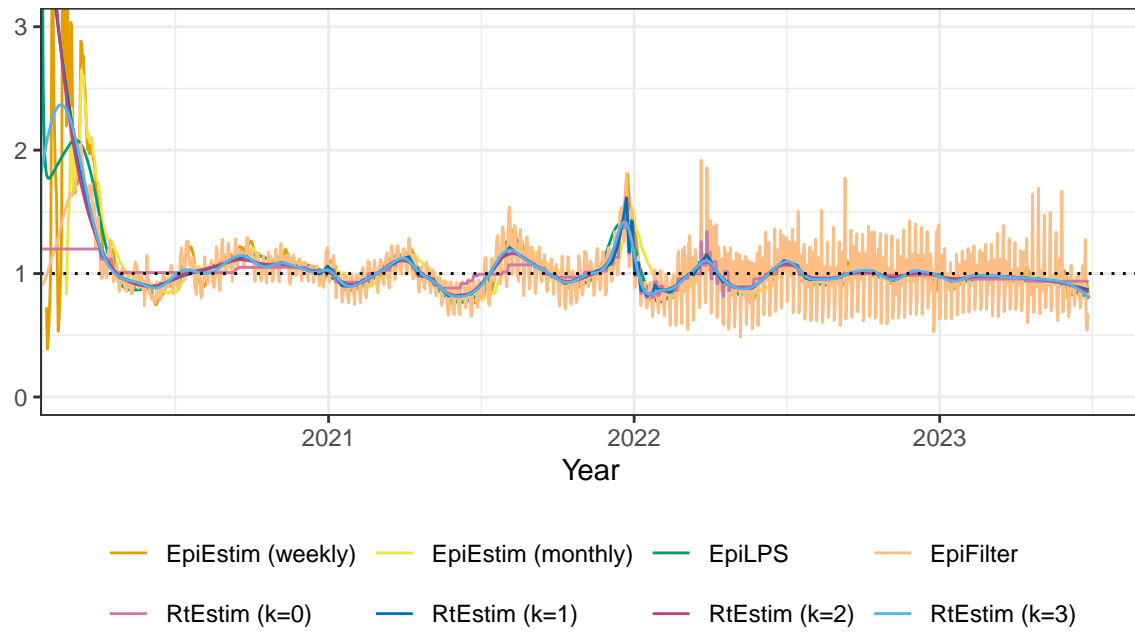
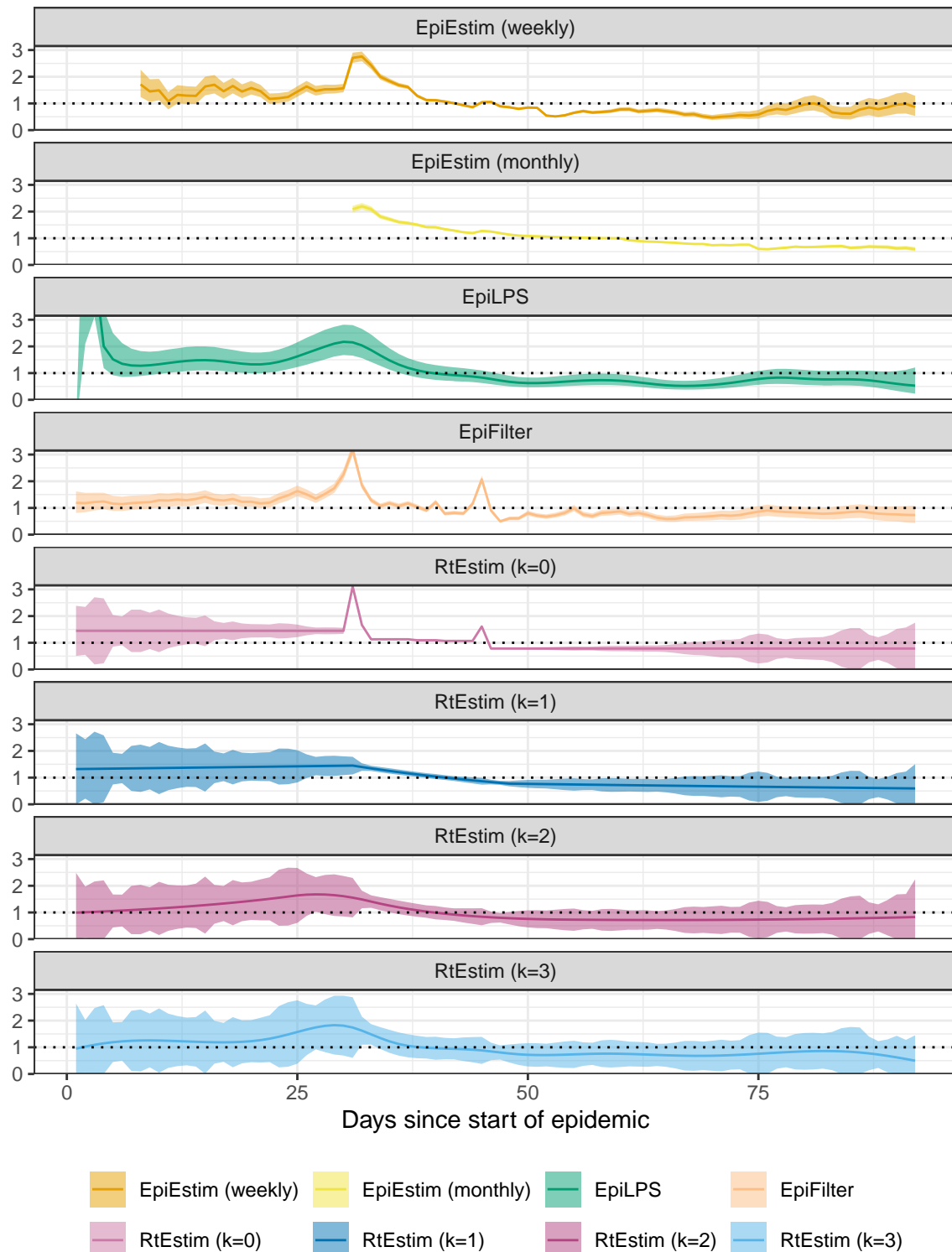


Figure A.8.2: Rt estimates for Covid19.


Figure A.8.3:  $R_t$  estimates with CIs for Flu 1918.

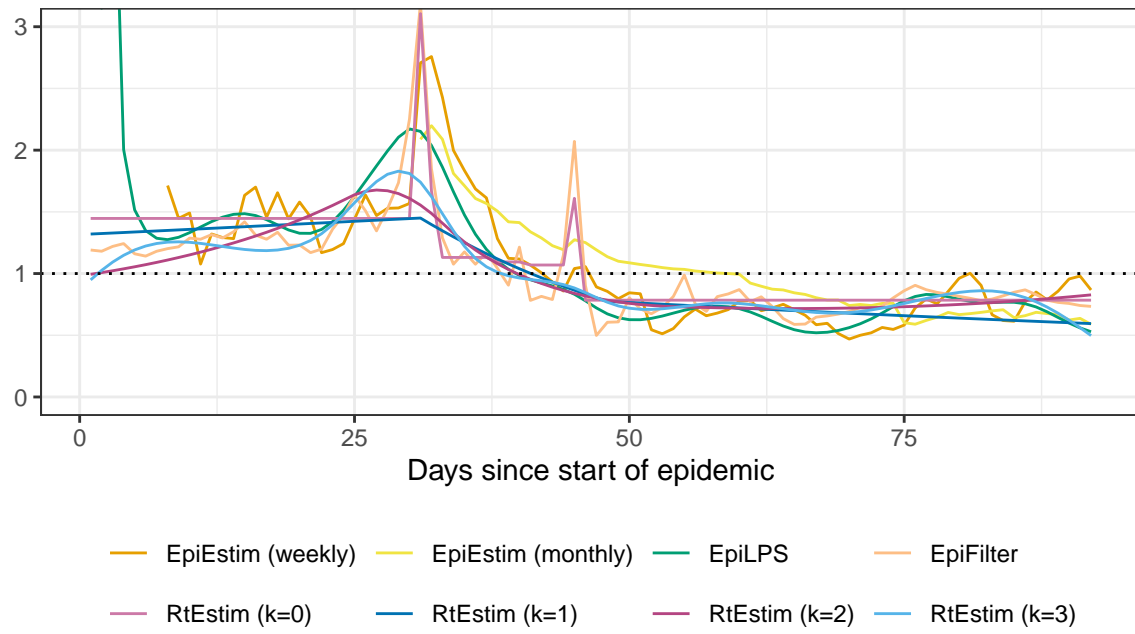


Figure A.8.4: Rt estimates for Flu 1918.